



All Theses and Dissertations

2016-09-01

Energy Quantity Estimation in Radiated Acoustic Fields

Eric B. Whiting
Brigham Young University

Follow this and additional works at: <https://scholarsarchive.byu.edu/etd>

 Part of the [Astrophysics and Astronomy Commons](#)

BYU ScholarsArchive Citation

Whiting, Eric B., "Energy Quantity Estimation in Radiated Acoustic Fields" (2016). *All Theses and Dissertations*. 6159.
<https://scholarsarchive.byu.edu/etd/6159>

This Thesis is brought to you for free and open access by BYU ScholarsArchive. It has been accepted for inclusion in All Theses and Dissertations by an authorized administrator of BYU ScholarsArchive. For more information, please contact scholarsarchive@byu.edu, ellen_amatangelo@byu.edu.

Energy Quantity Estimation in Radiated Acoustic Fields

Eric B. Whiting

A thesis submitted to the faculty of
Brigham Young University
in partial fulfillment of the requirements for the degree of
Master of Science

Kent L. Gee, Chair
Tracianne B. Neilsen
Scott D. Sommerfeldt

Department of Physics and Astronomy
Brigham Young University

Copyright © 2016 Eric B. Whiting

All Rights Reserved

ABSTRACT

Energy Quantity Estimation in Radiated Acoustic Fields

Eric B. Whiting

Department of Physics and Astronomy, BYU

Master of Science

Energy quantities, which are calculated from pressure and particle velocity, yield a great deal of information about acoustic fields. Errors in pressure or particle velocity estimation lead to bias errors in the estimation of energy quantities. The bias errors arise from different probe configurations and processing methods. Two processing methods are examined: the traditional method and the recently developed Phase and Amplitude Gradient Estimation (PAGE) method. These two methods are compared to investigate how each estimates pressure and particle velocity and the subsequent bias errors in a plane wave, standing wave, and spherical spreading wave field. Analytical expressions are derived for the energy quantity estimation using ideal one-dimensional probes. A simulation of the field from a baffled circular piston and measurements using ideal two-dimensional probes is computed. Compared to the traditional method, the PAGE method significantly extends the range of frequencies for which the results are accurate. It is found that a probe with a center microphone significantly reduces the estimation error and extends the usable range of frequencies. The PAGE method with unwrapping, perfectly matches the analytical results for plane waves, while the traditional method is only good at wavelengths that are large compared to the probe size. Furthermore, the PAGE method has a constant bias error in spherical wave fields due to the $1/r$ decrease in pressure. The traditional method has a frequency dependent bias error that is much worse at higher frequencies. Lastly, the PAGE method has the same or worse error for the standing wave. As an application of energy quantities, acoustic intensity is used to develop an equivalent source model for jet noise from an F-22 at military and afterburner engine conditions. An optimization is used to find the best-matching wavepacket model for measured intensity vectors. The results are compared to another intensity method of estimating the source region and source directivity, and the two methods have good agreement.

Keywords: acoustic intensity, energy density, specific acoustic impedance

ACKNOWLEDGMENTS

Every time I try to put into words what the faculty of BYU Acoustics have done for me, I feel like my words fail to grasp their true greatness. Pleasantries seem inadequate to describe what they have done, even sacrificed, in order to help me. Everyone has gone beyond what was expected to help their students. Countless hours were put into class lectures. Labs had great thought and required great effort. Homework was challenging beyond the simple plug and chug problems. Writing was included in every class. All of this took time and consideration on behalf of the instructors: Dr. Gee, Dr. Neilsen, Dr. Leishman, and Dr. Sommerfeldt. They all put in incredible effort to make each class the best it could be and really set BYU apart. While I did not have a class from Dr. Anderson, I recognize the same traits in him and know that he will be a great professor.

Besides the classes, the individual guidance from professors was incredible. Dr. Leishman sat down and talked with me on numerous occasions to guide me on a career path. He was the first one to encourage me to study acoustics. Dr. Sommerfeldt also spent countless hours advising me on research and helping to understand results. Truly, his greatness is demonstrated by the fact that he has so many things calling for his attention, and yet he still made time for long meetings about my research. He was supportive and helpful throughout the whole process. Dr. Gee and Dr. Neilsen spent incalculable hours at meetings advising me about research. They displayed immense amount of patience and kindness as I struggled to perform at the level required for graduate work. They even showed respect and gave a lot of encouragement as I was often discouraged in writing and research. Truly, their efforts on my behalf were exemplary. They spent many late nights and long hours editing my work. In this they demonstrated immense integrity and character that I only aspire to. They were consistently supportive and ready to help.

I would like to thank my family for their support. I suppose no one knows more than my wife the discouragement and stress I experienced as I worked and studied over the past two years. She was always encouraging me and helping me make progress. I will never forget the hours, even days, she spent editing all my work, looking over papers, and forcing me to practice presentations. She truly helped me reach this point. Lastly, Maddy has brought a lot of joy as I have struggled to finish this thesis.

My acknowledgments would be incomplete without mentioning the many peers that have helped this work progress. This includes my office mates Blaine Harker, Trevor Stout, Brent Reichman, and Kyle Miller as well as surrogate office mates Matt Calton, Josh Bodon, Zac Jensen, Kelly Succo, Sarah Young, Pegah Aslani, and Miles Davis. Each has offered suggestions for my research and been an example and support for the past two years. It should also be noted there are many who have gone before me, who have influenced this work. In particular, Ben Christensen gave the initial explanation of the PAGE method and helped me get started with my work. Along with this, Darren Torrie has worked with me the entire time and has done a lot of analysis and data gathering supporting this work. The experimental verification of the methods discussed in this thesis was completely Darren's work. Along with Darren, there have been many undergraduates who have helped with this work. They have all been helpful and encouraging.

Lastly, none of this work and research would have been possible without the generous funding from many sources. I would like to thank the Office of Naval Research, the National Science Foundation, Air Force Research Labs, and NASA for funding me in this research. Likewise, the initial study of rocket noise could not have occurred without a close association with Blue Ridge Research and Consulting.

Table of Contents

ABSTRACT.....	ii
ACKNOWLEDGMENTS	iii
Table of Contents.....	v
List of Figures.....	vii
List of Tables:.....	xiii
Chapter 1.....	- 1 -
1.1 Energy-based acoustics	- 1 -
1.2 Obtaining energy quantities	- 2 -
1.3 The PAGE method	- 3 -
1.4 Thesis Outline	- 7 -
Chapter 2.....	- 9 -
2.1 Introduction.....	- 9 -
2.2 Estimating pressure at the center of the microphone array	- 10 -
2.3 Estimating the pressure gradient	- 17 -
2.4 Estimating particle velocity.....	- 18 -
2.5 Obtaining Energy-based Quantities from Experimental Data.....	- 21 -
2.5.1 Acoustic Intensity.....	- 21 -
2.5.2 Energy density.....	- 24 -
2.5.3 Specific acoustic impedance	- 26 -
2.6 Conclusion.....	- 28 -
Chapter 3.....	- 29 -
3.1 Introduction.....	- 29 -
3.2 Plane wave.....	- 31 -
3.2.1 Analytical expressions.....	- 31 -
3.2.2 Traditional and PAGE method error expressions	- 32 -
3.2.2.1 Pressure relative error.....	- 32 -
3.2.2.2 Particle velocity relative error	- 35 -
3.2.2.3 Intensity relative error	- 36 -
3.2.2.4 Energy density relative error	- 38 -
3.2.2.5 Specific acoustic impedance relative error.....	- 41 -
3.3 Standing wave	- 42 -
3.3.1 Analytical Expressions	- 42 -
3.3.2 Error expressions.....	- 43 -
3.4 Monopole	- 49 -

3.4.1	Analytical Expressions	- 49 -
3.4.2	Error expressions	- 50 -
3.4.2.1	Pressure relative error	- 50 -
3.4.2.2	Particle velocity relative error	- 52 -
3.4.2.3	Intensity relative error	- 54 -
3.4.2.4	Potential and kinetic energy density relative error	- 58 -
3.4.2.5	Specific acoustic impedance relative error	- 62 -
3.5	Conclusions	- 65 -
Chapter 4	- 69 -
4.1	Introduction	- 69 -
4.2	Simulating two dimensional fields	- 69 -
4.3	Simulating results of different probe configurations	- 70 -
4.4	Baffled circular piston results	- 72 -
4.5	Conclusions	- 82 -
Chapter 5	- 84 -
5.1	Introduction	- 84 -
5.2	Methods	- 87 -
5.2.1	Model	- 87 -
5.2.2	Simulated annealing algorithm	- 91 -
5.2.3	Verification of Optimization	- 94 -
5.3	Results	- 95 -
5.3.1	Example of optimization results	- 96 -
5.3.2	Military engine condition	- 100 -
5.3.3	Afterburner engine condition	- 103 -
5.4	Conclusion	- 105 -
Chapter 6	- 107 -
6.1	Conclusions	- 107 -
6.2	Future Work	- 108 -
Appendix A	- 110 -
A.1	Derivations of two- and three-microphone expressions	- 110 -
A.2	Traditional method two-microphone expression:	- 110 -
A.3	Traditional method three-microphone expression:	- 112 -
A.4	PAGE method two-microphone expression:	- 113 -
A.5	PAGE method three-microphone expression:	- 114 -
Bibliography	- 117 -

List of Figures

- Figure 1.1. The sound intensity level (LI) in a GEM-60 rocket noise field computed using the traditional or finite-difference method (FD) and the PAGE method. Both are compared to the sound pressure level (Lp). - 5 -
- Figure 1.2. The localization of the noise source region for the GEM-60 rocket motor at 1200 Hz. Each triangle or circle represents an energy probe location. Using the acoustic intensity vectors that were within 3 dB of the peak level, the vectors were traced back to the centerline of the plume to determine a source region for the noise. At 1200 Hz, the source region is roughly 10 to 20 nozzle diameters (D) downstream from the nozzle of the engine. - 6 -
- Figure 1.3. The source location for various frequencies using the method described in Figure 1.2 to determine the source location along the centerline. At low frequencies the source region is farther upstream than at higher frequencies, where the source region is between 10 to 20 nozzle diameters (D) downstream. - 6 -
- Figure 2.1. A two-microphone energy probe with spacing d from the probe center to a microphone. - 10 -
- Figure 2.2. The phase for a plane wave as a function of kr for $r = 1\text{m}$ and zero initial phase. The wrapped phase has discontinuities at odd multiples of π . The unwrapped phase correctly subtracts 2π to the wrapped phase in order to produce a continuous line. - 14 -
- Figure 2.3. Phasor diagram for estimating the center pressure of a plane wave with a two-microphone intensity probe using both the traditional (left) and the PAGE (right) processing methods. The dashed grey line shows the path the correct center pressure follows, while the black line shows the path the actual estimate traces out for the specific method. The black x shows the correct center pressure for the particular wavenumber (k) and microphone spacing (a). The red and blue vectors show the relative phasors for the first and second microphone, respectively. The green line is the estimate of the center pressure at the particular kd value. - 16 -
- Figure 2.4. Phasor diagram for estimating the particle velocity of a plane wave with a two-microphone intensity probe using both the traditional (left) and the PAGE (right) processing methods. The dashed gray line represents the path of the actual particle velocity. The black line shows the path of the estimation, and the black x marks the correct value. The traditional method's magnitude falls off as frequency increases. Also, beyond the SNF, the phase of the particle velocity using the traditional method is π radians out of phase. The PAGE method with unwrapping has no bias error for the plane wave case. - 20 -
- Figure 3.1. Schematic of the two-microphone one-dimensional probe (top) and the three-microphone probe (bottom) one-dimensional probe. r is the distance from the origin to the center of the probe, and d is the distance from the center of the probe to the outside microphones. - 30 -
- Figure 3.2. The computed magnitude and phase of the relative error ($ep + 1$) of the complex pressure at the center of a two-microphone intensity probe from different methods.

The SNF indicates where the complex pressure measured from the microphones is π radians out of phase. The traditional method estimate of the center pressure magnitude goes to zero at the SNF. Both the unwrapped and wrapped PAGE method have the correct magnitude, but only the unwrapped PAGE method has the correct phase above the SNF..... - 34 -

Figure 3.3. The computed magnitude and phase relative error ($eu + 1$) of the complex particle velocity at the center of a two-microphone intensity probe from different methods. The SNF indicates where the complex particle velocity estimated from the microphones is π radians out of phase. Both the unwrapped and wrapped PAGE methods have the correct magnitude, but only the unwrapped PAGE method has the correct phase above the SNF..... - 36 -

Figure 3.4. Estimates of the active intensity relative error for a plane wave using a two- and three-microphone probe using both the traditional and PAGE methods. The PAGE method's estimations (with phase unwrapping) are exactly equivalent to the analytical expressions, so no error is produced. The traditional method's errors in pressure and particle velocity estimation lead to errors in active intensity estimation. The three-microphone probe does not have errors in pressure estimation, extending the usable bandwidth to twice that of the two-microphone probe. - 38 -

Figure 3.5. The relative error for estimates of the potential (top) and kinetic energy density (bottom) for a plane wave..... - 40 -

Figure 3.6. The relative error in the total energy density for a plane wave using the different probes and processing methods. - 40 -

Figure 3.7. The relative error in the specific acoustic impedance for a plane wave using the different probes and processing methods. The top plot shows the magnitude error, and the bottom plot shows the discrepancy in phase. - 42 -

Figure 3.8. The relative pressure error for a standing wave using two-microphones to estimate the center pressure. When the microphones span a node, the PAGE method averages the phase of the center microphone to be $\pi/2$ radians. Furthermore, as the actual center of the probe approaches a node, the PAGE method overestimates the magnitude and the relative error blows up. When the PAGE method does not have jumps, it follows the traditional method. The traditional method rolls off exactly like the plane wave case..... - 47 -

Figure 3.9. The relative particle velocity error for a standing wave using two-microphones to estimate the center pressure. The nodes of the standing wave cause jumps in the phase and magnitude for the PAGE method. Despite the jumps, the PAGE method follows the trend of the traditional method. The traditional method rolls off like in the plane wave. - 48 -

Figure 3.10. The computed magnitude and phase error of complex pressure for a monopole at a distance of $r = 4.3d$, where $d = 2\text{ cm}$ and is the spacing from one microphone to the center. Both the traditional method and PAGE methods for calculating complex pressure at the center of a two-microphone intensity probe are shown. The SNF indicates where the complex pressures measured from the microphones are π radians out of phase. All methods are affected by the bias error caused by the proximity to the

source and the spacing of the probe. Only the unwrapped PAGE method has the correct phase above the SNF.....	52 -
Figure 3.11. The computed magnitude and phase error of particle velocity for a monopole at a distance of $r = 4.3d$. $d = 2\text{ cm}$ and is the spacing from one microphone to the center. The error for both the traditional method and PAGE methods for calculating particle velocity at the center of a two-microphone intensity probe are shown. The SNF indicates where the microphones are half a wavelength apart, making the phase between their measurements π radians different. All methods are affected by the bias error caused by the proximity to the source and the spacing of the probe. Only the unwrapped PAGE method has the correct phase above the SNF.	53 -
Figure 3.12. Active intensity relative error for different methods and probes for a monopole at a distance of $r = 4.3d$. $d = 2\text{ cm}$ and is the spacing between the microphone and the center. The top plot shows the magnitude error and the bottom plot shows direction errors.	55 -
Figure 3.13. Active intensity relative error for the traditional and PAGE methods applied to two and three-microphone probes. The black line is the spatial Nyquist limit. The three-microphone PAGE case has no error in estimating active intensity for all values of kd and kr . The two-microphone probe is susceptible to bias error when the probe is only a few d from the source. The traditional method also breaks down for large values of kd	56 -
Figure 3.14. The reactive intensity relative error for $r = 2d$, $d = 2\text{ cm}$, and d is the distance between the center and an outer microphone. Bias error is present in all of the processing and probes depicted. The traditional method applied to three-microphone probe is frequency dependent in its error, as are both of the PAGE method estimates. -	57 -
Figure 3.15. Relative error for reactive intensity as a function of kd and kr . The black line indicates the spatial Nyquist limit. Bias errors are present in all processing and probes. The PAGE three-microphone results have slightly less relative error than the two-microphone results. The traditional and PAGE methods are the same for the two-microphone case.....	58 -
Figure 3.16. The energy density relative error when $r = 4.3d$. The top plot is the potential energy, and the bottom plot is the kinetic energy. The traditional method has error that oscillates above the Nyquist limit. The PAGE method shows constant bias errors. The bias error goes to 0 dB above the Nyquist limit for the three-microphone case.....	59 -
Figure 3.17. The relative total energy density error with the probe at $r = 4.3d$	60 -
Figure 3.18. Relative error for potential energy density as a function of kd and kr . The black line indicates the spatial Nyquist limit.	61 -
Figure 3.19. Relative error for kinetic energy density as a function of kd and kr . The black line indicates the spatial Nyquist limit. The PAGE method estimate with the three-microphone probe has less error at higher frequencies, but the two-microphone probe has a constant bias error. The traditional method's analysis is again frequency dependent and worsens near the Nyquist limit.	62 -

- Figure 3.20. The relative error for specific acoustic impedance of a monopole where the probe is at $r = 4.3d$ - 64 -
- Figure 3.21. Relative error for the magnitude of specific acoustic impedance. The traditional method has large errors at high frequencies because that's where its estimates of pressure and particle velocity break down. The PAGE method's estimate with the two-microphone probe results in zero error. The three-microphone probe has a constant bias error due to microphone spacing and distance to source, but this bias decreases at the higher frequencies. - 65 -
- Figure 4.1. The three probe configurations: (a) equilateral triangle with a microphone at the center, (b) the orthogonal pair of microphones with no microphone at the center, and (c) the orthogonal pair of microphones with a microphone at the center. - 71 -
- Figure 4.2. Magnitude error for active intensity between the analytical solution of the baffled circular piston and various estimates at 8 kHz from different probes using the PAGE method. Subplot (a) shows the active sound intensity level and some active intensity vectors. The remaining subplots show the error, on a decibel scale, in magnitude of the active intensity estimates obtained for (b) the equilateral triangle probe with a microphone at the center, (c) the orthogonal probe with no microphone at the center, and (d) the orthogonal probe with a microphone at the center. The size of the probe and microphone positions are shown in the bottom left corner of each error subplot... - 74 -
- Figure 4.3. Magnitude error for reactive intensity between the analytical solution and various estimates at 8 kHz from different probes using the PAGE method. Subplot (a) shows the reactive sound intensity level and some reactive intensity vectors from the baffled circular piston model. The remaining subplots show the error, on a decibel scale, in magnitude of the reactive intensity estimates obtained for (b) the equilateral triangle probe with a microphone at the center, (c) the orthogonal probe with no microphone at the center, and (d) the orthogonal probe with a microphone at the center. The size of the probe and microphone positions are shown in the bottom left corner of each error subplot. - 76 -
- Figure 4.4. Magnitude error for potential energy density between the analytical solution and various estimates at 8 kHz from different probes using the PAGE method. Subplot (a) shows the potential energy density level from a baffled circular piston. The remaining subplots show the error, on a decibel scale, in magnitude of the potential energy estimates obtained for (b) the equilateral triangle probe with a microphone at the center, (c) the orthogonal probe with no microphone at the center, and (d) the orthogonal probe with a microphone at the center. The size of the probe and microphone positions are shown in the bottom left corner of each error subplot... - 78 -
- Figure 4.5. Magnitude error for kinetic energy density between the analytical solution and various estimates at 8 kHz from different probes using the PAGE method. Subplot (a) shows the kinetic energy density level for the baffled circular piston. The remaining subplots show the error, on a decibel scale, in magnitude of the kinetic energy estimates obtained for (b) the equilateral triangle probe with a microphone at the center, (c) the orthogonal probe with no microphone at the center, and (d) the

orthogonal probe with a microphone at the center. The size of the probe and microphone positions are shown in the bottom left corner of each error subplot... - 79 -

Figure 4.6. Error plot showing the magnitude error for specific acoustic impedance between the analytical solution and various estimates in the direction of the active intensity at 8 kHz from different probes using the PAGE method. Subplot (a) shows the specific acoustic impedance for a baffled circular piston divided by the specific acoustic impedance of a plane wave. for the baffled circular piston. The remaining subplots show the error, on a decibel scale, in magnitude of the specific acoustic impedance estimates obtained for (b) the equilateral triangle probe with a microphone at the center, (c) the orthogonal probe with no microphone at the center, and (d) the orthogonal probe with a microphone at the center. The size of the probe and microphone positions are shown in the bottom left corner of each error subplot... - 81 -

Figure 5.1. Experimental Setup. (a) Photograph of the intensity probe on top of the 90 microphone array. (b) Schematic of noise measurements of a tethered high-performance military aircraft. The red triangles indicate the positions of the 90 microphone array. - 85 -

Figure 5.2. Various normalized wavepacket shapes. The baseline parameters are $Uc = 478 m/s$, $b1 = 4 m$, $b2 = 14 m$, $g1 = 14 m$, and $g2 = 2 m$. For the various plots (b)-(f), one parameter is changed from the baseline as indicated in the plot. - 90 -

Figure 5.3. The various cost functions for military engine condition at 125 Hz for 10 different optimization runs. - 94 -

Figure 5.4. The optimized wavepacket (a) for military engine condition at 125 Hz. The center line shows the measured (blue dashed) and modelled (red) intensity magnitude for the three intensity probe measurement plane 1 (b), plane 2 (c), and the 22.9 m arc (d), shown in Figure 5.1(b). The bottom line shows the agreement of measured and modelled intensity directions for the same locations. - 97 -

Figure 5.5. For 125 Hz and military engine condition, subplot (a) shows the measured afterburner acoustic intensity vectors, and subplot (b) shows the wavepacket-predicted intensity vectors. Subplot (b) has the wavepacket-predicted intensity level throughout the region. The dashed line indicates the approximate jet shear layer. The predicted levels inside the shear layer are not related to the turbulent flow and have no meaning. - 97 -

Figure 5.6. Same as Figure 5.4, but at 1000 Hz. - 98 -

Figure 5.7. Same as Figure 5.5, but at 1000 Hz. - 99 -

Figure 5.8. Comparison of the estimated maximum equivalent source regions from the ray-tracing method employed by Stout et al. and the optimized wavepacket ESM for the F-22 when a single engine was operated at military engine conditions - 101 -

Figure 5.9. Comparison of the direction of the largest measured and wavepacket-predicted intensity vectors on plane 2 at military engine conditions. The dotted green line represents the peak radiation direction computed from the optimized convective velocity using Eq. 5.2. - 103 -

- Figure 5.10. Comparison of the estimated maximum equivalent source region from the ray-tracing method employed by Stout et al. and the optimized wavepacket ESM for the F-22 when a single engine was operated at afterburner power..... - 104 -
- Figure 5.11. Comparison of the direction of the largest measured and wavepacket-predicted intensity vectors on plane 2 at afterburner engine conditions. The dotted green line represents the peak radiation direction computed from the optimized convective velocity using Eq. 5.2..... - 105 -

List of Tables:

Table 2.1. Expression for single-sided active intensity for the two and three-microphone one dimensional probe using both the traditional and PAGE methods. - 24 -

Table 2.2. Expression for single-sided reactive intensity for the two- and three- microphone one-dimensional probe using bot the traditional and PAGE methods. - 24 -

Table 2.3. Expressions for single-sided potential energy density for the two and three-microphone one-dimensional probe using both the traditional and PAGE methods - 25 -

Table 2.4. Expressions for single-sided kinetic energy density for the two and three-microphone one dimensional probe using both the traditional and PAGE methods. - 26 -

Table 2.5. The single-sided specific acoustic impedance found using the traditional and PAGE methods. - 27 -

Table 3.1. Analytic expressions for acoustic quantities in the acoustic field of a propagating plane wave. - 32 -

Table 3.2. Relative error for center pressure estimates using the traditional and PAGE method with a two and three-microphone one-dimensional probe for a plane wave. For the two-microphone case, the PAGE estimate with correct phase unwrapping has zero error even above the SNF. Without phase unwrapping, the estimate above the SNF is not used. Therefore, the high frequency limit for the PAGE method without unwrapping is 1.57kd. With a center microphone, either processing method can go as high in frequency because the pressure is accurately determined. - 34 -

Table 3.3. The relative error expressions for particle velocity in a plane wave field. - 35 -

Table 3.4. Relative error for active and reactive intensity using the traditional and PAGE method with a two- and three-microphone probe. Because the reactive intensity is analytically zero, the relative error for this quantity is not applicable (NA). - 37 -

Table 3.5. Relative error expressions for potential and kinetic energy density using the traditional and PAGE method with a two and three-microphone probe. - 39 -

Table 3.6. Relative error for specific acoustic impedance using the traditional and PAGE method with a two- and three-microphone probe. - 41 -

Table 3.7. Analytic expressions for pressure, particle velocity, active intensity, reactive intensity, potential energy density, kinetic energy density, and specific acoustic impedance in an infinite standing wave field. The active intensity is zero because a standing wave does not propagate. - 43 -

Table 3.8. The relative error for estimates of energy quantities for an infinite standing wave. The traditional and PAGE method give identical results as long as the probe does not span a null (microphones not closely spaced), otherwise the PAGE give worse results than the traditional method. Because the active intensity is zero, the relative error for this quantity is not applicable (NA). - 45 -

Table 3.9. Analytic expressions for the energy quantities in the field of a monopole. - 50 -

Table 3.10. Relative error for pressure using the traditional and PAGE method with a two and three-microphone probe for the monopole case. Also, the expected location (kd) where the error exceeds ± 0.5 dB is listed. For relative error functions where the error theoretically never exceeds 0.5 dB, nothing is listed. If there is a center microphone, then the results should be accurate for the frequency range over which the microphone frequency response is relatively flat. If there is no center microphone and phase unwrapping is not applied, the PAGE method estimates for the center pressure are good until $kd = \pi/2$, the spatial Nyquist limit. - 51 -

Table 3.11. The relative error expression for particle velocity for a monopole source. - 53 -

Table 3.12. Relative error active and reactive intensity using the traditional and PAGE method with a two and three-microphone probe for the monopole case. - 54 -

Table 3.13. Relative error for potential and kinetic energy using the traditional and PAGE method with a two and three-microphone probe for the monopole case. - 59 -

Table 3.14. Relative error for the specific acoustic impedance using the traditional and PAGE method with a two- and three-microphone probe for the monopole case. - 63 -

Table 5.1. Actual and optimized wavepacket parameters for a numerical case comparable to the wavepacket obtained for the F-22 measured intensity at 125 Hz and military engine condition. The top row lists the chosen parameters for the simulated wavepacket. The second and third row indicate the mean and standard deviation, respectively, after the 100 optimizations. - 95 -

Chapter 1

Introduction

1.1 Energy-based acoustics

The use of energy-based acoustical measurements has increased during the past few decades. Energy-based measurements include acoustic intensity, acoustic energy density, and specific acoustic impedance and can be used to characterize a source or sound field. Acoustic intensity describes the time rate of energy flow through a surface. Intensity is a vector, which allows it to describe not only the amount of energy flow, but also the direction. Acoustic energy density is the sum of the potential and kinetic energy densities. The potential energy density describes how much energy is stored in the air from the compression of the air due to an acoustic wave, much like a compressed spring has potential energy. Kinetic energy density describes the energy in the air from the movement of the air molecules. Lastly, specific acoustic impedance relates the acoustic pressure to the particle velocity in the frequency domain. This ratio describes the influence the medium has on the wave field.

Energy-based measurements have benefits over traditional scalar pressure measurements. Acoustic intensity has been used in a variety of ways. One common use of active intensity measurements has been to integrate over multiple measurement locations to find the radiated sound power of a source.¹⁻⁶ A particularly useful application is to measure the sound power of a machine in situ.^{7,8} Using intensity measurements over a surface for determining sound power is advantageous because it is less affected by noise outside the surface. Several standards on

measuring acoustic intensity to obtain acoustic power have been published.⁹⁻¹³ Another application is to use intensity vectors to find the source location.^{14, 15} A third application of acoustic intensity is acoustic holography, which uses pressure and particle velocity measurements to visualize the acoustic fields.¹⁶⁻²¹ Lastly, Mann and Tichy²² used reactive intensity and the complex specific impedance to differentiate between a three point source and a two point source with resonator. While acoustic intensity has been mainly used for propagating waves, energy density has been used extensively in enclosed fields. Acoustic energy density has been successfully used for active control of noise in enclosures as a better quantity to minimize than the traditionally-used squared pressure measurements.²³⁻²⁹ Energy density is also useful in describing the global sound properties in a room.^{24, 30, 31} Specific acoustic impedance has been used mainly in studying propagation in ducts. Lastly, all of these energy quantities can be leveraged to describe the transition between the acoustic near and far fields for propagation from arbitrary sources.

1.2 Obtaining energy quantities

Since all the energy quantities considered here are based on the product or ratio of acoustic pressure and particle velocity, it is important to measure these two quantities accurately. Pressure is easily measured using a microphone, but there are multiple ways to obtain particle velocity. Until recently, measuring particle velocity was challenging and very inaccurate. The Microflown^{32, 33} directly measures particle velocity, but because it is based on heated wires, it is susceptible to errors caused by moving or turbulent air. An alternative method to obtain particle velocity is to use Euler's equation, which relates the gradient of pressure to particle velocity. With this equation, pressure measured at several closely spaced microphones can be used with a finite difference to estimate the gradient of pressure and obtain particle velocity. When used to

find acoustic intensity, this is called the p-p method. Although originally used in the time domain, this method is now implemented in the frequency domain. The frequency-domain approach uses the imaginary part of the cross spectrum between a pair of microphones to obtain the time-averaged active intensity component.³⁴⁻³⁷ Although an effective method, the traditional p-p or cross-spectral method is limited to a relatively small range of frequencies. At the lower end of the range, the phase mismatches between the measurement channels cause errors that grow larger as the distance between the microphones becomes smaller. The upper end of the frequency range is limited by the separation between microphones compared to the wavelength of sound. A smaller separation here means a higher usable frequency range. These and other errors have been analyzed by Fahy,² Jacobsen,³⁸⁻⁴⁰ Elko,⁴¹ and others.⁴²⁻⁴⁴ Furthermore, many have tried to correct for errors or find an optimal arrangement of microphones or processing method to minimize error.⁴⁵⁻⁵¹ To extend the usable frequency range, a new processing method has been developed that allows the use of a larger separation between microphones for more accurate lower frequency measurements, but still achieves accurate results at higher frequencies.

1.3 The PAGE method

The Phase and Amplitude Gradient Estimation (PAGE) method was developed to extend the usable bandwidth over which energy quantities could be obtained.^{52, 53} This method, developed recently at BYU, utilizes measurements of complex pressure differently than the traditional method. The PAGE method is based on the work of Mann et al.⁵⁴ and Mann and Tichy,^{22, 55} who expressed complex pressure in terms of a magnitude and phase and showed that the particle velocity can be written in terms of a gradient of phase and a gradient of magnitude. The traditional method and the PAGE method both use finite differences to estimate the gradient. The advantage of the PAGE method is the gradient of phase and magnitude can be better

estimated using a first-order difference, rather than the traditional gradient estimation of a complex number. This leads to the PAGE method being accurate up to the frequency where the spacing between microphones is equal to a half wavelength. The PAGE method can actually be accurate beyond this point, but the phase has to be unwrapped, which is explained later.

The PAGE method was developed with the intent to analyze the broadband noise from a rocket or jet engine. Gee et al.⁵⁶ used the PAGE method to analyze intensity from a Mach 1.8 laboratory-scale jet using the PAGE method. He found that the frequency range where he could analyze data was almost an order of magnitude larger than that of the traditional method. Similarly, Stout et al.¹⁴ used intensity measurements from an F-22A Raptor at military and afterburner engine conditions to find a source region and a directivity from the source. Lastly, Gee et al.⁵⁷ used the PAGE method to extend the region where acoustic measurements of a GEM-60 rocket could be analyzed. Figure 1.1 shows that the PAGE method sound intensity level agrees with the sound pressure level (which is expected for a propagating sound field) for the frequency range from 40 Hz to 4 kHz, while the traditional method matches at low frequencies, but rolls off at higher frequencies. At about 3 kHz, the traditional method has rolled off by 5 dB. Since the PAGE method predicts a sound intensity level that matches the sound pressure level to at least 4 kHz, the acoustic vector intensity measurement is considered accurate and can be used for further analysis.

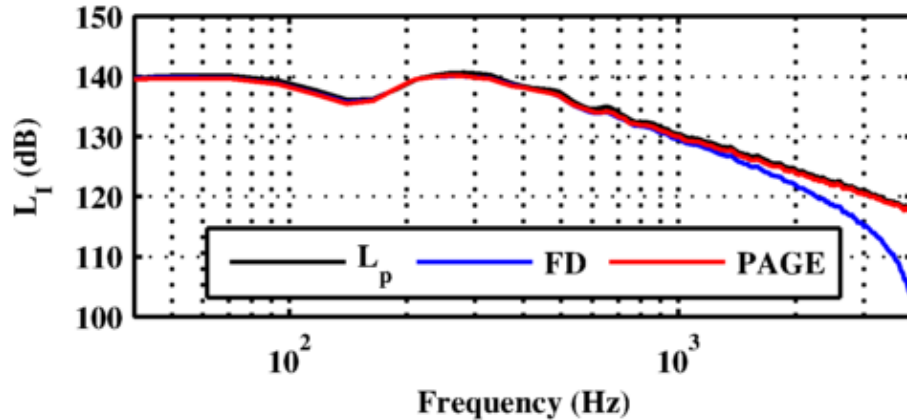


Figure 1.1. The sound intensity level (L_I) in a GEM-60 rocket noise field computed using the traditional or finite-difference method (FD) and the PAGE method. Both are compared to the sound pressure level (L_p).

After determining the frequency range where the PAGE method was accurate, an analysis of the source region and directivity of the source was performed. Using Figure 1.2 as an example of the process, the acoustic intensity vectors that were within 3 dB of the peak sound intensity level were used to trace lines in the opposite direction of the acoustic intensity vector. The points where the lines cross the centerline (x-axis) of the rocket give the extent of the dominant source region. The source location for each frequency was determined in this manner to create Figure 1.3, which shows that the source location of the noise moves closer to the nozzle at higher frequencies. This analysis, which is important to understanding rocket noise characteristics, shows the utility of the PAGE method and motivates deeper analyses of the errors associated with this method.

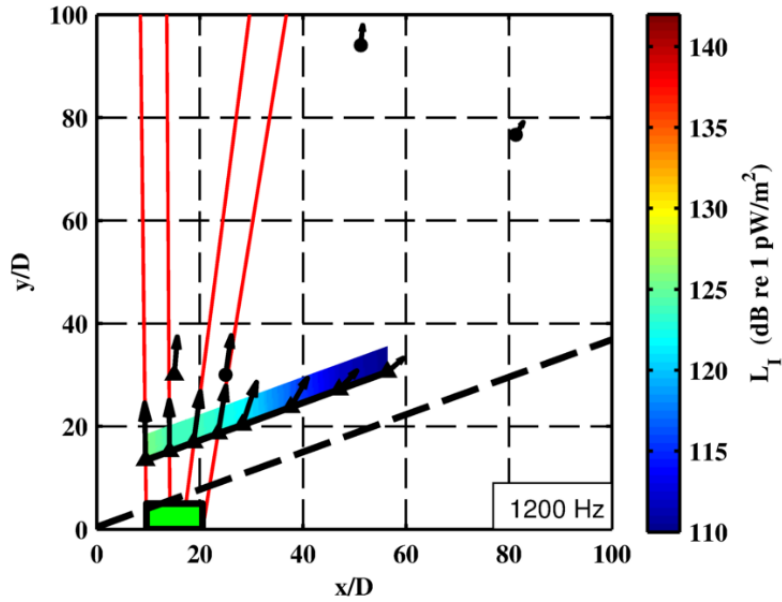


Figure 1.2. The localization of the noise source region for the GEM-60 rocket motor at 1200 Hz. Each triangle or circle represents an energy probe location. Using the acoustic intensity vectors that were within 3 dB of the peak level, the vectors were traced back to the centerline of the plume to determine a source region for the noise. At 1200 Hz, the source region is roughly 10 to 20 nozzle diameters (D) downstream from the nozzle of the engine.

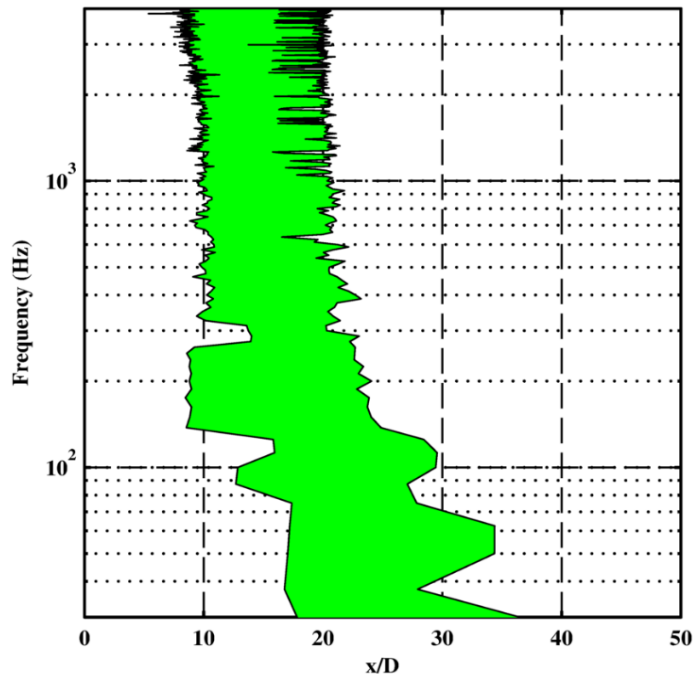


Figure 1.3. The source location for various frequencies using the method described in Figure 1.2 to determine the source location along the centerline. At low frequencies the source region is farther upstream than at higher frequencies, where the source region is between 10 to 20 nozzle diameters (D) downstream.

1.4 Thesis Outline

This thesis investigates the traditional and PAGE methods for analyzing sound fields in terms of energy quantities. Previous investigations of the PAGE method focused mainly on active intensity, but this work analyzes all the previously mentioned energy quantities. Chapter 2 discusses in detail each of the methods' estimations of the various acoustic quantities. This thesis also looks at different probe configurations and the errors introduced in either method's estimation of a sound field. This is done by simulating and analyzing simple sound fields analytically to find bias errors in the estimations. Chapter 3 focuses on the errors introduced by estimating these quantities using the traditional and PAGE methods with one-dimensional probe configurations. Chapter 4 expands the analysis of the measurement errors to those of two-dimensional probe configurations. It is found that there is a tradeoff between the number of microphones in a probe configuration and decreasing error in the estimation results.

This thesis concludes in Chapter 5 with a discussion of using a limited number of vector intensity measurements to optimize parameters for a wavepacket as an equivalent source model for the noise of a static F-22 Raptor aircraft. Measurements of the jet noise were taken using an intensity probe, and the model was developed based on the vector intensity measurements. The equivalent source wavepacket was found via a simulated annealing algorithm that optimized the fit of the predicted and measured acoustic intensity vectors. Since the motivation for the PAGE method development was to study aeroacoustic sources, it is only fitting to use energy quantities to build an optimized equivalent source model. The results are similar to those derived from pressure-based wavepacket models, but the vector intensity measurements used to develop this model require far fewer measurement points, which makes this a more efficient method of model

development. Thus, the PAGE method ability to extend the usable bandwidth of intensity calculations can further improve equivalent source model development.

Chapter 2

Pressure-based methods for estimating acoustic quantities

2.1 Introduction

Although there are many ways to calculate acoustic energy quantities, this work focuses on using microphones to measure pressure and estimate particle velocity (the p-p method). The pressure at the center of an array of microphones can be measured directly, or it can be estimated from the surrounding microphones. The traditional method and the PAGE method estimate this center pressure differently. These differences are explained in Section 2.2. In Section 2.3, a Taylor series-based method for estimating the gradient of a function is explained. After the explanation of how the gradient is estimated, Section 2.4 explains how the traditional and PAGE methods use this gradient and Euler's equation to estimate particle velocity. Both use a finite-difference scheme, but the PAGE method uses a phase and amplitude representation while the traditional method finds the difference between complex pressures using the real and imaginary parts. This seemingly subtle difference changes the useable bandwidth of each method's computation. The difference between the estimations and analytical solutions for various energy-based quantities and simple fields will be explored in Chapter 3. Finally, Section 2.5 uses the pressure and particle velocity estimations from each method to derive expressions for energy-based quantities based on auto spectra, cross spectra, and the phase of the transfer function for a two- and three-microphone energy probe.

2.2 Estimating pressure at the center of the microphone array

The energy calculation depends on the pressure at the center of the microphone array, which can be found in several ways. In this thesis, two scenarios are considered. Either a microphone at the center of the probe configuration directly measures the pressure, or an average over the complex pressure at several microphones provides the estimate of the pressure at the center of the probe configuration. Weiderhold et al.⁴⁶ suggested and examined various other alternatives for estimating pressure. The options vary from choosing a single microphone offset from the center to be the pressure estimate for all directions, to estimating the pressure and particle velocity using an orthogonal pair of microphones, to averaging the complex pressures from multiple microphones surrounding the center of a probe. Pascal and Li⁵⁰ suggested that this last option results in the least bias error overall.

This thesis also utilizes this last option of averaging complex pressure from multiple microphones surrounding the center. In practice, a truncated Taylor series is used to find the pressure estimate at a point in space. The series is truncated because only a finite number of microphones are used to estimate the pressure at the center of those microphone positions. An example of this method for a one-dimensional two microphone probe follows.

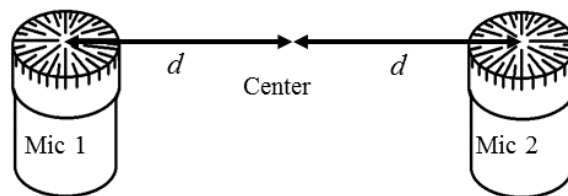


Figure 2.1. A two-microphone energy probe with spacing d from the probe center to a microphone.

To estimate the pressure at the center of the two-microphones, Taylor series expansions of the pressure at microphones a distance d and $-d$ from the center (as shown in Figure 2.1) are considered

$$\tilde{p}(d) = \tilde{p}(0) + d\tilde{p}^{(1)}(0) + \frac{d^2}{2}\tilde{p}^{(2)}(0) + \dots, \quad \text{Eq. 2.1}$$

$$\tilde{p}(-d) = \tilde{p}(0) - d\tilde{p}^{(1)}(0) + \frac{d^2}{2}\tilde{p}^{(2)}(0) + \dots, \quad \text{Eq. 2.2}$$

where $\tilde{p}(d)$ is the pressure at location d , $\tilde{p}(0)$ is for location at the center, and $\tilde{p}^{(n)}(0)$ is the n th derivative evaluated at the center. By adding Eq. 2.1 and Eq. 2.2 together, an approximation for the pressure at the center of the probe, $\tilde{p}(0, \omega)$, using only two-microphones can be found.

$$\tilde{p}(0) \approx \frac{\tilde{p}(d) + \tilde{p}(-d)}{2} + \mathcal{O}(d^2). \quad \text{Eq. 2.3}$$

Thus, the estimate of the pressure at the center is dependent on the average of the complex pressures from the microphones surrounding the probe. Similar results can be found for multidimensional probes where the microphones are equally spaced around the center. Furthermore, with more microphones, the second derivative or higher could be used to better estimate the center pressure. This thesis does not thoroughly study energy probes with sufficient numbers of microphones to use higher-order estimates.

For the probes studied in this thesis, the center, \vec{r}_c , of the probe is defined as

$$\vec{r}_c = \frac{1}{N} \sum_{k=1}^N \vec{r}_k, \quad \text{Eq. 2.4}$$

where \vec{r}_k is the k th microphone location, relative to the source location, and N is the total number of microphones used in the probe. Pressure and particle velocity are estimated at the probe center and then used in the energy-based calculations. Again, to emphasize the scope of this work, this expression works for a select group of probes where the microphones are equidistant from the

center and equally distributed around the center and there are not so many microphones that higher-order derivatives could be used in the estimation. Perhaps this criterion is too stringent, but it allows the analysis of the two- and three-microphone one-dimensional probes in Chapters 2 and 3 as well as some multi-dimensional probes in Chapter 4. For probe configurations that do not fit this criterion, one would have to derive unique expressions for the Taylor expansion or use an alternative method for estimating pressure by using some sort of weighting scheme or a single microphone located at the center of the probe to obtain the center pressure. In other words, the method of estimating center pressure would be specific to the probe. It is beyond this work to analyze every type of probe configuration. Thus, the probe types are restricted so that an analysis of the two processing methods can be compared. The following discussion shows how the traditional and PAGE methods for calculating various energy quantities determine the pressure at the center of the probe configuration.

If there is no microphone at the center of the probe directly measuring the pressure, then the traditional method for estimating the center pressure using the real and imaginary parts of the complex pressure is

$$\tilde{p}_c(\vec{r}_c, \omega) = \frac{1}{N} \sum_{k=1}^N \tilde{p}_k(\vec{r}_k, \omega), \quad \text{Eq. 2.5}$$

where $\tilde{p}_c(\vec{r}_c, \omega)$ is the complex pressure for angular frequency (ω) at the center (\vec{r}_c) of the probe, and \tilde{p}_k is the pressure at microphone k . This result is a generalization of Eq. 2.3 where the second-order derivatives have been truncated from the expression. It should be noted that there is not necessarily a standard way to estimate the pressure at the center of the probe using the traditional method, but this method agrees with the work of Fahy² and Pavic.³⁵ This allows comparisons in Chapter 3 to be made between the results from Fahy's expressions and those of the PAGE method.

The limitations of the traditional method for estimating center pressure are illustrated in Fig. 2.2 for the case of a plane wave and a two-microphone probe of spacing $2d$ (see Figure 2.1). The complex pressure from the microphone closer to the source \tilde{p}_1 (red), and \tilde{p}_2 (blue) is the complex pressure from the farther microphone. The phase for \tilde{p}_2 is set to zero, because only the relative phase between \tilde{p}_2 and \tilde{p}_1 matters for the bias error. Using the two-microphone traditional method, the center pressure estimate, p_{est} , (green) is the midpoint between the tips of the \tilde{p}_1 and \tilde{p}_2 phasors. At low frequencies, like when $2kd = \pi/4$, the phase is accurate, and there is only a small decrease in magnitude between the estimated center pressure and the actual center pressure (the black 'x'). As frequency increases, like when $2kd = 3\pi/4$, the phase is still correct, but the magnitude has dropped significantly from the correct value. At $2kd = \pi$, the magnitude of the pressure goes to zero. Beyond $2kd = \pi$, initially the phase is π radians out of phase with the correct value but it oscillates between in phase (0 radians) and completely out of phase (π radians). The magnitude also oscillates between being zero magnitude and the correct magnitude. Regardless, the traditional method has significant errors as it approaches and passes the spatial Nyquist frequency (SNF) limit. This limit occurs where the microphone spacing is equal to half a wavelength. The traditional method is not used near or beyond the SNF due to spatial aliasing caused by the microphone spacing.

The PAGE method does a better job of estimating the pressure at the center of the probe because it uses the magnitude and phase of the complex pressures at the microphones to estimate the pressure at the probe's center. The PAGE method works by combining the average of the magnitude with the average of phase from all the complex pressures to form an estimate of the center pressure

$$\tilde{p}_c(\vec{r}_c, \omega) = \left[\frac{1}{N} \sum_{k=1}^N |\tilde{p}_k(\vec{r}_k, \omega)| \right] \exp \left[\frac{j}{N} \sum_{k=1}^N \angle \tilde{p}_k(\vec{r}_k, \omega) \right]. \quad \text{Eq. 2.6}$$

Here $|\tilde{p}_k|$ is the magnitude and $\angle \tilde{p}_k$ is the phase of the k^{th} microphone.

In this expression, a complex number is expressed not in terms of a real and imaginary part, but as a phase and magnitude. Because of the nature of phase, there is some ambiguity of what the phase is. For example, the phase can be $0, 2\pi, 4\pi, \dots$ and each complex number with one of these phases will have the same real and imaginary portions. Because of this ambiguity, the MATLAB function that finds the phase is limited to the range between $(-\pi, \pi]$, but in actuality the phase can be outside this range. Figure 2.2 shows the wrapped and unwrapped phase of a plane wave. While the wrapped phase has discontinuities that produce erroneous phase, the unwrapped version can correctly find the phase. Thus, in order for the phase to be correct, the phase needs to be unwrapped beyond the point where the first discontinuity occurs.

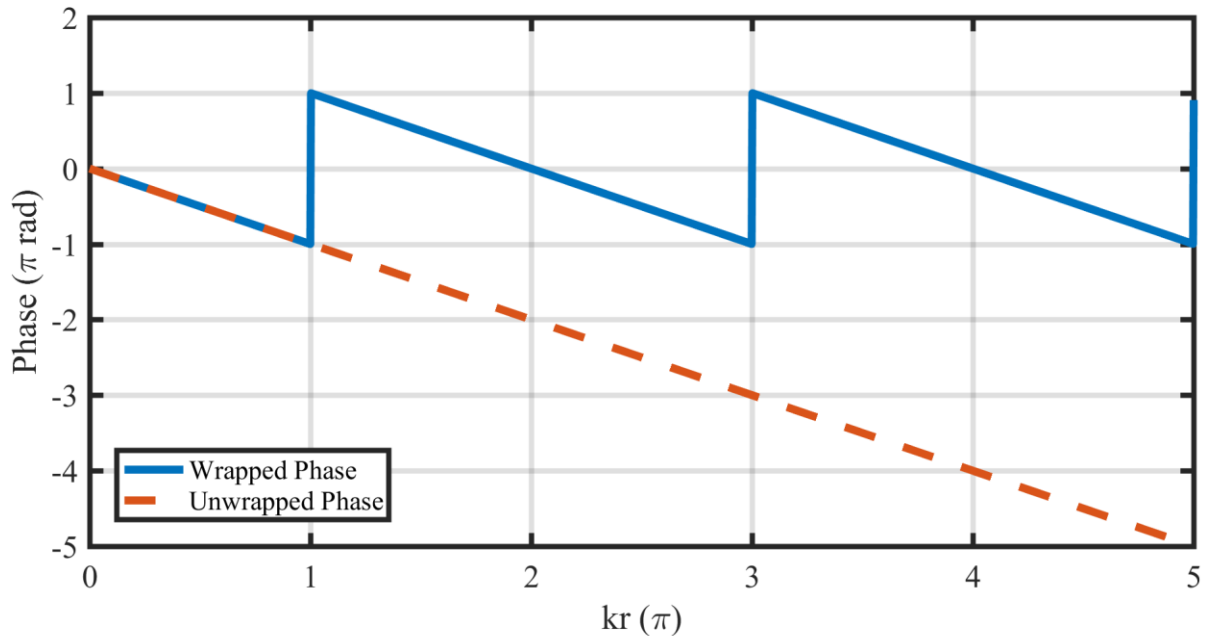


Figure 2.2. The phase for a plane wave as a function of kr for $r = 1m$ and zero initial phase. The wrapped phase has discontinuities at odd multiples of π . The unwrapped phase correctly subtracts 2π to the wrapped phase in order to produce a continuous line.

It should be noted that the phase of the center pressure is not very important to the energy expressions. For acoustic intensity and specific acoustic impedance calculations, the phase of the center pressure cancels out with a term in the particle velocity. This is shown in Eq. A.17, Eq. A.18, and Eq. A.21. Only the magnitude of the complex pressure is used to compute potential energy density (see Eq. A.19). Kinetic energy density uses the difference in phases of the outer microphone's pressures, not the phase of the center pressure (see Eq. A.20). Thus, the actual phase of the center microphone is not important for estimating any of the energy quantities. However, the phase difference between microphones is extremely important for accurately estimating the particle velocity. The phase difference will need to be unwrapped in order to have accurate estimates above the SNF.

Nevertheless, it can be seen in Figure 2.3 how even with unwrapping, the PAGE method can be inaccurate. If the difference in the pressure magnitude between the two-microphones is not a linear relationship, then the average of the magnitude will not match the actual pressure at the center. Likewise, if the phase does not have a linear relationship between the two-microphones, then the average of the phase will be incorrect. For a plane wave field, the estimate is accurate because the pressure phase and magnitude are linear in their spatial relationships, but for other fields this may not be the case. Error introduced by the estimates of the traditional and PAGE methods in such fields are examined in greater detail in Chapter 3. Figure 2.3 simply illustrates how the two methods differ in computing the center pressure and why the error arises in the estimate.

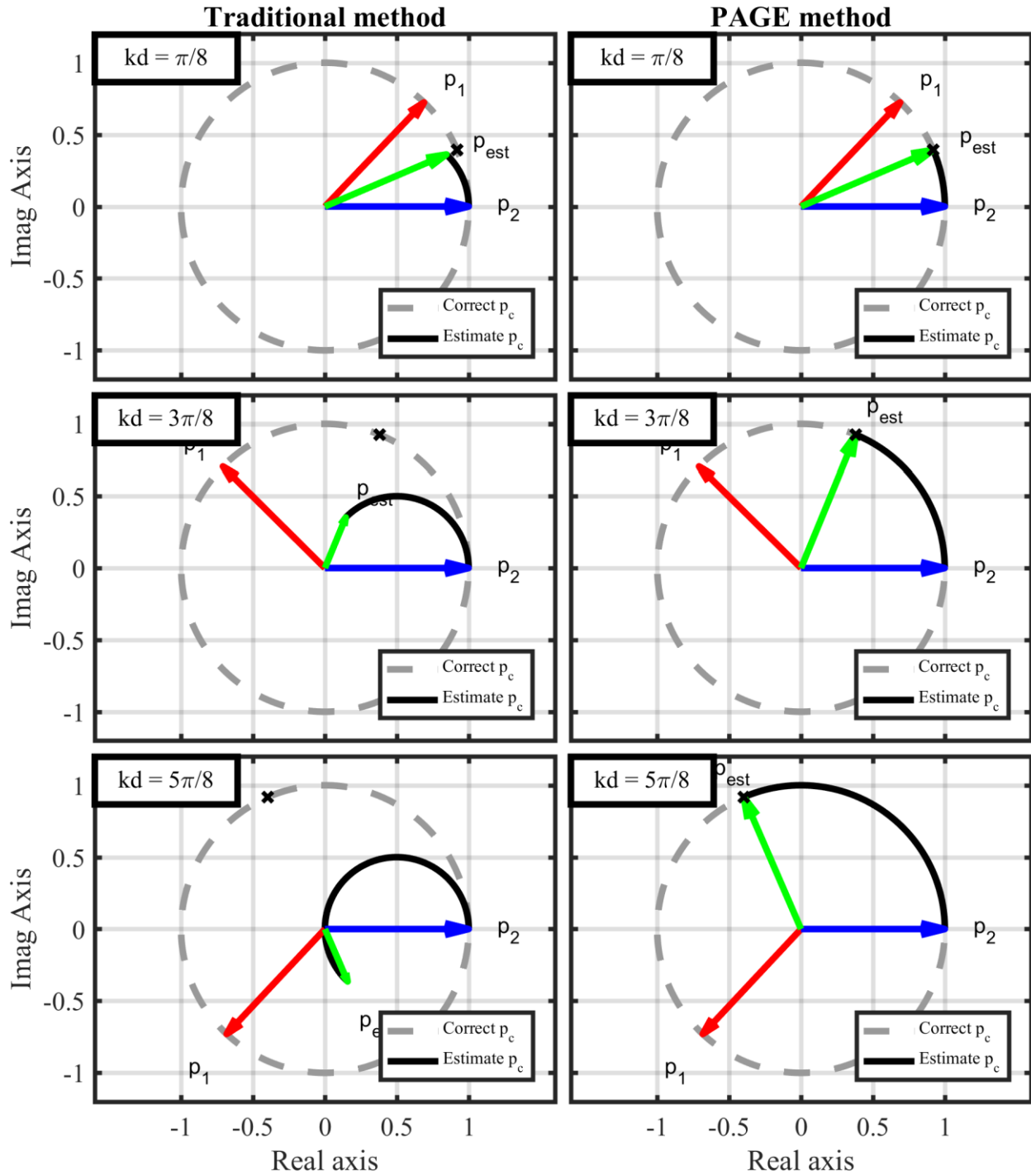


Figure 2.3. Phasor diagram for estimating the center pressure of a plane wave with a two-microphone intensity probe using both the traditional (left) and the PAGE (right) processing methods. The dashed grey line shows the path the correct center pressure follows, while the black line shows the path the actual estimate traces out for the specific method. The black x shows the correct center pressure for the particular wavenumber (k) and microphone spacing (a). The red and blue vectors show the relative phasors for the first and second microphone, respectively. The green line is the estimate of the center pressure at the particular kd value.

2.3 Estimating the pressure gradient

Both the traditional method and the PAGE method estimate the gradient of the complex pressure at location \vec{r} , by using several closely spaced microphones. A Taylor series^{50, 58} is used to make a first-order approximation of the gradient of the complex pressure

$$\tilde{f}(\vec{r}_j) = \tilde{f}(\vec{r}_i) + (\vec{r}_j - \vec{r}_i) \cdot \nabla \tilde{f}(\vec{r}_i, \omega) + \text{H. O. T.}, \quad \text{Eq. 2.7}$$

where $\tilde{f}(\vec{r}_j)$ is the complex number at point \vec{r}_j , and $\tilde{f}(\vec{r}_i)$ is the complex number at point \vec{r}_i , $\nabla \tilde{f}(\vec{r}_i)$ is the gradient of the complex numbers and is the vector we are trying to estimate, and $(\vec{r}_j - \vec{r}_i)$ is the spatial vector that points from point \vec{r}_i to \vec{r}_j . Lastly, H.O.T. stands for higher order terms and includes all the higher order derivatives.

The expression in Eq. 2.7 can be applied to a multi-microphone probe.^{52, 53} For N microphones, there are $NP = N(N - 1)/2$ pairs of microphones leading to a system of equations that can be written in matrix form:

$$\nabla f(\vec{r}_c, \omega) \approx (R^T R)^{-1} R^T \Delta F, \quad \text{Eq. 2.8}$$

where

$$R = \begin{bmatrix} \vec{r}_2 - \vec{r}_1 \\ \vdots \\ \vec{r}_N - \vec{r}_{N-1} \end{bmatrix} \quad \text{Eq. 2.9}$$

is the matrix of difference in positions between all pairs of microphones, and

$$\Delta F = \begin{bmatrix} f(\vec{r}_2) - f(\vec{r}_1) \\ \vdots \\ f(\vec{r}_N) - f(\vec{r}_{N-1}) \end{bmatrix} \quad \text{Eq. 2.10}$$

is the difference in the quantities at the corresponding locations. These expressions allow the gradient of pressure, and therefore the particle velocity, to be estimated for an arbitrary probe configuration.

2.4 Estimating particle velocity

In order to estimate the gradient of pressure, Euler's equation, which relates the particle velocity to the gradient of pressure, can be used. The time-harmonic form of Euler's equation can be expressed as

$$\vec{u}(\vec{r}, \omega) = \frac{j}{\omega \rho_0} \nabla \tilde{p}(\vec{r}, \omega), \quad \text{Eq. 2.11}$$

where $\vec{u}(\vec{r}, \omega)$ is the frequency domain particle velocity vector at location \vec{r} , $j = \sqrt{-1}$, ω is the angular frequency, ρ_0 is the density of air, and $\tilde{p}(\vec{r}, \omega)$ is the frequency-domain pressure at location \vec{r} .

For the traditional method, the particle velocity is estimated using the finite difference of the complex pressure over the distance separation, $2d$. For the two-microphone probe, this can be written as

$$\vec{u}(\vec{r}, \omega) \approx \frac{j}{\omega \rho_0} \frac{\tilde{p}_2 - \tilde{p}_1}{2d}, \quad \text{Eq. 2.12}$$

where \tilde{p}_2 is the complex pressure from microphone 2, and \tilde{p}_1 is the complex pressure from microphone 1 and $2d$ is the separation between the microphones. For multi-dimensional probes, the result is similar

$$\vec{u}(\vec{r}, \omega) \approx \frac{j}{\omega \rho_0} (R^T R)^{-1} R^T \Delta \tilde{p}, \quad \text{Eq. 2.13}$$

where $\Delta \tilde{p}$ is the difference in complex pressure for each pair of microphones, and X is the matrix of the paired spatial differences between microphones.

In the PAGE method, the gradient of pressure can be rewritten in a different form. First, the complex pressure is written in terms of magnitude and phase as

$$\tilde{p}(\vec{r}, \omega) = P(\vec{r}, \omega) \exp(j\phi(\vec{r}, \omega)), \quad \text{Eq. 2.14}$$

where $\tilde{p}(\vec{r}, \omega)$ is the complex pressure at location \vec{r} and angular frequency ω . $P(\vec{r}, \omega)$ and $\phi(\vec{r}, \omega)$ are the magnitude and phase, respectively, of the complex pressure at the same location and frequency. This allows the pressure gradient to be found using the product rule to obtain

$$\nabla \tilde{p}(\vec{r}, \omega) = \exp[j\phi(\vec{r}_c, \omega)] [\nabla P(\vec{r}, \omega) + jP(\vec{r}_c, \omega)\nabla\phi(\vec{r}, \omega)]. \quad \text{Eq. 2.15}$$

This expression is then substituted into Euler's equation to obtain an estimate of particle velocity, written without the dependence on (\vec{r}, ω) as

$$\vec{u}(\vec{r}, \omega) \approx \frac{\exp(j\phi_c) [j(R^T R)^{-1} R^T \Delta P - P_c (R^T R)^{-1} R^T \Delta\phi]}{\omega \rho_0}. \quad \text{Eq. 2.16}$$

Because the particle velocity estimate at the probe's center is being estimated, ϕ_c is the estimate of the phase at the center of the probe, and P_c is the estimate of the pressure magnitude at the center of the probe. The gradients of the magnitude and phase are written using Eq. 2.8, where ΔP is the vector with the difference in pressure magnitude between microphone pairs, and $\Delta\phi$ is the phase difference between pairs of microphones. From this expression, it is seen that the real part of the particle velocity depends on the gradient of phase, and the imaginary part depends on the gradient of the pressure magnitude.

The phasor diagrams for particle velocity in the case of a plane wave give insight into how each method works. Figure 2.4 shows the correct particle velocity as the dashed gray circle. The black line shows the path the processing method follows as frequency increases. The traditional method falls off as frequency increases, but the PAGE method is completely accurate for a plane wave.

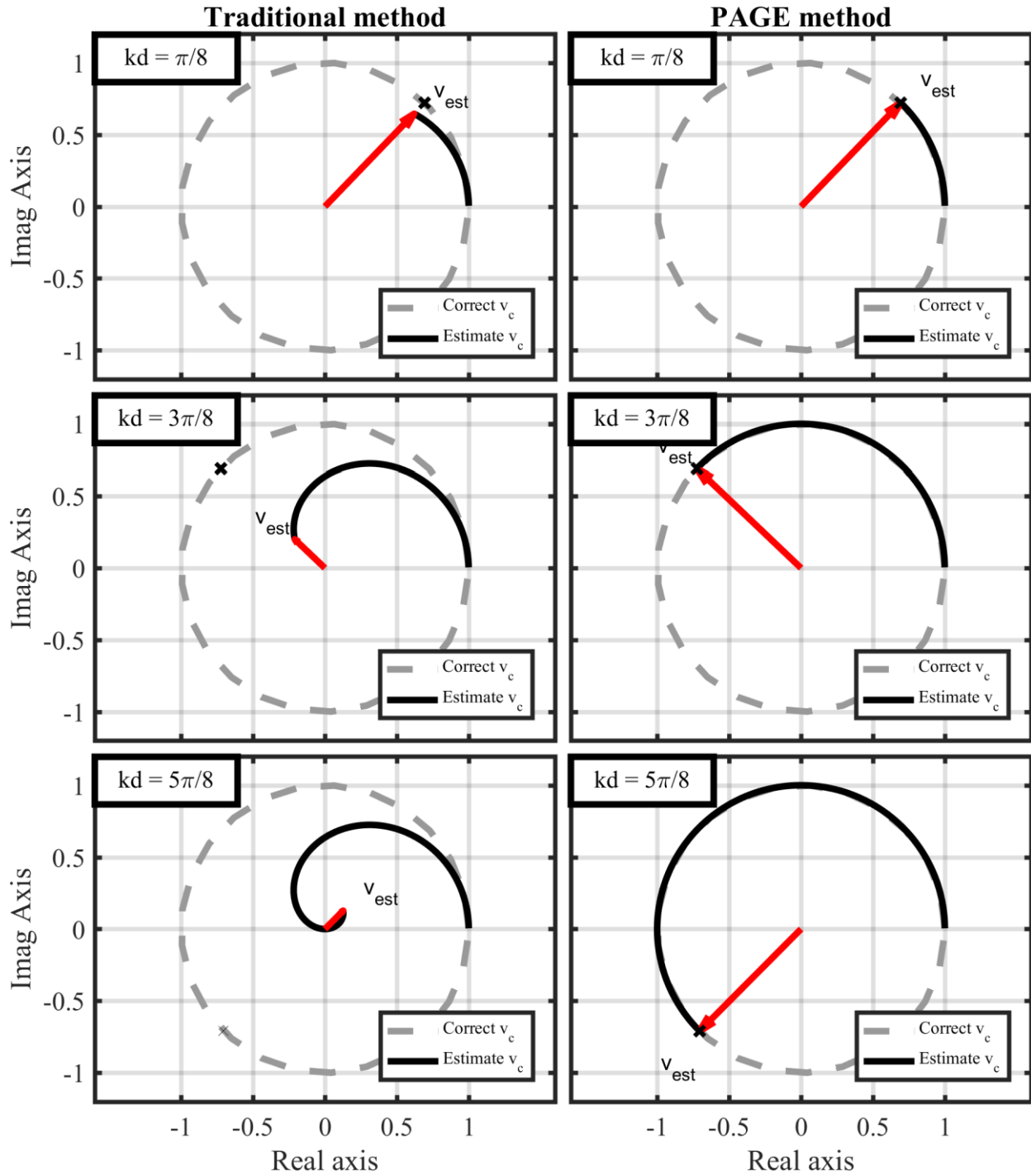


Figure 2.4. Phasor diagram for estimating the particle velocity of a plane wave with a two-microphone intensity probe using both the traditional (left) and the PAGE (right) processing methods. The dashed gray line represents the path of the actual particle velocity. The black line shows the path of the estimation, and the black x marks the correct value. The traditional method's magnitude falls off as frequency increases. Also, beyond the SNF, the phase of the particle velocity using the traditional method is π radians out of phase. The PAGE method with unwrapping has no bias error for the plane wave case.

2.5 Obtaining Energy-based Quantities from Experimental Data

In practice, energy quantities are found using ensemble-averaged data to reduce the effects of measurement noise. Expressions for the energy quantities in terms of auto and cross spectra and transfer functions between the microphones can be found through rearranging the pressure (Eq. 2.5, Eq. 2.6) and particle velocity (Eq. 2.13, Eq. 2.16) expressions and ensemble averaging. For the two- and three- microphone probe configurations, these expressions are derived for the traditional and PAGE methods below.

For clarification, the following definitions from Bendat and Piersol²⁷ are used for the auto-spectrum, the cross spectrum, and the transfer function. The single-sided auto spectrum for a zero-mean pressure waveform, $p_1(t)$, is defined as

$$G_{11}(\omega) = 2\langle \tilde{p}_1^*(\omega)\tilde{p}_1(\omega)\rangle. \quad \text{Eq. 2.17}$$

The single-sided cross spectrum is similarly

$$G_{12}(\omega) = 2\langle \tilde{p}_1^*(\omega)\tilde{p}_2(\omega)\rangle. \quad \text{Eq. 2.18}$$

Lastly, the ensemble-averaged transfer function may be written as the cross spectrum divided by the auto spectrum

$$H_{12}(\omega) = \frac{G_{12}(\omega)}{G_{11}(\omega)}. \quad \text{Eq. 2.19}$$

2.5.1 Acoustic Intensity

The first energy quantity of interest is the active intensity. The active intensity quantifies the flow of energy through a surface. It has a direction and a magnitude. The general equation for active intensity, $\vec{I}_a(\omega)$, in the frequency domain is

$$\vec{I}_a(\vec{r}, \omega) = \frac{1}{2}\text{Re}\{\tilde{p}(\vec{r}, \omega)\tilde{\vec{u}}^*(\vec{r}, \omega)\}, \quad \text{Eq. 2.20}$$

where $\tilde{p}(\omega)$ is the complex pressure, and $\tilde{u}^*(\omega)$ is the conjugated complex particle velocity at location, \vec{r} , and angular frequency, ω . Mann and Tichy⁵⁵ showed that by writing the pressure in terms of magnitude and phase, the active intensity could also be written as

$$\vec{I}_a(\omega) = \frac{P^2 \nabla \phi}{2\rho_0 \omega}, \quad \text{Eq. 2.21}$$

where P is the pressure magnitude and ϕ is the phase of the complex pressure. This expression is extremely useful for understanding active intensity. Knowledge of the gradient of the phase of the complex pressure leads to a knowledge of the direction of the active intensity vector. The magnitude of active intensity depends on the squared pressure magnitude. Furthermore, it shows that the PAGE method works well at estimating active intensity when the squared pressure is accurate (as is the case when the probe has a microphone at the center) and when the gradient of phase is well approximated. Because, the PAGE method works well even above the SNF, it has been used often in calculating active intensity for broadband sources where phase unwrapping works well.^{14, 15, 53, 56} The active intensity expressions for a two and three-microphone energy probe are given in Table 2.1. The traditional method expressions can be written in terms of the imaginary part of the cross spectrum as shown in Fahy.² The PAGE method expressions can be written in terms of the auto spectrum multiplied by the phase difference between the outer microphones.

The other important intensity quantity is the reactive intensity. Reactive intensity quantifies the non-propagating portion of acoustic power. Reactive intensity is an important quantity in two situations. First, in standing fields, the field is entirely reactive, and second, in the near field of an acoustic source, the field is partially reactive. For a source, the ratio of reactive to active intensity can delineate the near and far fields. The general expression for reactive intensity is

$$\vec{I}_r(\omega) = \frac{1}{2} \text{Im}\{\tilde{p}(\omega)\tilde{u}^*(\omega)\}. \quad \text{Eq. 2.22}$$

Similar to the active intensity, Mann and Tichy⁵⁵ give an equivalent expression for the reactive intensity when the pressure is written in terms of magnitude and phase.

$$\vec{I}_r(\omega) = \frac{-P\nabla P}{2\rho_0\omega}, \quad \text{Eq. 2.23}$$

where P is again the pressure magnitude, and ∇P is the gradient of pressure magnitude. This expression is useful for understanding reactive intensity because unlike active intensity, reactive intensity depends on pressure and the gradient of pressure. Thus, the gradient of the pressure in the field is what determines the direction of the reactive intensity.

Table 2.2 gives the expressions for reactive intensity for a two and three-microphone probe. The two-microphone probe has the same results regardless of the choice in processing methods. The three-microphone probe has similar results between processing methods. The traditional method takes the difference between the real part of the cross spectra while the PAGE method takes the difference between the magnitude of the cross spectra.

While the expressions for single-sided intensity estimates from a two- and three-microphone probe are given in the tables, the full derivation for these and following quantities are in Appendix A. The active and reactive intensities for the two-microphone probe match those of Fahy.² Chapter 3 discusses the advantages of these methods and the differences in the accuracy of estimating active and reactive intensity.

Table 2.1. Expression for single-sided active intensity for the two and three-microphone one dimensional probe using both the traditional and PAGE methods.

Active Intensity	Traditional Method	PAGE Method
2 mic	$-\frac{\text{Im}\{G_{12}\}}{2d\rho_0\omega}$	$\frac{(\sqrt{G_{11}} + \sqrt{G_{22}})^2 \arg\{H_{12}\}}{4d\rho_0\omega}$
3 mic	$\frac{\text{Im}\{G_{21}\} + \text{Im}\{G_{32}\}}{4d\rho_0\omega}$	$-\frac{G_{22} \arg\{H_{13}\}}{4d\rho_0\omega}$

Table 2.2. Expression for single-sided reactive intensity for the two- and three- microphone one-dimensional probe using both the traditional and PAGE methods.

Reactive Intensity	Traditional Method	PAGE Method
2 mic	$\frac{G_{11} - G_{22}}{4d\rho_0\omega}$	$\frac{G_{11} - G_{22}}{4d\rho_0\omega}$
3 mic	$\frac{\text{Re}\{G_{21}\} - \text{Re}\{G_{32}\}}{4d\rho_0\omega}$	$\frac{ G_{21} - G_{32} }{4d\rho_0\omega}$

2.5.2 Energy density

In addition to calculating intensity, it is useful to use energy quantities like potential and kinetic energy densities to describe an acoustic field or source. Potential energy density is

$$E_p(\vec{r}, \omega) = \frac{|\tilde{p}(\vec{r}, \omega)|^2}{4\rho_0 c}, \quad \text{Eq. 2.24}$$

where $|\tilde{p}|$ is the magnitude of the single-sided complex pressure. Kinetic energy density has a similar expression,

$$E_k(\vec{r}, \omega) = \frac{\rho_0}{4} |\tilde{u}(\vec{r}, \omega)|^2, \quad \text{Eq. 2.25}$$

where $|\tilde{u}|$ is the magnitude of the particle velocity. The addition of the potential and kinetic energy densities equals the total energy density. When the total energy density is multiplied by a factor of c , it is approximately equal to the active intensity in the far field.⁵⁹

Differences can be seen between the traditional and PAGE methods by comparing the expressions for potential energy density for the two methods, shown in Table 2.3. If there is a microphone at the center of the probe, then both methods produce the same potential energy density expressions. The expressions for the two-mic probe for the two methods are nearly identical, but the traditional method relies on the real part of G_{12} while the PAGE method uses the magnitude of G_{12} . Chapter 3 investigates the relative error caused by using either estimation.

Table 2.3. Expressions for single-sided potential energy density for the two and three-microphone one-dimensional probe using both the traditional and PAGE methods

Potential Energy Density	Traditional Method	PAGE Method
2 mic	$\frac{G_{11} + 2\text{Re}\{G_{12}\} + G_{22}}{8\rho_0 c^2}$	$\frac{G_{11} + 2 G_{12} + G_{22}}{8\rho_0 c^2}$
3 mic	$\frac{G_{22}}{2\rho_0 c^2}$	$\frac{G_{22}}{2\rho_0 c^2}$

The estimation of the kinetic energy density has quite complicated expressions, particularly for the PAGE method, as shown in Table 2.4. Nevertheless, both methods depend on the auto spectra of the outer microphones as well as the cross spectra between the two outer microphones. Also, the PAGE method has a $(\nabla P)^2$ and a $(P\nabla\phi)^2$ term for the kinetic energy density term, which leads to much more complicated expressions. All of the expressions depend on the auto spectra and the cross spectrum of the outer microphones. Again, the traditional method uses the real part of the cross spectrum, while the PAGE method used the magnitude.

Table 2.4. Expressions for single-sided kinetic energy density for the two and three-microphone one dimensional probe using both the traditional and PAGE methods.

Kinetic Energy Density	Traditional Method	PAGE Method
2 mic	$\frac{G_{22} + G_{11} - 2\text{Re}\{G_{12}\}}{8\omega^2\rho_0d^2}$	$\frac{1}{8\omega^2\rho_0d^2} \left[(G_{11} + G_{22} - 2 G_{12}) + \frac{G_{11} + G_{22} + 2 G_{12} }{4} (\arg\{H_{12}\})^2 \right]$
3 mic	$\frac{G_{33} + G_{11} - 2\text{Re}\{G_{13}\}}{8\omega^2\rho_0d^2}$	$\frac{1}{8\omega^2\rho_0d^2} [(G_{11} + G_{33} - 2 G_{13}) + G_{22}(\arg\{H_{13}\})^2]$

2.5.3 Specific acoustic impedance

The specific acoustic impedance for a one dimensional field is also an important acoustic quantity. It is defined as

$$\tilde{z}(\vec{r}, \omega) = \frac{\tilde{p}(\vec{r}, \omega)}{\tilde{u}(\vec{r}, \omega)}. \quad \text{Eq. 2.26}$$

In order to estimate the specific acoustic impedance, average Eq. 2.26 over several blocks of data. An alternative is to use the energy quantities²² already derived:

$$\tilde{z}(\vec{r}, \omega) = \frac{2\rho_0c^2E_p}{I_a - jI_r} = \frac{\rho_0(I_a + jI_r)}{2E_k}. \quad \text{Eq. 2.27}$$

These alternate expressions are found by multiplying the top and bottom of Eq. 2.26 by either the pressure or particle velocity, respectively. The specific acoustic impedance expressions only work for one dimensional fields where the intensity is not a vector (dividing by a vector is an undefined operation). Alternatively, admittance, which is particle velocity over pressure, can be used as a vector. Lastly, all the different methods of estimating the specific acoustic impedance could give different results because the errors in all the different energy quantities are different.

Besides relating pressure and particle velocity, specific acoustic impedance describes if the acoustic field at location \vec{r} is in the near or far field of a source as a function of ω by a simple comparison to $\rho_0 c$, which is the specific acoustic impedance of a traveling plane wave. In the far field of a source, the specific acoustic impedance approaches $\rho_0 c$. In the PAGE method specific acoustic impedance expressions, the imaginary part of \bar{z} will be significant in the near field, but in the far field, these terms do not contribute as much because they are related to the reactive part of the field. In the far field, the expressions for the PAGE method estimation of specific acoustic impedance approach $\rho_0 c$. For the traditional method, it is harder to find much intuition in the two and three-microphone expressions. Since there are so many ways to find specific acoustic impedance, perhaps another expression would give greater insight.

Table 2.5. The single-sided specific acoustic impedance found using the traditional and PAGE methods.

Specific acoustic impedance	Traditional Method	PAGE Method
2 mic	$-j\omega\rho_0 d \left(\frac{G_{21} + G_{11}}{G_{21} - G_{11}} \right)$	$\frac{2\omega\rho_0 d(G_{11} + G_{22} + 2 G_{12})}{2j(G_{22} - G_{11}) + (G_{11} + G_{22} + 2 G_{12}) \arg\{G_{12}\}}$
3 mic	$-\frac{j2\omega\rho_0 d G_{22}}{G_{32} - G_{12}}$	$\frac{2\omega\rho_0 d G_{22}}{j(G_{23} - G_{21}) + G_{22} \arg\{H_{13}\}}$

These expressions represent the estimations for these acoustic quantities via the traditional and PAGE methods. While only one-dimensional two- and three-microphone probes are analyzed here, any geometrically symmetric intensity probe can have similar expressions derived. Chapter 3 investigates the error of these estimations as compared to the true quantities for known acoustic fields found analytically.

2.6 Conclusion

In Chapter 2, expressions of the estimations for a few acoustic energy-related quantities were found for a two and three-microphone probe using the traditional method and the PAGE method. The process began with either using a microphone at the center of the probe or estimating the pressure at the center of the probe. Then the particle velocity was estimated from the gradient of pressure found by using the two different methods. From pressure and particle velocity, expressions for intensity, energy density, and specific acoustic impedance were found.

The traditional method differs from the PAGE method in its approach. First, in the absence of a center microphone, the traditional method averages the surrounding complex pressures to estimate the center pressure while the PAGE method averages the magnitudes and phases separately to construct an estimate of the center pressure. Second, in the estimation of pressure gradient across the probe, the traditional method uses a finite difference method on the complex pressures while the PAGE method uses a finite difference method on the pressure phase and magnitude, separately.

The differences between the PAGE and traditional methods for pressure and particle velocity estimation lead to the acoustic energy quantity expressions containing similar differences. The energy expressions from the traditional method often use the real or imaginary part of the cross spectrum, while the PAGE method uses the magnitude and phase of the cross spectrum (the argument of the transfer functions is the same as the phase of the cross spectrum). Since the traditional method uses the real or imaginary part of the cross spectrum, a frequency dependence is introduced. This is seen in greater detail in Chapter 3 where the accuracy of these different expressions is examined against the true expressions for various acoustic fields.

Chapter 3

Application to different analytical acoustic sources

3.1 Introduction

The traditional and PAGE methods can be used to provide estimates for energy-based acoustic quantities based on measurements made by multi-microphone probes of various configurations. The expressions for the estimates are given in Chapter 2 and derived in Appendix A for one-dimensional two and three-microphone probes. Here, the accuracy of these estimates is evaluated by comparing the traditional and PAGE estimates to the analytical values for the energy-based quantities in known acoustic fields. This thesis investigates the bias errors in the computations of the two methods, but does not consider other sources of error, such as measurement noise, microphone phase mismatch bias,⁵² or probe scattering.²⁹

Bias error from inexact estimates of the pressure and particle velocity lead to errors in the calculation of energy quantities. These bias errors are dependent on the type of source or field where the measurements are taken. In this chapter, the bias errors for a plane wave, a standing wave, and a monopole are explored. The plane wave case is important because it shares common characteristics with what is expected in the far field of a free-field source. The standing wave is entirely reactive, so this case gives insight into the near field of an acoustic source, where the reactive field is dominant. Finally, the monopole case has both near- and far-field regions, and the amplitude of the pressure dissipates with distance. Acoustic sources are often modeled as one or more monopoles, making this case an important consideration. For all cases, the estimates of

the traditional method are compared to those of the PAGE method. A two-microphone and a three-microphone probe are used in this analysis. Figure 3.1 depicts these one dimensional probes. The position of the probe relative to the origin is r . For the monopole case, the source is a point source at the origin. The outer microphones are each a distance d from the center of the probe. The difference between the probes is that the three-microphone probe has a microphone at the center of the probe, but the spacing of the outer microphones is the same for each probe.

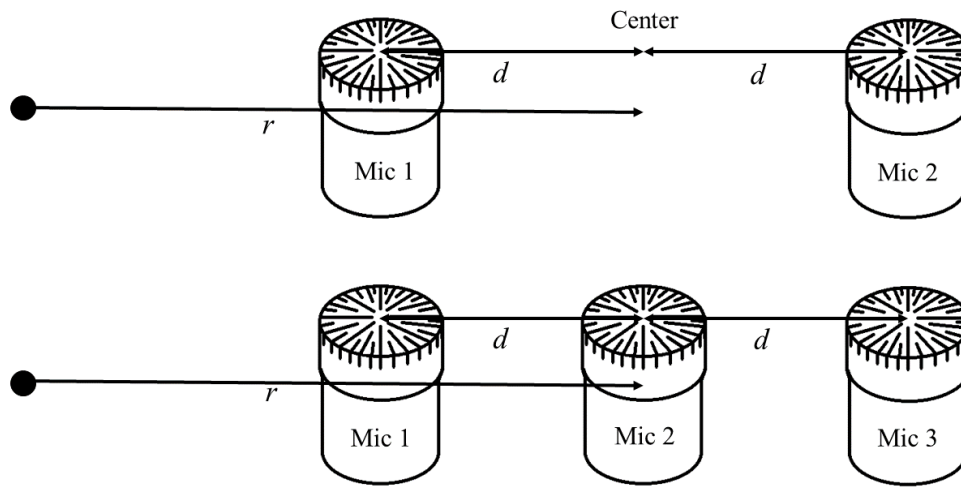


Figure 3.1. Schematic of the two-microphone one-dimensional probe (top) and the three-microphone probe (bottom) one-dimensional probe. r is the distance from the origin to the center of the probe, and d is the distance from the center of the probe to the outside microphones.

This chapter proceeds by discussing the analytical expressions of the energy-based quantities for the different sources. This is followed by an analysis of the relative error, which is the ratio of the ideal (perfectly phase-matched microphones with no scattering and no noise) estimate of the energy quantity over the analytical solution for each energy quantity. This leads to an understanding of the patterns of error when using the traditional or PAGE methods. Also, it shows for which cases it is advantageous to have a center microphone in the probe configuration.

All of this ultimately gives insight into optimal probe designs and analysis methods in arbitrary fields. In order to understand the frequency bandwidth differences between the PAGE and the traditional method, an error criterion of 0.5 dB is used. A half decibel is used because it corresponds to a relative error of $\pm 10\%$. The point at which the relative error exceeds 0.5 dB is the upper limit of the frequency range for which the estimate of the energy-based quantity is valid.

3.2 Plane wave

The plane wave is an important case as it is one of the simplest fields but also represents the characteristics of the far field of many free-field sources. For a plane wave, the pressure and particle velocity are in phase with each other, all the energy is propagating, and there is no near-field region or reactive intensity. Furthermore, the sound levels do not change with distance, which makes the pressure magnitude gradient zero. Lastly, for a specific frequency, the phase is proportional to position, meaning the gradient of phase is a constant. Due to these properties, the different processing methods have different errors because of their different approaches to analyzing the field. The traditional method has greater error near the spatial Nyquist frequency (SNF), but the PAGE method with unwrapping has no error at any frequency for the plane wave case.

3.2.1 Analytical expressions

In order to make comparisons to the energy quantity estimates, it is first important to understand the analytical expressions for a one-dimensional plane wave propagating in the r direction with complex pressure: $\tilde{p}(r, \omega) = A \exp(-jkr)$. The wavenumber $k = \omega/c$ and the position r can be written as vectors, but the one-dimensional case considered here does not require that distinction. If instead the plane wave was obliquely incident on the measurement

probe, then vector notation would be necessary. The analytical expressions for the pressure, particle velocity, active and reactive intensity, potential and kinetic energy density, and specific acoustic impedance are shown in Table 3.1, where the subscript A denotes an analytical expression. The expressions for the plane wave's pressure and particle velocity are similar because the particle velocity is in phase with the pressure. For the plane wave, the specific acoustic impedance is $\rho_0 c$ where ρ_0 is the density of air and c is the speed of sound in air. The active intensity expression is amplitude squared divided by the specific acoustic impedance. The reactive intensity is zero. The potential and kinetic energy density expressions are equivalent, and when added together, the sum differs from the active intensity by a factor of c .

Table 3.1. Analytic expressions for acoustic quantities in the acoustic field of a propagating plane wave.

	\tilde{p}_A	$\vec{\tilde{u}}_A$	\vec{I}_{aA}	\vec{I}_{rA}	E_{pA}	E_{kA}	\tilde{z}_A
Analytic Expressions	Ae^{-jkr}	$\frac{A}{\rho_0 c} e^{-jkr}$	$\frac{A^2}{2\rho_0 c}$	0	$\frac{A^2}{4\rho_0 c^2}$	$\frac{A^2}{4\rho_0 c^2}$	$\rho_0 c$

3.2.2 Traditional and PAGE method error expressions

With this understanding of the nature of a plane wave and its energy quantities, the relative error of estimating a plane wave's pressure, particle velocity, and the various energy quantities is presented for the traditional and PAGE methods.

3.2.2.1 Pressure relative error

When utilizing measurements made with a two-microphone probe, both methods need to estimate the pressure at the center of the probe. The relative error for each method using a two-microphone probe was calculated and is shown in Table 3.2. The pressure relative error expression for the two-microphone probe processed using the traditional method matches the

results of Fahy.² When the separation between the microphones is small compared to wavelength, the traditional method has little error in estimating the center pressure. This was demonstrated in Figure 2.3. Another visualization is in Figure 3.2, which shows the relative magnitude error and difference in phase for pressure as a function of kd . Remembering that d is the distance between the center and the outer microphones, and that the SNF corresponds to the frequency at which the distance between the outside microphones equals half a wavelength, then the SNF occurs when $2kd = \pi$, or $kd = \pi/2$. At the SNF, the complex pressures from each of the outer microphones sum to zero. Because the traditional method sums the pressures from the microphones by summing the real and imaginary components, it has a relative error of negative infinity decibels. When $4kd = \pi$, or when the signals received at the two-microphones are $\frac{\pi}{2}$ radians out of phase, the traditional method's relative error in pressure is -1.5 dB. In fact, the traditional method traces out (black line in Figure 2.3) a circle that corresponds to $\cos(kd)$, which is the relative magnitude error shown in Table 3.2. Thus, whenever $kd = \pi(2n + 1)/2$, the center pressure estimate goes to zero. Above the SNF, both the magnitude and phase of the pressure are incorrect at times with the traditional method. The estimated phase just above the SNF is π radians out of phase with the actual result (see the phase error in Figure 3.2).

On the other hand, for a plane wave, the PAGE method estimates the center pressure by summing the amplitudes and phases of the pressure measured by the microphones. The relative errors of the center pressure estimates using the PAGE method are also shown in Table 3.2. The center pressure estimate using the PAGE method is exact below the SNF. Above the SNF when the phase is unwrapped correctly, the PAGE method's estimate is exact, as displayed in Figure 3.2. Even without phase unwrapping, the PAGE method greatly increases the bandwidth for which intensity can be estimated accurately. With no unwrapping, the PAGE method is accurate

up to the SNF. In this case, the bandwidth (using the 0.5dB criteria) is greatly increased from $0.47kd$ for the traditional method to $1.57kd$ for the PAGE method.

Table 3.2. Relative error for center pressure estimates using the traditional and PAGE method with a two and three-microphone one-dimensional probe for a plane wave. For the two-microphone case, the PAGE estimate with correct phase unwrapping has zero error even above the SNF. Without phase unwrapping, the estimate above the SNF is not used. Therefore, the high frequency limit for the PAGE method without unwrapping is $1.57kd$. With a center microphone, either processing method can go as high in frequency because the pressure is accurately determined.

	Traditional		PAGE	
	2 Mic	3 Mic	2 Mic	3 Mic
$e_p = \frac{\tilde{p}}{\tilde{p}_A} - 1$	$\cos(kd)-1$	0	0	0

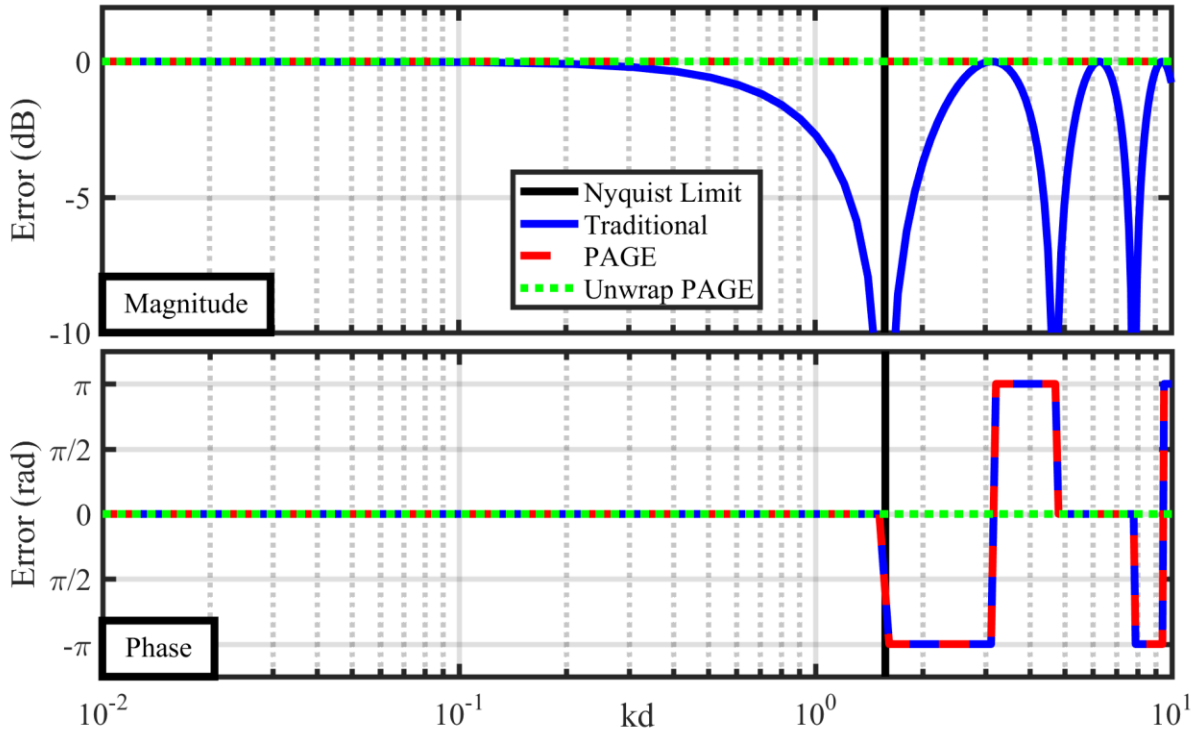


Figure 3.2. The computed magnitude and phase of the relative error ($e_p + 1$) of the complex pressure at the center of a two-microphone intensity probe from different methods. The SNF indicates where the complex pressure measured from the microphones is π radians out of phase. The traditional method estimate of the center pressure magnitude goes to zero at the SNF. Both the unwrapped and wrapped PAGE method have the correct magnitude, but only the unwrapped PAGE method has the correct phase above the SNF.

3.2.2.2 Particle velocity relative error

Similar to the relative errors in pressure estimation, the particle velocity estimate for a plane wave is exact for all frequencies using the PAGE method with unwrapping, but inaccurate for the traditional method at higher frequencies. Both the two and three-microphone traditional method estimations have the same error because the estimate is based on the measurements from the outside microphones only (see Table 3.3). Furthermore, the particle velocity relative error expression for the two-microphone probe again matches Fahy's work.² Figure 3.3 shows that for the traditional method, the particle velocity magnitude falls off more slowly than the pressure magnitude estimate. Instead of going to negative infinity dB at $2kd = \pi$, it goes to negative infinity at $kd = \pi$. This makes sense because the traditional method's estimate of particle velocity is based on subtracting the two complex numbers from the outer microphones. When the distance between the outside microphones is one wavelength, then the pressure difference is zero. Unlike the complex pressure estimate, the traditional method's estimate of the particle velocity never completely returns to zero magnitude error after it falls off (see Figure 3.3).

Table 3.3. The relative error expressions for particle velocity in a plane wave field.

	Traditional		PAGE	
	2 Mic	3 Mic	2 Mic	3 Mic
$e_u = \frac{\tilde{u}}{\tilde{u}_A} - 1$	$\text{sinc}(kd)-1$	$\text{sinc}(kd)-1$	0	0

The unwrapped PAGE method has no errors in its estimate of particle velocity, but the wrapped version has errors similar to the traditional method after the spatial Nyquist limit. The PAGE method's estimate of particle velocity again subtracts the complex pressures from the outer microphones to estimate the gradient of pressure, but does so using the amplitude and phase of the complex values, instead of the real and imaginary parts. Since a plane wave has a

linear pressure gradient, this method always correctly estimates the pressure gradient, and thus the particle velocity. Again the PAGE method increases the usable range of frequencies where particle velocity is accurate. Without unwrapping, the PAGE method has less than 0.5 dB error until the SNF, corresponding to $1.57kd$, compared to $0.82kd$ with the traditional method. Thus, the bandwidth with the PAGE method is almost double that of the traditional method.

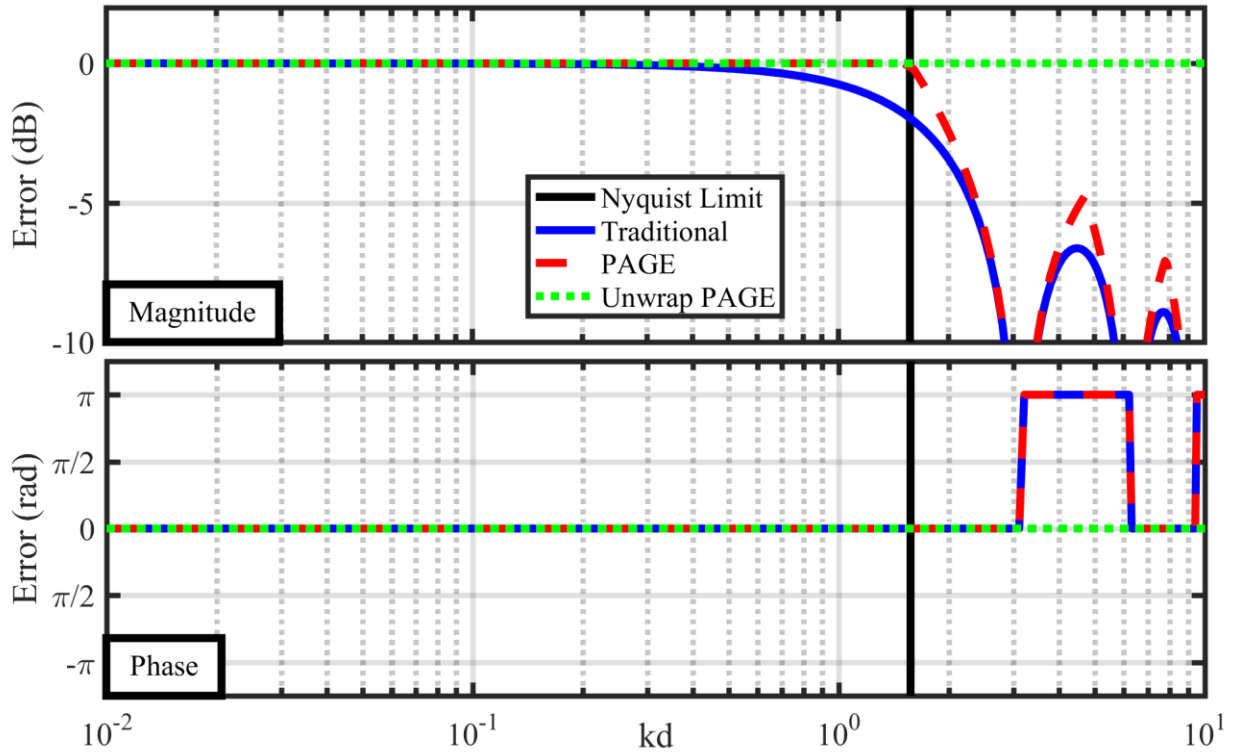


Figure 3.3. The computed magnitude and phase relative error ($e_u + 1$) of the complex particle velocity at the center of a two-microphone intensity probe from different methods. The SNF indicates where the complex particle velocity estimated from the microphones is π radians out of phase. Both the unwrapped and wrapped PAGE methods have the correct magnitude, but only the unwrapped PAGE method has the correct phase above the SNF.

3.2.2.3 Intensity relative error

Since the unwrapped PAGE method has no errors in estimating the center pressure or particle velocity, the energy quantities exactly match the analytical expressions. In contrast, the traditional method's errors in estimating center pressure and particle velocity affect its energy estimates. The relative errors are shown in Table 3.4 and plots of the magnitude and phase errors

are shown in Figure 3.4. For the traditional method, both the two- and three-microphone probes have a sinc-like error. The three-microphone probe has a usable bandwidth that is twice that of the two-microphone probe because the three-microphone probe does not have error in the pressure estimate; it measures the center pressure with the central microphone. Regardless of the errors in the estimates, both methods and both probes all correctly calculate the reactive intensity to be zero.

Table 3.4. Relative error for active and reactive intensity using the traditional and PAGE method with a two- and three-microphone probe. Because the reactive intensity is analytically zero, the relative error for this quantity is not applicable (NA).

	Traditional		PAGE	
	2 Mic	3 Mic	2 Mic	3 Mic
$e_{I_a} = \frac{I_a}{I_{aA}} - 1$	$\text{sinc}(2kd) - 1$	$\text{sinc}(kd) - 1$	0	0
$e_{I_r} = \frac{I_r}{I_{rA}} - 1$	NA	NA	NA	NA

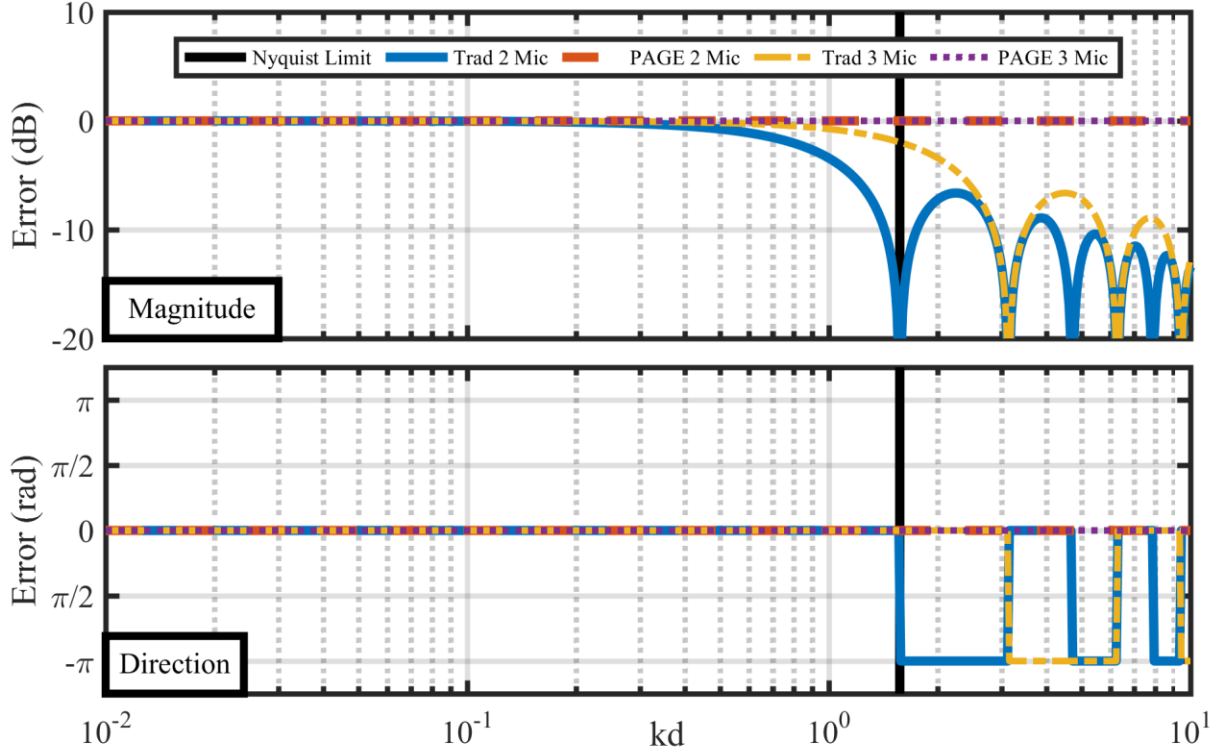


Figure 3.4. Estimates of the active intensity relative error for a plane wave using a two- and three-microphone probe using both the traditional and PAGE methods. The PAGE method's estimations (with phase unwrapping) are exactly equivalent to the analytical expressions, so no error is produced. The traditional method's errors in pressure and particle velocity estimation lead to errors in active intensity estimation. The three-microphone probe does not have errors in pressure estimation, extending the usable bandwidth to twice that of the two-microphone probe.

A comparison of the usable frequency range of the traditional method to the PAGE method shows the increase the PAGE method offers in estimating active intensity. First, using a center microphone for the traditional method doubled the usable frequency range from $0.41kd$ to $0.82kd$ (see Table 3.4). Without unwrapping, the PAGE method is accurate until the SNF, which is double the bandwidth from the three-microphone traditional processing method. With unwrapping, the PAGE method can extend the usable frequency range past the SNF.⁵⁶

3.2.2.4 Energy density relative error

The relative error in the total energy density for a plane wave depends on both the potential and kinetic energy densities. The only time there is a relative error for potential energy density is when the data is processed using the traditional method and there is no center

microphone. All other cases correctly estimate the center pressure magnitude, so their estimates of potential energy density are also correct. Since potential energy density depends on the squared pressure magnitude, its relative error falls off more quickly than that of the pressure estimate. For the kinetic energy estimate, the traditional method has the same error for both probes because they had the same error in the particle velocity estimate. Again, because the PAGE method correctly estimates pressure and particle velocity, its estimate of kinetic energy density is also correct.

Table 3.5. Relative error expressions for potential and kinetic energy density using the traditional and PAGE method with a two and three-microphone probe.

	Traditional		PAGE	
	2 Mic	3 Mic	2 Mic	3 Mic
$e_{E_p} = \frac{E_p}{E_{p_A}} - 1$	$\cos^2(kd) - 1$	0	0	0
$e_{E_k} = \frac{E_k}{E_{k_A}} - 1$	$\text{sinc}^2(kd) - 1$	$\text{sinc}^2(kd) - 1$	0	0

The relative errors for potential and kinetic energy density for a plane wave for the different methods and probe configurations are listed in Table 3.5 and displayed in Figure 3.5. For potential energy density, the two-microphone probe with traditional processing has 0.5 dB error at $0.34kd$. This is a significantly lower bandwidth than the three-microphone probe, which measures the pressure at the center, and the two-microphone probe with PAGE processing. The kinetic energy density high frequency limit is $0.58kd$ for either probe using the traditional method, while the PAGE obtains good estimates up to the SNF without unwrapping, and above the SNF when the phase is unwrapped correctly. Similarly, the relative error in the total energy density is shown in Figure 3.6. There is no error for the PAGE method, but the traditional method rolls off more quickly for the two-microphone probe than for the three-microphone

probe. Thus, a probe with a center microphone should be used for energy density estimates for more accurate results.

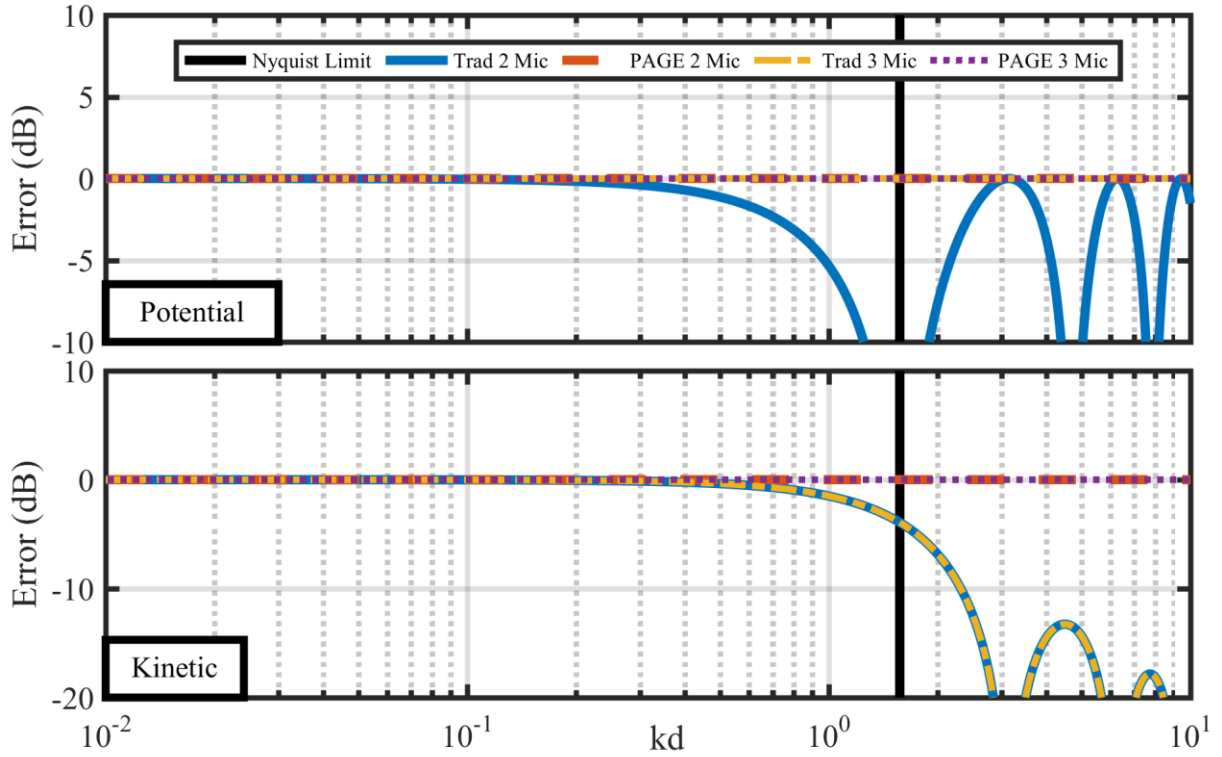


Figure 3.5. The relative error for estimates of the potential (top) and kinetic energy density (bottom) for a plane wave.

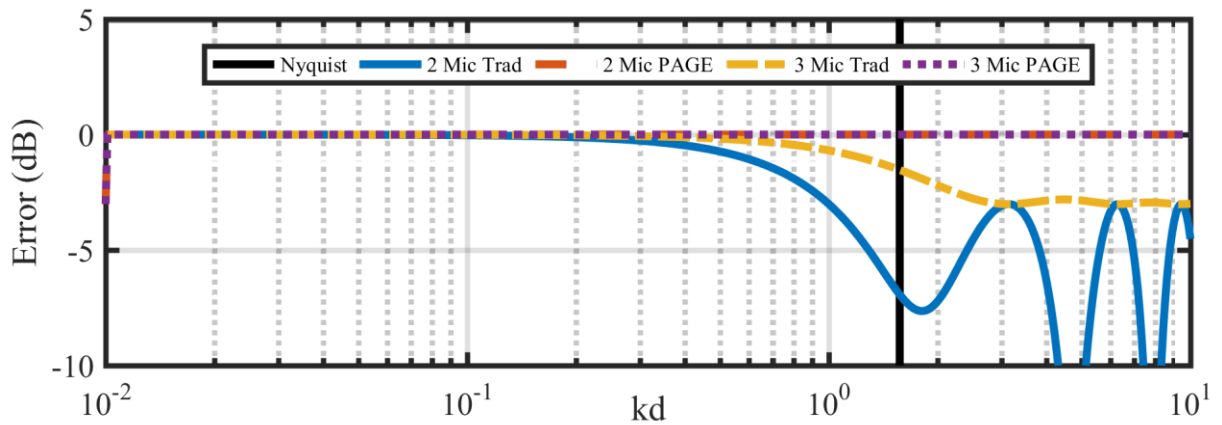


Figure 3.6. The relative error in the total energy density for a plane wave using the different probes and processing methods.

3.2.2.5 Specific acoustic impedance relative error

Lastly, the specific acoustic impedance error for the traditional method can be quite dramatic. Since the particle velocity estimate can go to zero, the specific acoustic impedance relative dB error can range from negative to positive infinity. Therefore, the specific acoustic impedance can really only be used at low frequencies far from the SNF. For the two-microphone probe using the traditional method, the specific acoustic impedance is accurate until $0.57kd$ while the three-microphone probe fails the 0.5 dB criterion at $0.82kd$. Both of these are significantly lower than the SNF, at which the PAGE method without unwrapping is able to accurately estimate specific acoustic impedance. With correct phase unwrapping, the PAGE method accurately estimates the specific acoustic impedance above the SNF. It should be noted that the specific acoustic impedance for the traditional method is highly dependent on the method of calculation. In Section 2.5.3, three different methods were given for calculating specific acoustic impedance. Since these three different methods (Eq. 2.26-Eq. 2.27) depend on different quantities, the error in specific acoustic impedance will differ depending on which expression is used.

Table 3.6. Relative error for specific acoustic impedance using the traditional and PAGE method with a two- and three-microphone probe.

	Traditional		PAGE	
	2 Mic	3 Mic	2 Mic	3 Mic
$e_z = \frac{\tilde{z}}{\tilde{z}_A} - 1$	$\frac{\cos(kd)}{\text{sinc}(kd)} - 1$	$\frac{1}{\text{sinc}(kd)} - 1$	0	0

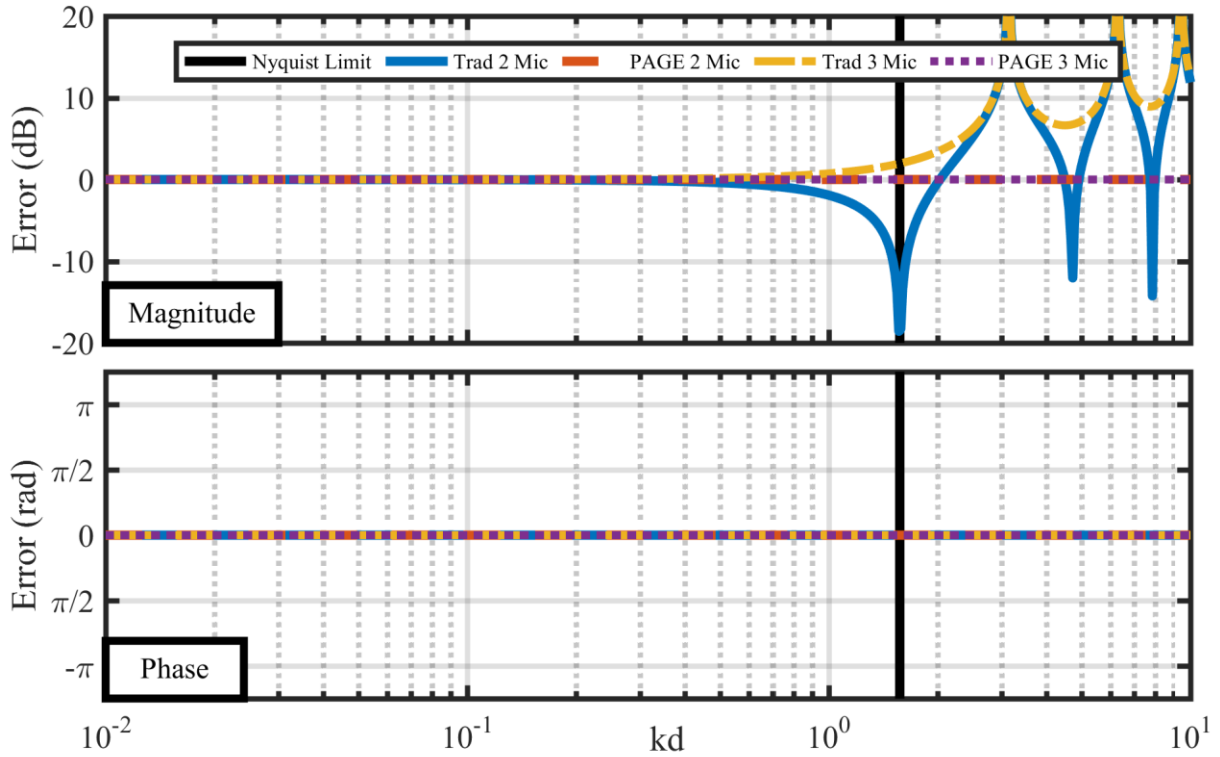


Figure 3.7. The relative error in the specific acoustic impedance for a plane wave using the different probes and processing methods. The top plot shows the magnitude error, and the bottom plot shows the discrepancy in phase.

3.3 Standing wave

3.3.1 Analytical Expressions

Since this work is mainly concerned with propagating waves, the standing wave is not central to this work. However, the standing wave field analysis should give some insight into how well the traditional and PAGE methods perform in the acoustic near field of a source where the field is largely reactive. There are some differences between a standing wave and the reactive field near a source. The reactive field of a propagating wave generally falls off quickly while a standing wave is always reactive. Future work will more thoroughly analyze standing waves and

reverberant rooms and lead to an understanding of how the PAGE method could be used to find energy densities in various rooms with standing-wave-like fields.

The magnitudes of the various energy quantities in a standing wave field depend on the measurement location: near a null or a peak or somewhere in between. Additionally, the particle velocity and pressure are in quadrature everywhere in the field, which means there is no active intensity. The analytical expressions for the energy-based quantities are given in Table 3.7.

Table 3.7. Analytic expressions for pressure, particle velocity, active intensity, reactive intensity, potential energy density, kinetic energy density, and specific acoustic impedance in an infinite standing wave field. The active intensity is zero because a standing wave does not propagate.

	\tilde{p}_A	\tilde{u}_A	I_{aA}	I_{rA}	E_{pA}	E_{kA}	\tilde{Z}_A
Analytic Expressions	$A \cos(kr)$	$\frac{-A \sin(kr)}{\rho_0 c}$	0	$\frac{A^2}{4\rho_0 c} \sin(2kr)$	$\frac{A^2 \cos^2(kr)}{4\rho_0 c^2}$	$\frac{A^2}{4\rho_0 c^2} \sin^2(kr)$	$j\rho_0 c \cot(kr)$

3.3.2 Error expressions

A standing wave can be thought of as the superposition of two plane waves traveling in opposite directions. Therefore, Fahy² concluded that similar error expressions exist for the standing wave field as for the plane wave field. Likewise, the relative error expressions for pressure, particle velocity, and the energy quantities in Table 3.8 are the same as for the plane wave case. With only two microphones, it is impossible to estimate the center pressure using a Taylor series with more than the first terms (the mean of the pressures). Likewise, the gradient of pressure can only be estimated as the difference between the pressures. This truncation of all the other Taylor series terms is only valid for $kd \ll 1$. Nevertheless, this work is trying to expand the bandwidth to the SNF and beyond. Before comparing the PAGE method to the traditional method, it is important to first explore the error for the traditional method caused by the truncation of the Taylor series.

First, for the two-microphone probe, the center pressure has to be estimated. As Table 3.7 indicates, the pressure equals $\cos(kx)$. Thus, the pressure at the center is $\tilde{p}_c = \cos(kx_c)$, the pressure at the first microphone is $\tilde{p}_1 = \cos(k(x_c - d))$, and the pressure at the second microphone is $\tilde{p}_2 = \cos(k(x_c + d))$, where k is the wavenumber, x_c is the center of the probe, and d is the spacing from the center to each outer microphone. Then the relative error, e_p , for pressure is

$$e_p = \frac{\tilde{p}_2 + \tilde{p}_1}{2\tilde{p}_c} = \frac{\cos(kx_c + kd) + \cos(kx_c - kd)}{2\cos(kx_c)} = \cos(kd), \quad \text{Eq. 3.1}$$

where a sum-to-product trigonometry identity was used. This surprising expression indicates that the error only depends on the spacing of the probe and not the location of the probe in the standing field. There is one caveat. When the center of the probe is on a node, the error actually goes to zero regardless of the probe size. The problem is when the probe center is on a node, $\cos(kx_c) = 0$. Therefore, the above expression ends up being zero divided by zero.

Nevertheless, except for when the center of the probe is on a node, the error for the center pressure estimate only depends on probe spacing and not location. To further emphasize this point, the Taylor series can be used to estimate the error. Combining Eq. 2.1 and Eq. 2.2 and dividing both sides by 2 produces

$$\frac{\tilde{p}(x_c + d) + \tilde{p}(x_c - d)}{2} = \tilde{p}(x_c) + \frac{d^2}{2!}\tilde{p}^{(2)}(x_c) + \frac{d^4}{4!}\tilde{p}^{(4)}(x_c) + \dots \quad \text{Eq. 3.2}$$

Now if $\tilde{p}(x) = \cos(kx)$, then the above expression turns into

$$e_p = \frac{\cos(k(x_c + d)) + \cos(k(x_c - d))}{2\cos(kx_c)} = \left(1 - \frac{(kd)^2}{2!} + \frac{(kd)^4}{4!} \dots\right) \quad \text{Eq. 3.3}$$

$$= \cos(kd).$$

The Taylor expansion of $\cos(kd)$ was used to show that the Taylor series and the trigonometric identity both gave the same result: the relative error is dependent on the spacing of the

microphones and not the position. A similar procedure gives the traditional method's relative error for particle velocity as $\text{sinc}(kd)$. (See Table 3.8 for all the relative error expressions. As will be shown, the PAGE method and the traditional method give the same error expressions as long as the PAGE method does not span an odd number of nodes in the standing wave). Thus, the relative error is the same as the plane wave case and depends on the probe spacing. It is almost always position independent. The exceptions are when estimating the pressure, if the probe is on a node, $\cos(kx_c) = 0$ and there is no error. When estimating particle velocity, if the probe is centered on an antinode, $\sin(kx_c) = 0$, then the error is zero.

Table 3.8. The relative error for estimates of energy quantities for an infinite standing wave. The traditional and PAGE method give identical results as long as the probe does not span a null (microphones not closely spaced), otherwise the PAGE method gives worse results than the traditional method. Because the active intensity is zero, the relative error for this quantity is not applicable (NA).

Traditional and PAGE	2 Mic.	3 Mic.
e_p	$\cos(kd) - 1$	0
e_u	$\text{sinc}(kd) - 1$	$\text{sinc}(kd) - 1$
e_{I_a}	NA	NA
e_{I_r}	$\text{sinc}(2kd) - 1$	$\text{sinc}(kd) - 1$
e_{E_p}	$\cos^2(kd) - 1$	0
e_{E_k}	$\text{sinc}^2(kd) - 1$	$\text{sinc}^2(kd) - 1$
e_z	$\frac{\cos(kd)}{\text{sinc}(kd)} - 1$	$\frac{1}{\text{sinc}(kd)} - 1$

The next step in understanding the relative error for the standing wave case is to determine the relative error in the estimate of center pressure for a two-microphone probe using the PAGE method and the relative error in the estimate of particle velocity from the PAGE method. Because the PAGE method averages the magnitude and phase of the pressure on the outer microphones, the location of the microphone relative to nodes in the standing field is

important. If the microphones do not span an odd number of nodes, then the two outside microphones are in phase, and the center pressure estimate is exactly the same as the traditional method. But when the microphones do span an odd number of modes, the estimate is incorrect.

In Figure 3.8, the relative error for the center pressure using the two processing methods is shown. As can be seen in the figure, the PAGE and traditional method are the same for the portions of the plot when the two-microphones do not span an odd number of nodes. When the microphones do span an odd number of nodes, the phase error changes by $\pi/2$ radians. This comes from averaging the phase from the two-microphones that are π radians out of phase. In addition, at some kd , the probe is centered on a node. In this case, the PAGE method averages the magnitudes, which are non-zero. The actual magnitude is zero, so when the relative error is calculated, the relative magnitude error explodes, because the finite PAGE estimate is divided by zero. Thus, the PAGE method has some regions (the probe microphones span an odd number of nodes) where the result is completely wrong.

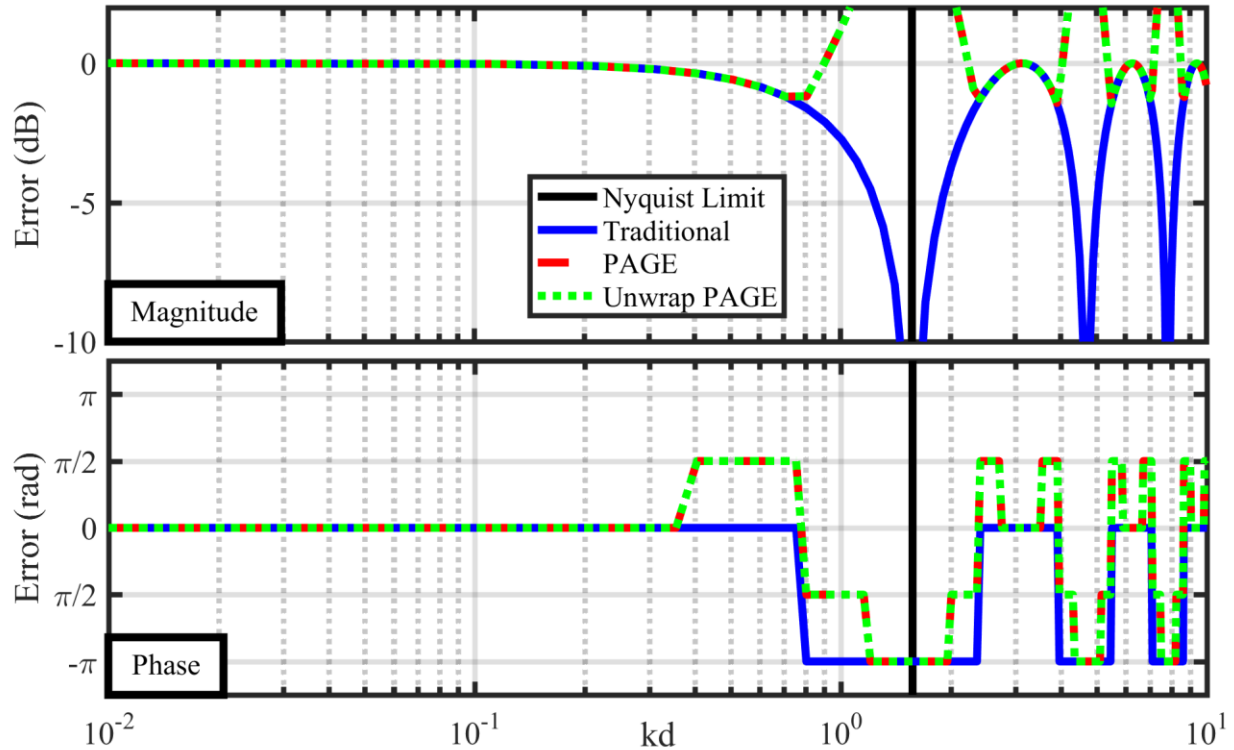


Figure 3.8. The relative pressure error for a standing wave using two-microphones to estimate the center pressure. When the microphones span a node, the PAGE method averages the phase of the center microphone to be $\pi/2$ radians. Furthermore, as the actual center of the probe approaches a node, the PAGE method overestimates the magnitude and the relative error blows up. When the PAGE method does not have jumps, it follows the traditional method. The traditional method rolls off exactly like the plane wave case.

In order to estimate the particle velocity, the PAGE method needs to accurately measure the center pressure magnitude, the gradient of phase, and the gradient of pressure. Each of these quantities can contribute to the error. The gradient of phase will be wrong if the probe spans an odd number of nodes, in which case the phase difference between microphones will be π radians. Otherwise, the phase difference will be zero, which is the correct phase difference. Except for the jumps that arise from the phase, the particle velocity calculated from the PAGE method depends solely on the gradient of the pressure magnitude. Since the pressure is entirely real, the gradient of the pressure magnitude is the same as the estimated gradient used in the traditional method. Thus, the two processing methods get the same results except for when the PAGE method has large errors from an inaccurate phase difference. Figure 3.9 shows the estimates of the particle

velocity from both methods. The PAGE method follows the traditional method except for when it breaks down because it spans an odd number of nodes.

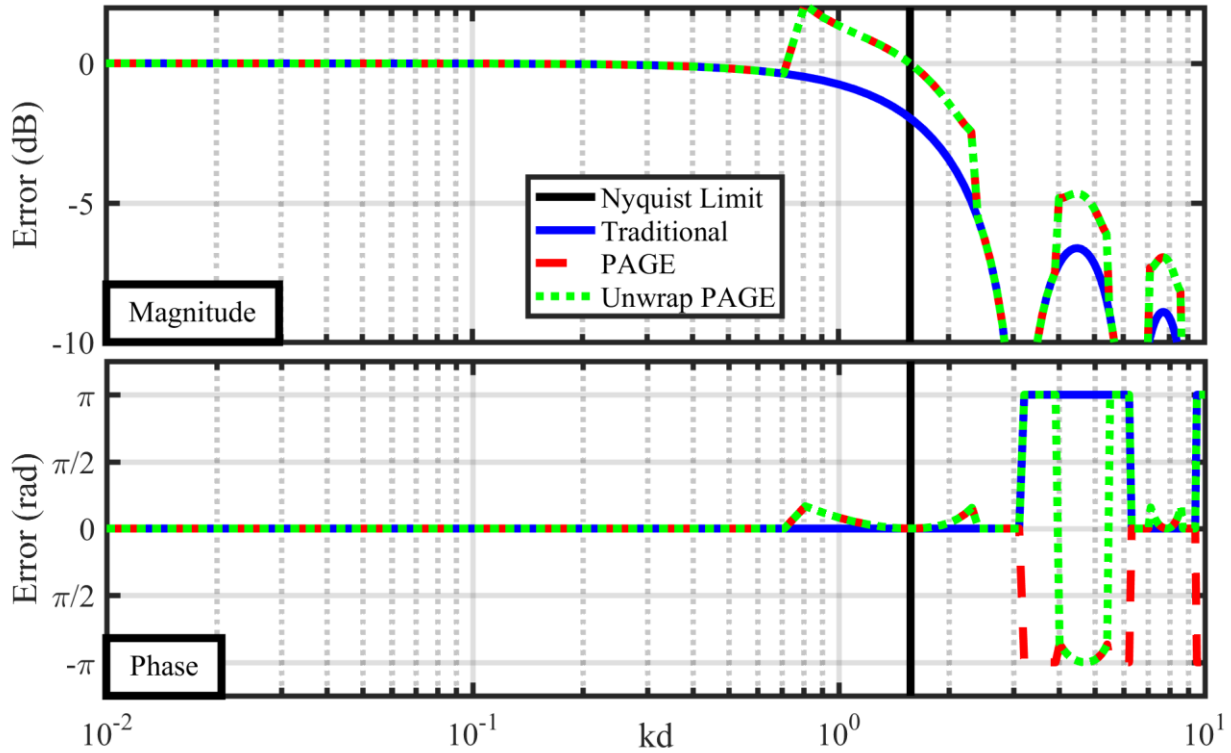


Figure 3.9. The relative particle velocity error for a standing wave using two-microphones to estimate the center pressure. The nodes of the standing wave cause jumps in the phase and magnitude for the PAGE method. Despite the jumps, the PAGE method follows the trend of the traditional method. The traditional method rolls off like in the plane wave.

Now that the relative error for a standing wave has been explored, the various energy quantities can be compared for the PAGE and the traditional method. First, to calculate the active intensity, the traditional method uses Eq. 2.20. Since the pressure is completely real and the particle velocity is completely imaginary, the real part of the product is zero. For the PAGE method, the active intensity is proportional to the gradient of phase. As long as the probe does not span an odd number of nodes, the difference in the phase for the outer microphones will be zero. Thus, both methods under the right conditions accurately calculate the active intensity to be zero as it should be. Since the PAGE method gives the same result for pressure and particle velocity as the traditional method for certain regions, then the rest of the energy quantities should

be the same. Outside those certain regions, the PAGE method is completely wrong, and so the results are meaningless.

This is a preliminary investigation into the performance of the PAGE method in reverberant fields. This analysis suggested that the current implementation of the PAGE method would perform as well as the traditional method at lower frequencies and worse near the SNF. A standing wave was examined, but a more realistic approach would be to investigate a mixture of standing and plane waves. This would allow the nulls to not go completely to zero and the phase difference would not always be 0 or π radians. The errors in this case might not be as significant. There is still a lot of work to be done with the PAGE method and reverberant fields. The results here indicate that for a perfect standing wave the PAGE method performs worse than the traditional method, and the PAGE method does not agree with the plane wave expressions, because it breaks down at position dependent locations.

3.4 Monopole

3.4.1 Analytical Expressions

The often complicated fields of acoustic sources are regularly analyzed in terms of a compilation of simple sources, or monopoles. For this reason, an analysis of the characteristics of the field from a monopole can be very insightful into how well different computation methods meant for analyzing complicated sources perform. The analytical expressions for the energy-based quantities in the case of a monopole source are listed in Table 3.9. One notable characteristic of the field from a monopole is that $|\tilde{p}|^2 \propto r^{-2}$. Not surprisingly, since the active intensity is related to $|\tilde{p}|^2$, the active intensity likewise falls off as r^{-2} . The reactive intensity falls off even more quickly as r^{-3} (see Table 3.9), so it is only significant near the source. The far field of a monopole is similar to the field of a plane wave. This means that the study of a

monopole source yields insight into how the PAGE method and traditional methods perform both near the source where the reactive field is still significant and there is a high degree of curvature to the wave fronts, and far from the source where the active field dominates.

Table 3.9. Analytic expressions for the energy quantities in the field of a monopole.

	\tilde{p}_A	\tilde{u}_A	\tilde{I}_{aA}	\tilde{I}_{rA}	E_{pA}	E_{kA}	\tilde{z}_A
Analytic Expressions	$\frac{\tilde{A}e^{-jkr}}{r}$	$\frac{\tilde{A}(-j + kr)e^{-jkr}}{\rho_0\omega r^2} \hat{r}$	$\frac{ A ^2}{2\rho_0cr^2} \hat{r}$	$\frac{ A ^2}{2\rho_0\omega r^3} \hat{r}$	$\frac{ \tilde{A} ^2}{4\rho_0c^2r^2}$	$\frac{ \tilde{A} ^2(1 + k^2r^2)}{4\rho_0c^2k^2r^4}$	$\frac{\rho_0c(kr)}{kr - j}$

3.4.2 Error expressions

The relative error for all the quantities of interest depends on the proximity to the source and the spacing between the microphones. An expression that appears quite commonly in the error expressions is

$$\beta = \frac{1}{1 - \left(\frac{kd}{kr}\right)^2}. \quad \text{Eq. 3.4}$$

Because β depends only on d and r , a relative error factor of β indicates that if the probe radius is large compared to wavelength, or if the distance to the source is small compared to the wavelength, then there is a greater non-frequency dependent bias error.

3.4.2.1 Pressure relative error

The expressions for the traditional method's estimates of center pressure and particle velocity are quite complicated. As

Table 3.10 shows, the relative error for the pressure estimate is a complex number and dependent on kd , r , and β . The latter of these is the bias error for proximity to the source and the probe spacing. This factor lessens as kr increases and as kd decreases. For small probe spacing, the results approach unity (no error).

Table 3.10. Relative error for pressure using the traditional and PAGE method with a two and three-microphone probe for the monopole case. Also, the expected location (kd) where the error exceeds ± 0.5 dB is listed. For relative error functions where the error theoretically never exceeds 0.5 dB, nothing is listed. If there is a center microphone, then the results should be accurate for the frequency range over which the microphone frequency response is relatively flat. If there is no center microphone and phase unwrapping is not applied, the PAGE method estimates for the center pressure are good until $kd = \pi/2$, the spatial Nyquist limit.

	Traditional		PAGE	
	2 Mic	3 Mic	2 Mic	3 Mic
e_p	$\beta \frac{r \cos(kd) + jd \sin(kd)}{r} - 1$	0	$\beta - 1$	0

The error in estimating complex pressure in the field from a monopole with a two-microphone probe analyzed by both the traditional and PAGE methods is shown in Figure 3.10. As kd increases, the traditional method has increasingly larger errors in pressure magnitude and phase estimation. However, unlike the plane wave case, the magnitude of the pressure estimate never goes to zero because the pressure falls off as $1/r$ such that the pressure at one microphone (one phasor in Figure 2.2) is larger than the other. This difference in the complex pressure magnitudes also affects the phase of the estimate to be incorrectly skewed to the larger complex number.

In contrast, the PAGE method has no error in phase estimation, due to the linear relationship in phase in the field from a monopole. However, the two-microphone probe does have a constant bias error (β) inherent to the results due to the microphone spacing (kd) and the distance from the source (kr). As kd decreases or kr increases, β decreases. This bias error arises because the pressure magnitude falls off as $1/r$, but is estimated by a first-order approximation with the closely spaced microphone locations. Despite this limitation, the PAGE method bias error is frequency independent, unlike that of the traditional method, as shown in Figure 3.10. A comparison of the bandwidth for pressure estimates for a two-microphone probe

shows that the traditional has an error of 0.5 dB at $0.59kd$ while the PAGE method is able to go to the SNF with no error, even without unwrapping.

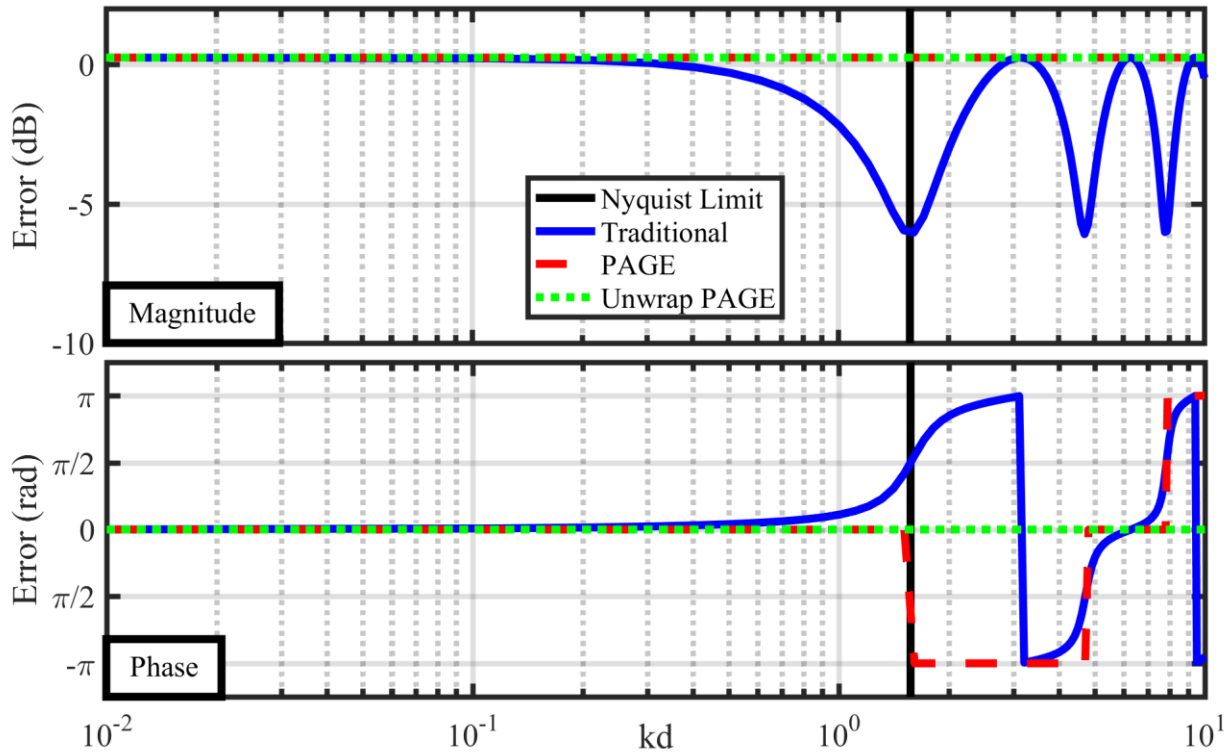


Figure 3.10. The computed magnitude and phase error of complex pressure for a monopole at a distance of $r = 4.3d$, where $d = 2$ cm and is the spacing from one microphone to the center. Both the traditional method and PAGE methods for calculating complex pressure at the center of a two-microphone intensity probe are shown. The SNF indicates where the complex pressures measured from the microphones are π radians out of phase. All methods are affected by the bias error caused by the proximity to the source and the spacing of the probe. Only the unwrapped PAGE method has the correct phase above the SNF.

3.4.2.2 Particle velocity relative error

The error in particle velocity is very similar to that of the plane wave analysis. The monopole field has an additional bias error, as shown in Table 3.11, but similar trends are seen in the estimates of particle velocity from the two fields. The particle velocity magnitude error falls as frequency increases for the traditional method, but the magnitude error is constant for the unwrapped PAGE method results, as displayed in Figure 3.11. The phase error from the traditional method in the monopole field is different from the plane wave case. The particle

velocity phase behaves more like the phase for the complex pressure of a monopole, but the error occurs at a higher frequency. For the two-microphone probe, the usable bandwidth of the traditional method is $0.95kd$ while the PAGE method without unwrapping obtains correct estimates to the SNF. When the phase is unwrapped correctly, the error in the PAGE method estimates for particle velocity at the center of the probe is the bias error independent of frequency.

Table 3.11. The relative error expression for particle velocity for a monopole source.

	Traditional	PAGE	
	2 and 3 Mic	2 Mic	3 Mic
e_u	$\beta \frac{jkr \operatorname{sinc}(kd) + \cos(kd)}{(jkr + 1)} - 1$	$\beta - 1$	$\frac{\beta \left[\frac{(kd)^2}{kr} + j - kr \right]}{j - kr} - 1$

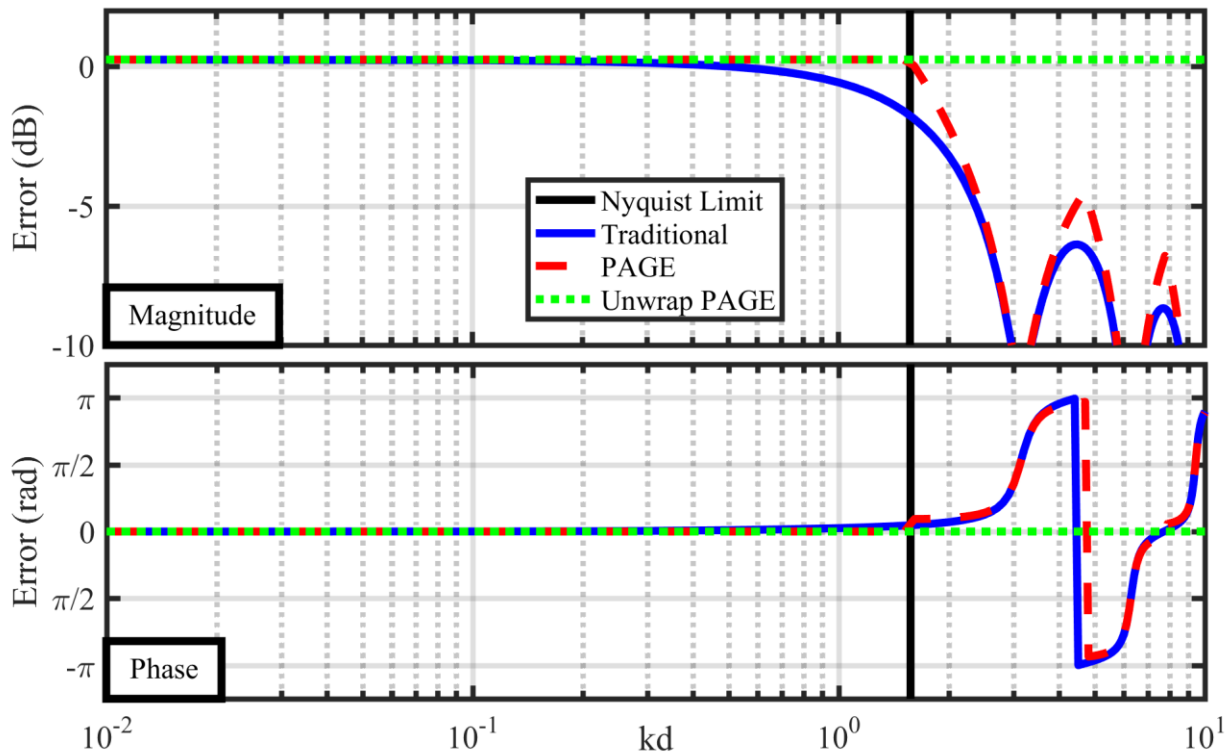


Figure 3.11. The computed magnitude and phase error of particle velocity for a monopole at a distance of $r = 4.3d$. $d = 2$ cm and is the spacing from one microphone to the center. The error for both the traditional method and PAGE methods for calculating particle velocity at the center of a two-microphone intensity probe are shown. The SNF indicates where the microphones are half a wavelength apart, making the phase between their measurements π radians different. All

methods are affected by the bias error caused by the proximity to the source and the spacing of the probe. Only the unwrapped PAGE method has the correct phase above the SNF.

3.4.2.3 Intensity relative error

The relative error for intensity determined by the traditional method is similar to that of the plane wave case, but with the bias error (Table 3.12). As in the plane wave case, the estimate of the active intensity using the traditional method has a sinc term that implies its estimate is accurate for low frequencies but falls off at higher frequencies. As has been seen already, the three-microphone probe has twice the usable bandwidth of the two-microphone probe (see Figure 3.12) because it accurately determines the center pressure. Unlike the plane wave case, the traditional method's estimate of active intensity for the monopole also has a constant bias error (β) caused by the finite distance separating the microphones. The active intensity estimate from the PAGE method for the two-microphone probe also has a constant bias of β^2 , which is frequency independent but larger than the traditional method (see Table 3.12). The three-microphone probe has no error in estimating active intensity using the PAGE method because its estimates of pressure and particle velocity are correct for all frequencies in the monopole field.

Table 3.12. Relative error active and reactive intensity using the traditional and PAGE method with a two and three-microphone probe for the monopole case.

	Traditional		PAGE	
	2 Mic	3 Mic	2 Mic	3 Mic
e_{I_a}	$\beta \text{sinc}(2kd) - 1$	$\beta \text{sinc}(kd) - 1$	$\beta^2 - 1$	0
e_{I_r}	$\beta^2 - 1$	$\beta \cos(kd) - 1$	$\beta^2 - 1$	$\beta - 1$

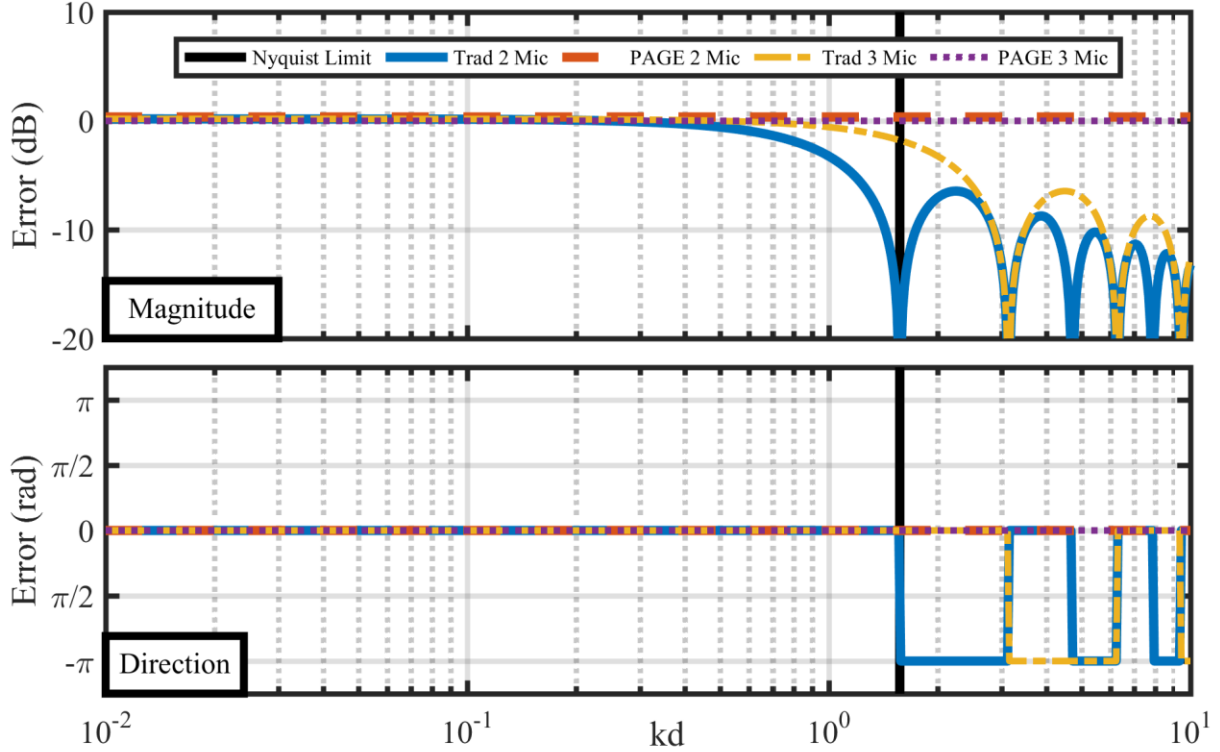


Figure 3.12. Active intensity relative error for different methods and probes for a monopole at a distance of $r = 4.3d$. $d = 2$ cm and is the spacing between the microphone and the center. The top plot shows the magnitude error and the bottom plot shows direction errors.

For propagating fields, the energy probe works best far from the source and with a small probe size, due to the β bias error discussed previously. To analyze this interdependence between probe size and distance, plots of the error as a function of kd and kr are shown in Figure 3.13 for the active intensity. The traditional method active intensity estimate has errors when the probe is close to the source or larger than the wavelength of sound. Likewise, as suggested by Pascal et al.⁵⁰, the bias error gets larger when the probe gets close to the source. Pascal et al. gave the rule as $r > 2h$ as the region where the error was less than 1 dB, but h was defined as the distance between microphones and not the distance from a microphone to the center. Using the same standard, for a bias error of less than 1 dB, the probe-source separation needs to be $4.3d$. In this analysis, it was found that all methods and probes except the PAGE three-microphone probe result in large errors along the line that goes from the bottom left to the

top right corner. This line represents the point where $r = d$. Clearly, the distance from the source cannot equal the probe radius or else a microphone will occupy the same location as the source. Thus, the probe needs to be several probe radii from a monopole for an accurate estimate of the active intensity.

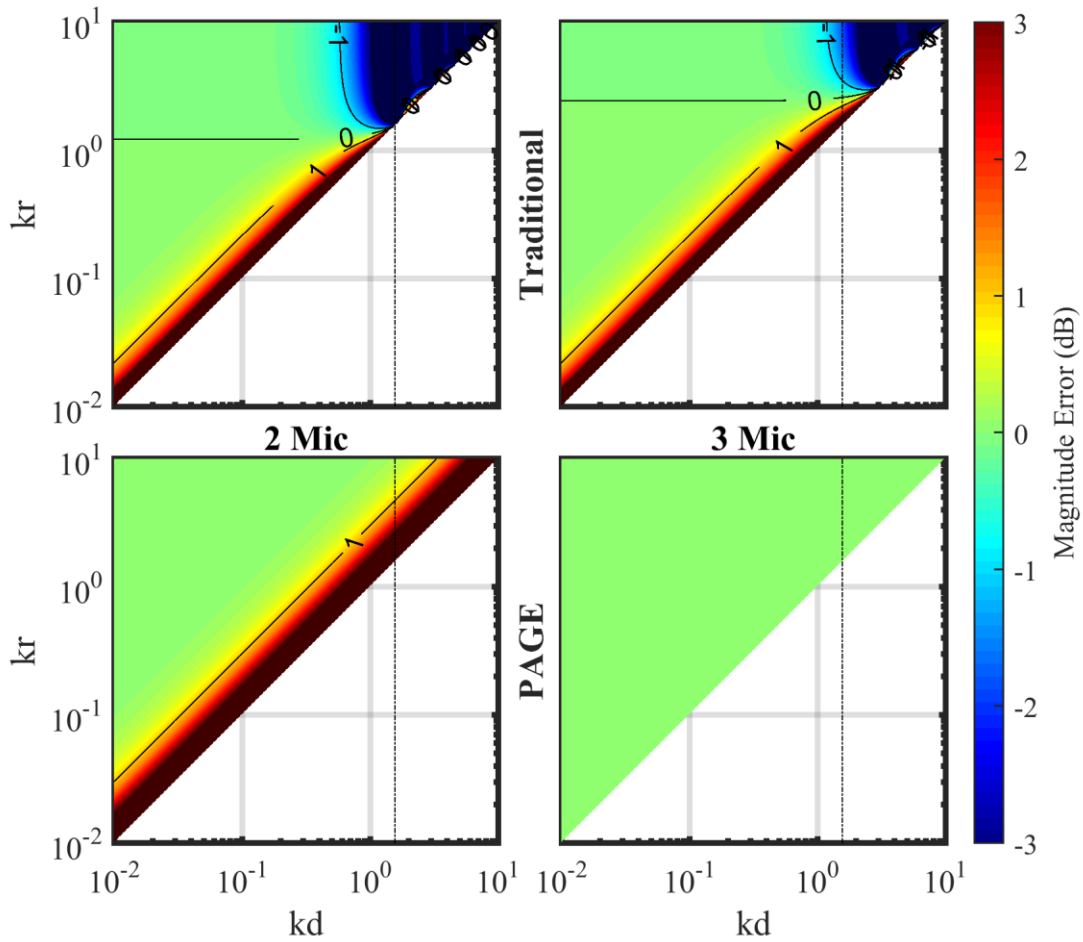


Figure 3.13. Active intensity relative error for the traditional and PAGE methods applied to two and three-microphone probes. The black line is the spatial Nyquist limit. The three-microphone PAGE case has no error in estimating active intensity for all values of kd and kr . The two-microphone probe is susceptible to bias error when the probe is only a few d from the source. The traditional method also breaks down for large values of kd .

Interestingly, the relative errors for estimates of reactive intensity are not frequency dependent except for when the traditional method is used with a three-microphone probe, as displayed in Table 3.12. The traditional method applied to the three-microphone probe depends

on the real part of the two cross spectra, so it is frequency dependent. For the two-microphone probe, the traditional and the PAGE methods have the same bias error for the reactive intensity. (See Figure 3.14 and Table 3.12.) Lastly, the three-microphone probe with PAGE processing has slightly less bias error than the two-microphone probe.

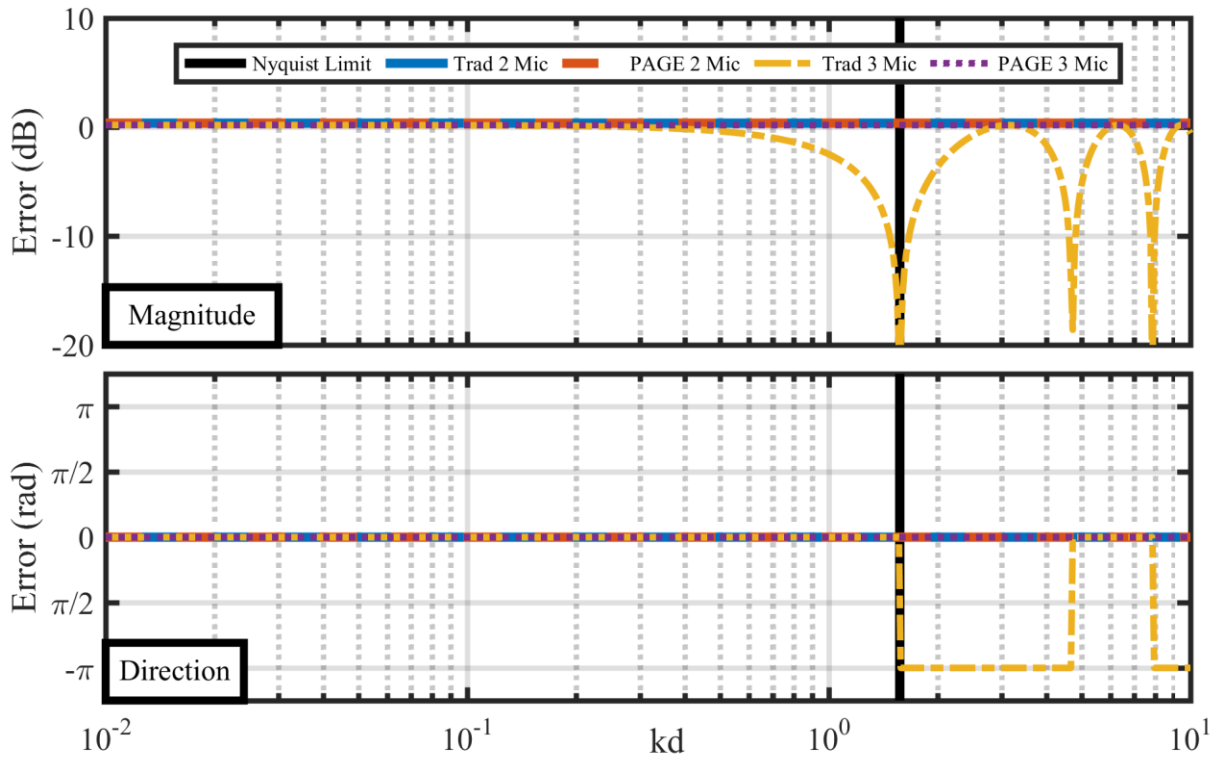


Figure 3.14. The reactive intensity relative error for $r = 2d$, $d = 2$ cm, and d is the distance between the center and an outer microphone. Bias error is present in all of the processing and probes depicted. The traditional method applied to three-microphone probe is frequency dependent in its error, as are both of the PAGE method estimates.

The variation in the error of the reactive intensity estimates as a function of kd and kr are shown in Figure 3.15 and exhibit similar behavior to the active intensity estimates in Figure 3.13. The two-microphone method has the same relative error results regardless of the processing method, and there is a large bias error when r approaches d . Likewise, the three-microphone probes also have a similar bias error that is less than the two-microphone probes, but the

traditional processing method has additional oscillations in the error starting near the spatial Nyquist frequency.

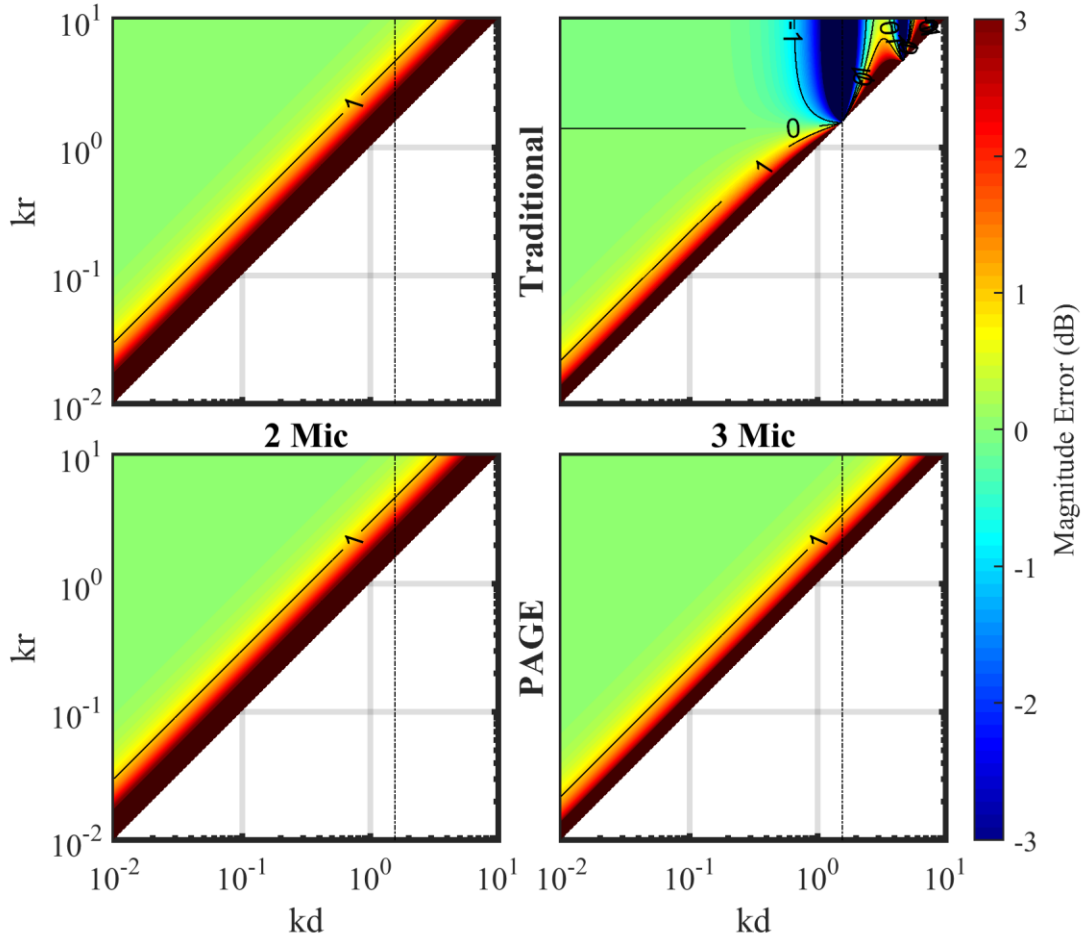


Figure 3.15. Relative error for reactive intensity as a function of kd and kr . The black line indicates the spatial Nyquist limit. Bias errors are present in all processing and probes. The PAGE three-microphone results have slightly less relative error than the two-microphone results. The traditional and PAGE methods are the same for the two-microphone case.

3.4.2.4 Potential and kinetic energy density relative error

The potential and kinetic energy density expressions can be quite complicated, but ultimately the relative error expressions are simply the squared magnitude of the pressure and particle velocity relative error expressions. Thus, they have similar trends as the relative error for pressure and particle velocity as shown in Table 3.13. One truly unique trait is that the PAGE method applied to a three-microphone probe approaches 0 dB relative error for kinetic energy

density at higher frequencies. The change is subtle, but visible in Figure 3.16. Again, the PAGE method dramatically increases the bandwidth. For potential energy density, the PAGE method can go to the SNF, while the traditional method cuts off at $0.48kd$. For kinetic energy density, the PAGE method does not fall off, but the traditional method falls off at $0.76 kd$.

Table 3.13. Relative error for potential and kinetic energy using the traditional and PAGE method with a two and three-microphone probe for the monopole case.

	Traditional		PAGE	
	2 Mic	3 Mic	2 Mic	3 Mic
e_{E_p}	$\beta^2 \left[\cos^2(kd) + \left(\frac{kd}{kr}\right)^2 \sin^2(kd) \right] - 1$	0	$\beta^2 - 1$	0
e_{E_k}	$\frac{\beta^2 [\cos^2(kd) + \left(\frac{kr}{kd}\right)^2 \sin^2(kd)]}{1 + (kr)^2} - 1$		$\beta^2 - 1$	$\frac{\beta^2 \left\{ [kd]^2 \left[\left(\frac{kd}{kr}\right)^2 - 2 \right] + [1 + (kr)^2] \right\}}{1 + (kr)^2} - 1$

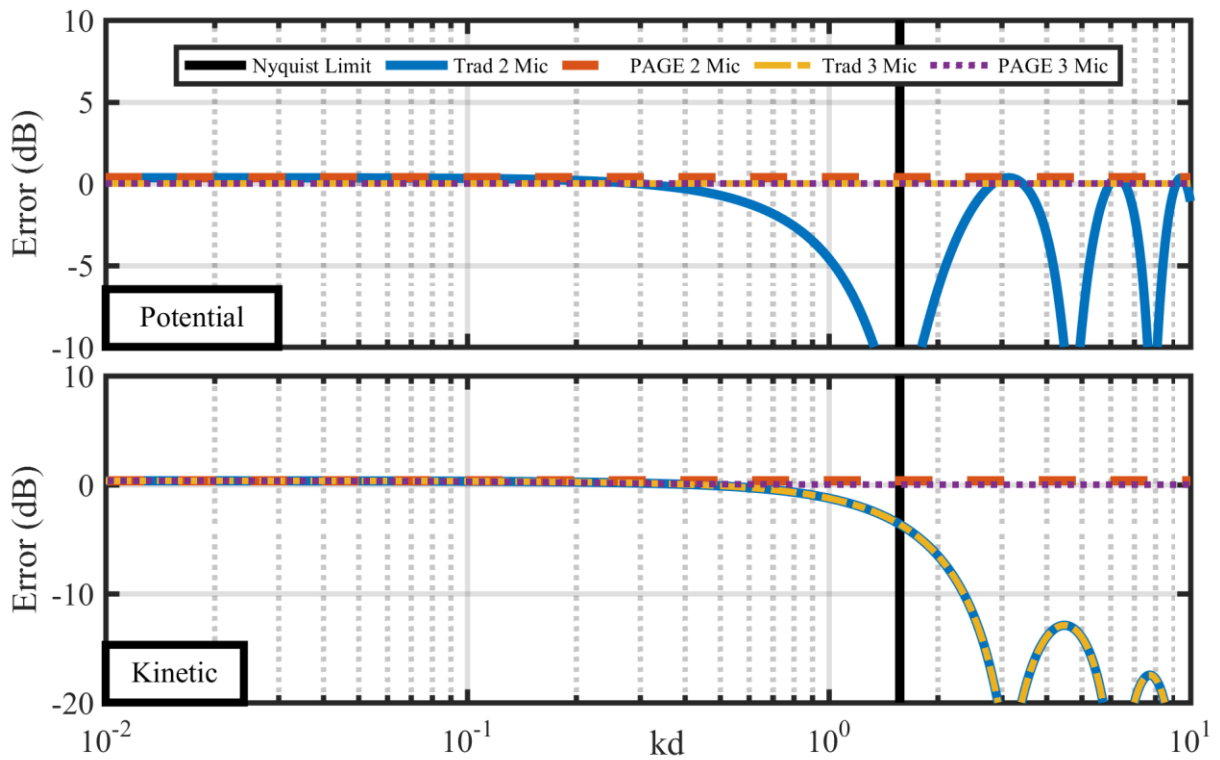


Figure 3.16. The energy density relative error when $r = 4.3d$. The top plot is the potential energy, and the bottom plot is the kinetic energy. The traditional method has error that oscillates above the Nyquist limit. The PAGE method shows constant bias errors. The bias error goes to 0 dB above the Nyquist limit for the three-microphone case.

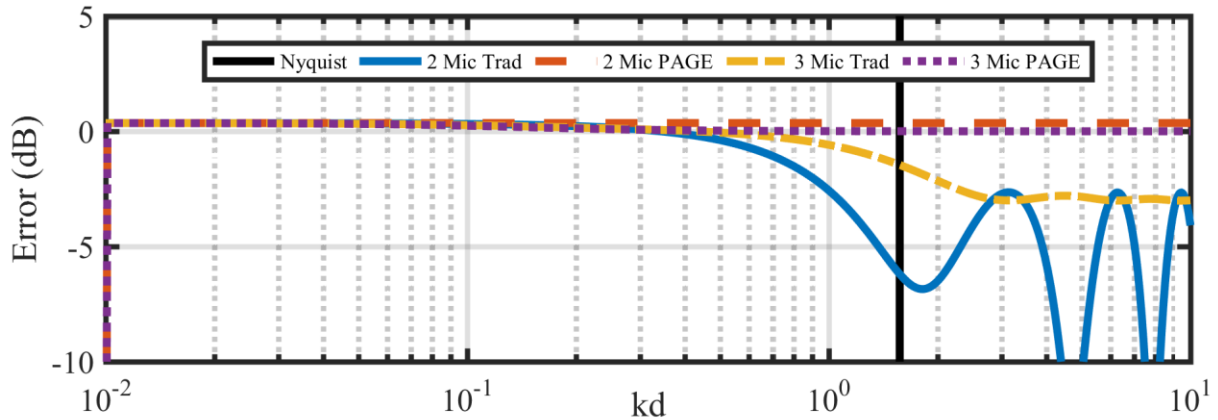


Figure 3.17. The relative total energy density error with the probe at $r = 4.3d$.

Since the distance from the source has to be greater than 4.3 times the probe radius, the monopole field is very similar to the plane wave results. The energy density plot in Figure 3.17 looks very similar to Figure 3.6. The microphone in the center of the probe dramatically improved the traditional method's estimate and the PAGE method estimate has a constant bias, independent of frequency.

Figure 3.18 shows the effect that distance from the source and the probe microphone spacing have on the estimate of potential energy density. The three-microphone probe measures the pressure exactly so there is no relative error in potential energy density estimates with this probe (recall that potential energy density depends only on the squared magnitude of pressure). As has been seen repeatedly, the two-microphone probe features a large bias error when the distance from the source approaches the radius of the probe. Furthermore, the traditional method has a frequency dependence that limits the usable frequency bandwidth of this method.

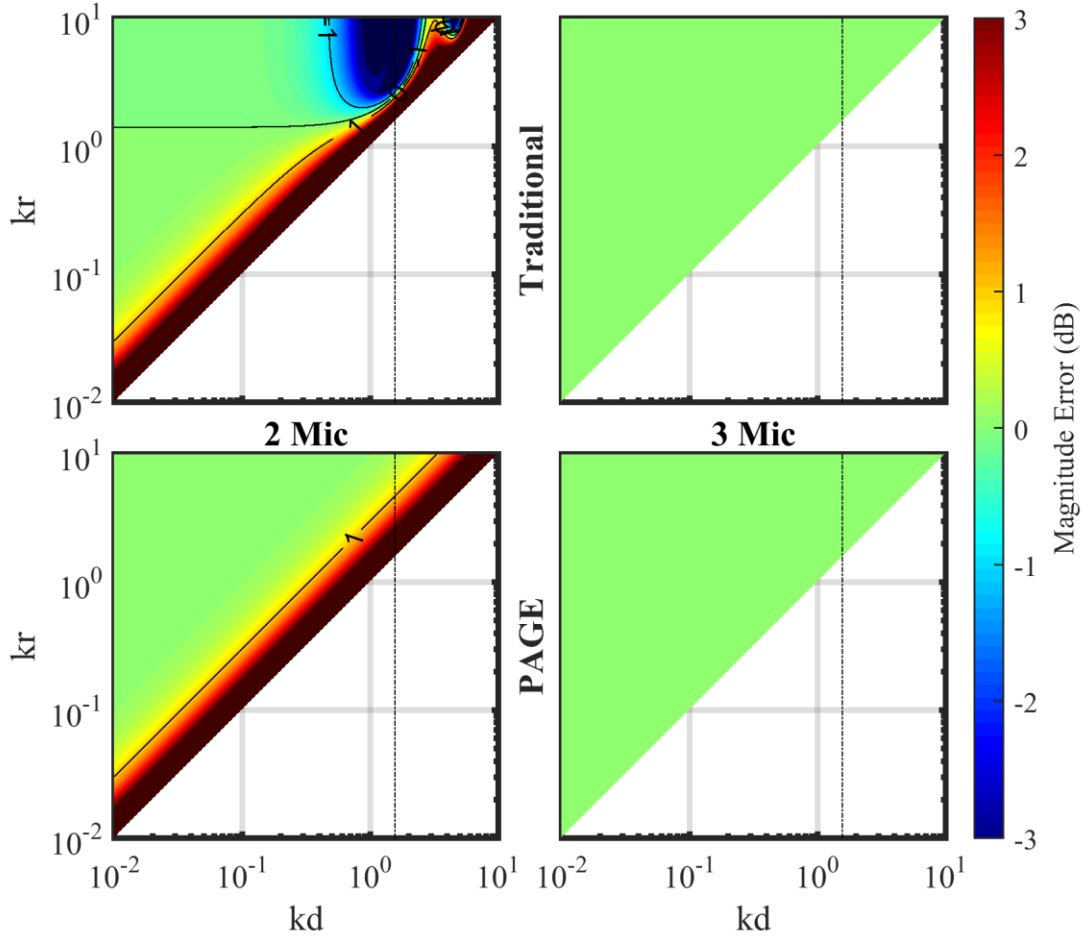


Figure 3.18. Relative error for potential energy density as a function of kd and kr . The black line indicates the spatial Nyquist limit.

The relative error for kinetic energy density shows trends similar to the particle velocity estimates, as shown in Figure 3.19. The bias error for probe spacing and distance from source is again present, and the traditional method is limited to lower frequencies. The PAGE method has a bias error for both probe configurations, but the three-microphone approach actually improves near the spatial Nyquist frequency. This reduction in error comes because kinetic energy density is proportional to the center pressure times the gradient of phase plus the gradient of particle velocity. The three-microphone probe center pressure measurement is significantly better than the two-microphone pressure estimate at higher frequencies, and the PAGE method's ability to

better estimate the gradient of particle velocity makes it perform better than the traditional method at higher frequencies.

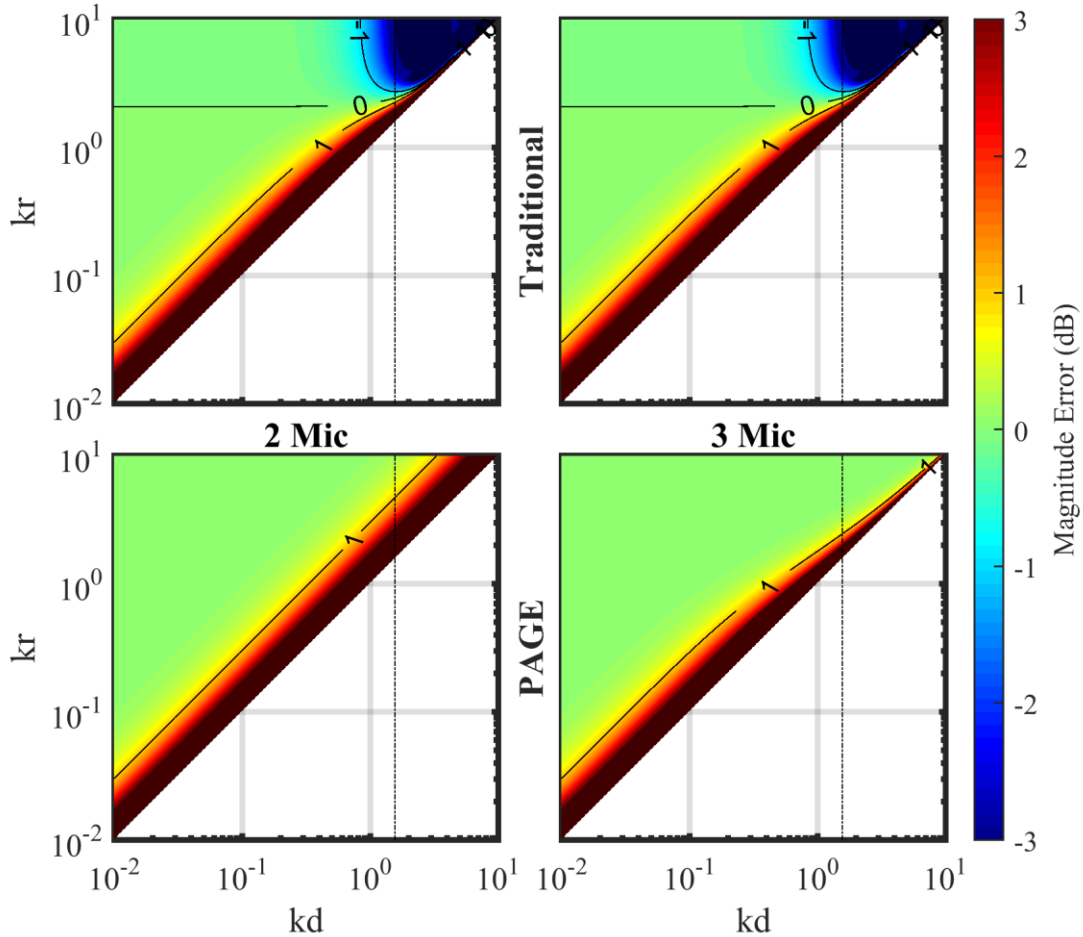


Figure 3.19. Relative error for kinetic energy density as a function of kd and kr . The black line indicates the spatial Nyquist limit. The PAGE method estimate with the three-microphone probe has less error at higher frequencies, but the two-microphone probe has a constant bias error. The traditional method's analysis is again frequency dependent and worsens near the Nyquist limit.

3.4.2.5 Specific acoustic impedance relative error

The monopole field specific acoustic impedance error expressions are quite complicated for the traditional method and simpler for the PAGE method. The traditional method had complex expressions for pressure and particle velocity, therefore it is not surprising that it also has complex relative error expressions for specific acoustic impedance. For the traditional method, the particle velocity falls off as frequency increases, therefore at high frequencies the

traditional method has huge errors. On the other hand, the PAGE method performs better at high frequencies. In fact, for the two-microphone probe, the error in the pressure is the same as the bias error for particle velocity, so when the two are combined, the errors cancel out and the PAGE method's estimate of specific acoustic impedance has no error. The three-microphone probe has some error, but it is mostly incorrect in the region where $kr \approx kd$. The traditional method bandwidth was able to reach $0.63kd$ for the two-microphone probe and $0.95kd$ for the three-microphone probe. For the PAGE method, the bandwidth of accurate results reaches the SNF.

Table 3.14. Relative error for the specific acoustic impedance using the traditional and PAGE method with a two- and three-microphone probe for the monopole case.

	Traditional		PAGE	
	2 Mic	3 Mic	2 Mic	3 Mic
e_z	$\frac{kd(1 + jkr)[kr \cos(kd) + jkd \sin(kd)]}{kr[kd \cos(kd) + jkr \sin(kd)]} - 1$	$\frac{kd(1 + jkr)}{\beta[kd \cos(kd) + jkr \sin(kd)]} - 1$	0	$\frac{kr - j}{kr - j\beta} - 1$

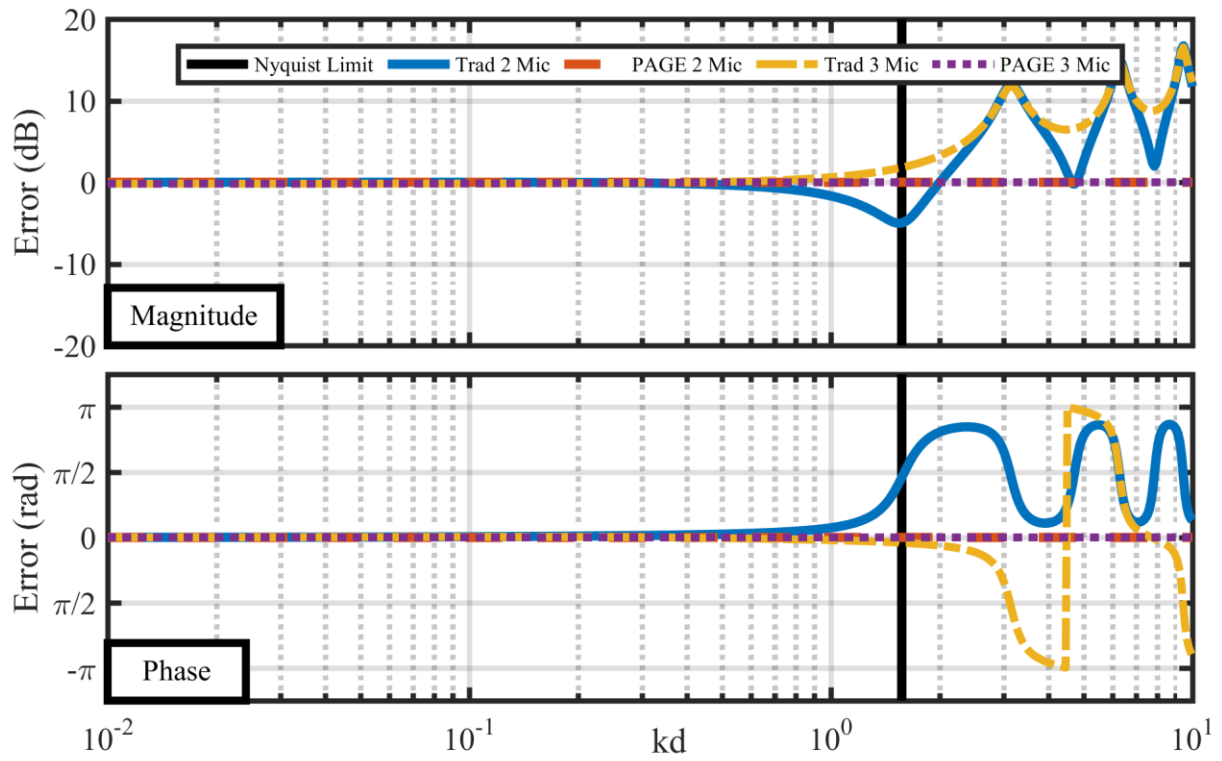


Figure 3.20. The relative error for specific acoustic impedance of a monopole where the probe is at $r = 4.3d$.

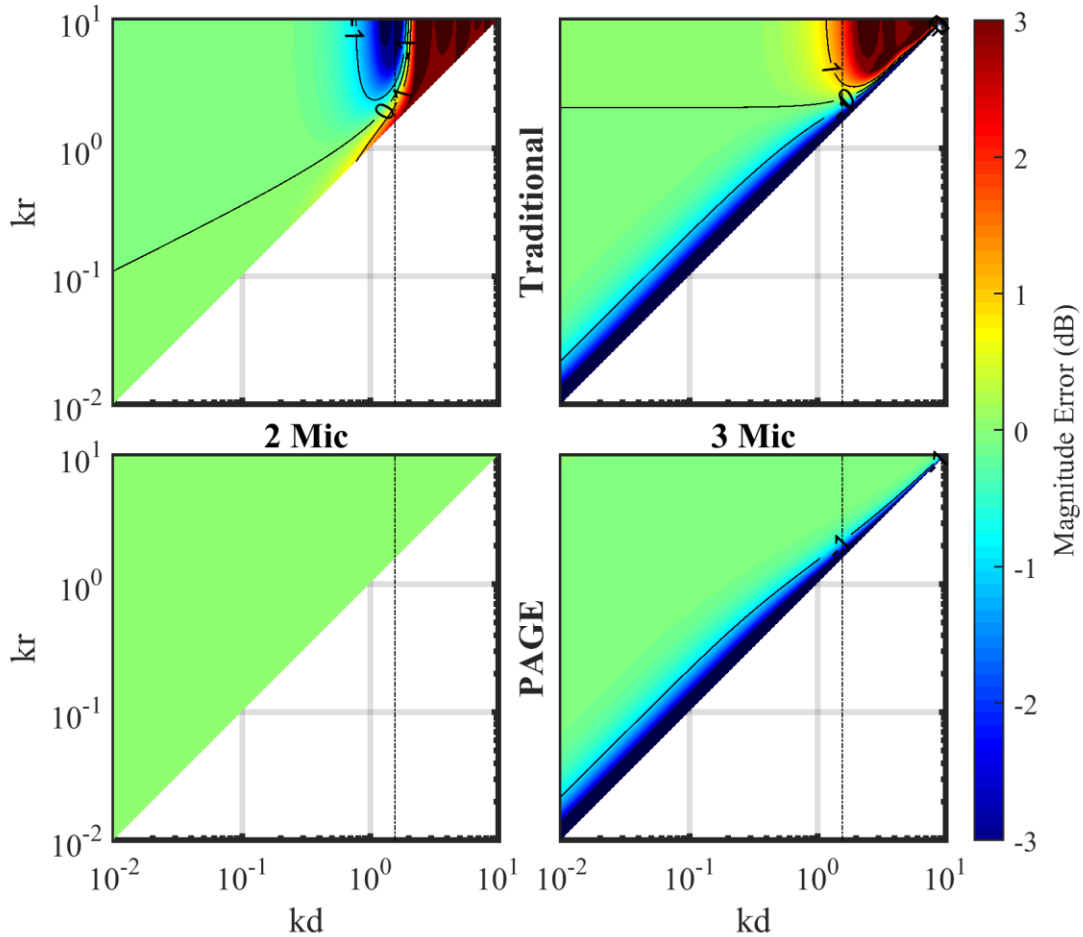


Figure 3.21. Relative error for the magnitude of specific acoustic impedance. The traditional method has large errors at high frequencies because that's where its estimates of pressure and particle velocity break down. The PAGE method's estimate with the two-microphone probe results in zero error. The three-microphone probe has a constant bias error due to microphone spacing and distance to source, but this bias decreases at the higher frequencies.

3.5 Conclusions

The error of the traditional and PAGE methods for estimating acoustic quantities in various fields has been shown. For a propagating plane wave, the traditional method breaks down as kd approaches the spatial Nyquist frequency limit, where d is the distance from the center of the probe to the outer microphones. On the other hand, the PAGE method has no errors in magnitude or phase estimation for the plane wave case up to the spatial Nyquist limit without phase unwrapping and above it with phase. For a standing wave, the PAGE method does not

perform better than the traditional method. The pressure values in this reactive field are real, so even though the PAGE method uses a difference of pressure magnitudes from the probe, it is the same as the traditional method's attempt at estimating the gradient using the real part of the pressure. Furthermore, since a standing wave can be considered the sum of two traveling plane waves, the relative errors are basically the same as the plane wave case. However, the PAGE method does not handle a probe measurement across a node in the field as well as the traditional method does. For the monopole, the traditional method breaks down with large kd , but both methods have a bias error in the estimate of all the energy quantities that depends on the size of the probe and the proximity to the source. As a general rule for both processing methods, the probe needs to be several radii away from the source. For the bias error to be less than 0.5 dB, the probe needs to be $4.3d$ away from the source. This can be problematic for measurements of the near-field properties of a source.

From a bias error standpoint, the PAGE method is clearly the optimal method for processing broadband data in propagating fields. For every energy quantity in the propagating fields, the PAGE method performed as well as or better than the traditional method and it did not have the same frequency dependence except for the three-microphone probe estimate of the particle velocity. In fact, without a frequency dependence, it is theoretically possible to make a correction to a measurement based on the probe radius and the distance from the source, assuming the source behaves like a monopole.

This work compared the two analysis methods for simple fields and ideal probes. It is still unclear which method performs better in non-ideal cases, such as when required to handle extraneous noise in the field. It is here inferred that the results for non-ideal cases would show

similar patterns. Since it is a general trend for the traditional method to be frequency limited, it is not included in the following work that analyzes ideal situations.

Interestingly, the results from the three-microphone probe were not always better than those of the two-microphone probe. The two-microphone probe was better at estimating specific acoustic impedance of a monopole because the error in the pressure estimate was the same as the error in the particle velocity. Therefore, the relative errors cancelled out allowing the two-microphone probe to exactly estimate the specific acoustic impedance. Likewise, in the plane wave case, both types of probes had zero specific acoustic impedance error when using the PAGE processing method. Now, this may only work in the ideal plane wave or monopole fields, but this peculiarity could be studied further. In another instance, the three-microphone probe's estimates of particle velocity and pressure were frequency dependent, while the two-microphone probe's estimates were not. Despite this advantage, the two-microphone probe did not necessarily perform better than the three-microphone probe in terms of having a lower bias error when $d \approx r$, or when the probe was near the source.

Although it is theoretically possible to derive error expressions for other fields and probe configurations, the work is tedious and only somewhat useful. The expressions derived and analyzed here form a good basis from which the expressions for additional fields and probe configurations can be extended. Even for the monopole case, the relative error expressions for some energy quantities were quite complicated and not necessarily insightful. In a multidimensional field, the incident angle could change with each measurement position, which would mean that a transformation of the error expression would be required for each incident angle. Therefore, an approach that can quickly and easily simulate the results measurements

made with various probe configurations in a variety of fields of complex sources is desired. This is discussed in Chapter 4.

Chapter 4

Two dimensional probe errors simulations

4.1 Introduction

Derivations of analytical expressions for calculating the various energy quantities is useful but really only practical for simple systems and simple probe configurations. For two- or three-dimensional fields and two- or three- dimensional probes, the derivations become complex and unwieldy. Therefore, a general approach to model both various practical fields as well as the errors from different probe designs is necessary.

4.2 Simulating two dimensional fields

All the energy quantities of interest can be derived from the pressure and particle velocity at a point in space. In order to calculate the pressure, the Rayleigh integral equation⁶⁰ can be used if one assumes that the source is surrounded by an infinite baffle. The Rayleigh integral can be written as

$$\tilde{p}(\omega, \vec{r}) = \frac{jk\rho_0c}{2\pi} \int \frac{\tilde{u}_0(\omega, \vec{r}_0)e^{-jkr}}{r} dS, \quad \begin{array}{l} \text{Eq.} \\ 4.1 \end{array}$$

where $\tilde{p}(\omega, \vec{r})$ is the complex pressure at angular frequency ω and position \vec{r} , k is the wavenumber, ρ_0 is the density of air, c is the speed of sound in air, $\tilde{u}_0(\omega, \vec{r}_0)$ is the surface velocity of the source at position \vec{r}_0 on the surface, r is the distance from \vec{r}_0 to \vec{r} , and dS is the differential area to be integrated over the surface.

In order to calculate the particle velocity, the linear form of Euler's equation is used to relate the particle velocity to the gradient of pressure

$$\vec{\tilde{u}}(\omega, \vec{r}) = \frac{j}{\rho_0 \omega} \nabla \tilde{p}(\omega, \vec{r}), \quad \text{Eq. 4.2}$$

where $\vec{\tilde{u}}(\omega, \vec{r})$ is the particle velocity at position \vec{r} , and $\tilde{p}(\omega, \vec{r})$ is the pressure calculated from Eq. 4.1. An expression for the particle velocity can be obtained for a baffled source by taking the gradient of the Rayleigh integral for the pressure

$$\vec{\tilde{u}}(\omega, \vec{r}) = \frac{1}{2\pi} \int \tilde{u}_0(\omega, \vec{r}_0) \frac{e^{-jkr}(1 + jkr)}{r^2} \hat{r} dS, \quad \text{Eq. 4.3}$$

where \hat{r} is the unit vector pointing from \vec{r}_0 to \vec{r} .

Because of the difficulty of finding the analytical expression from these integrals, the whole process is avoided by changing the integral equations into discrete sums over points defined on the source surface such that a numerical approximation of the integral can be obtained. In practice, a scanning laser Doppler vibrometer could be used to find the surface velocity of a source that can be used in the Rayleigh integral to obtain the field quantities, which can be used to estimate the various energy quantities. This could be done for complicated surface velocities beyond simple baffled pistons, which is the source modeled in this work.

4.3 Simulating results of different probe configurations

Once the estimates of the pressure and particle velocities of the acoustic field are obtained, the theoretical complex intensities, energy densities, and specific acoustic impedances can be computed. Then, it becomes desirable to compare the results from different probe configurations, rotations, and calculation methodologies to these theoretical results with the assumption that the theoretical results have zero error. To make this comparison, the Rayleigh integral equation can be used to calculate the complex pressure at each of the microphone

locations of the probe. The resulting pressures can be processed using both the traditional and PAGE methods to see how well estimates of the energy-based quantities match the theoretical results for the specified probe configuration. This allows a quick and convenient way to analyze various probe configurations as well as visualize the relative error from different methods.

Even with limiting this work to investigating only probe designs with a symmetric arrangement with few microphones, there are still many different ways of arranging and orienting the microphones. Furthermore, there are additional considerations like the orientation of the microphones and the microphone locations relative to the microphone holder in three dimensions, like enclosing the microphones on the surface of a hard sphere.^{45, 46} Since the goal is to develop intuition into the advantages and the possible bias errors of various probe designs, only those arrangements that are distinctly different are examined instead of investigating an exhaustive list of probe arrangements. The selected probe designs are an equilateral triangle with a microphone at the center, two orthogonal pairs of microphones, and two orthogonal pairs with an additional microphone at the center of the probe.

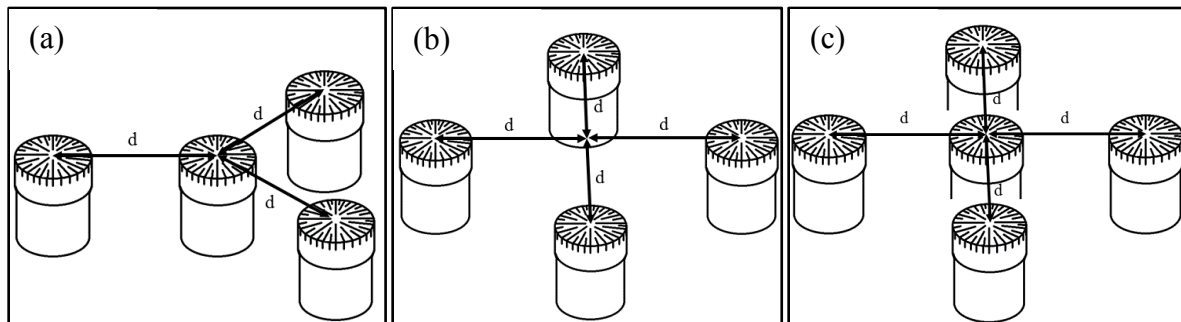


Figure 4.1. The three probe configurations: (a) equilateral triangle with a microphone at the center, (b) the orthogonal pair of microphones with no microphone at the center, and (c) the orthogonal pair of microphones with a microphone at the center.

Probe rotation is an important consideration for the accuracy of a measurement. Many probes are more accurate when the wave is propagating along a specific axis of the probe. Thus, if the probe is not pointed at the source, then the probe is effectively rotated relative to the wave

front. Thus, there will be errors associated with the angle of incidence on the probe and not just the probe design.

To analyze the merits of each probe design, the error of various energy quantities is examined in the field of a baffled circular piston (BCP). The BCP has the advantages of a reactive near field and a plane-wave-like far field. In this way, although it is a simplification of a real source, it is the best simplification of what the field of a real source in an anechoic environment would be.

4.4 Baffled circular piston results

For propagating waves, active intensity is the quantity that most readily identifies the key features of the acoustic field. An accurate measure of the active intensity can help characterize the source. For example, if the active intensity vectors at different probe locations are ray-traced back to the source, an estimate of the location of the maximum equivalent source region can be obtained (see Figure 1.2).¹⁴ Also, the power of the source can be obtained by integrating the active intensity vectors over a surface.² Hence, the dependence of errors in the active intensity due to probe geometry are considered first.

In Figure 4.1, subplot (a) shows the active intensity field from the modeled BCP with a radius of 3.5 cm centered at the origin with a frequency of 8 kHz calculated using discrete versions of Eq. 4.1 and Eq. 4.3. Subplots (b), (c), and (d) display the magnitude of the error of the active intensity estimates obtained by the PAGE method relative to the BCP model for three probes. All three probes have $d = 5$ cm as the distance from the center of the probe to the outer microphones. At this size of probe, the results rely on correct phase unwrapping since 8 kHz is over the spatial Nyquist limit. The equilateral triangle configuration shown in subplot (b) is the four microphone probe configuration developed for rocket noise research at BYU.⁵³ A

commonly used four-microphone orthogonal probe shown in subplot (c) is a commonly used intensity probe configuration, and for comparison, an orthogonal probe with a microphone at the center shown in subplot (d) is also selected to highlight the benefits of having an additional microphone at the center of the probe. Subplots (c) and (d) were chosen because they are similar to the one dimensional two- and three-microphone probes discussed in previous chapters. The closest r shown in Figure 4.1 and subsequent plots is $2d$.

For active intensity, there is an advantage to having a microphone at the center of the intensity probe. Clearly, the five microphone orthogonal probe (subplot (d)) yields an active intensity estimate with very little error. Likewise, the equilateral triangle with a microphone in the center (subplot (b)) provides a good estimate; it has less than 1 dB of bias error overall and performs the worst where there is a null in the field. All probes seem to have trouble accurately measuring the active intensity near nulls, especially because these probes have a large radius of 5 cm. The probes do not accurately measure intensity across the null because the phase changes on different sides of the null. This makes the estimate of phase very inaccurate near the null. Furthermore, when there is no center microphone, the center pressure is estimated by averaging the pressure magnitudes from the outer microphones. When near a null, this estimate is not close to zero as one would expect. This is why subplot (c) has a large error near the null. There is also a difference between subplot (b) and subplot (d). Although both have close to 0 dB error far from the nulls, subplot (b) shows errors both higher and lower than 0 dB, and subplot (d) only has error lower than 0 dB. From these plots, it is unclear which probe is better, but it is apparent that the probe configuration does affect the result. Lastly, subplot (c) clearly shows the disadvantage from the lack of a center microphone when compared to subplot (d). These results agree with the one dimensional cases where the center microphone improved the active intensity estimates.

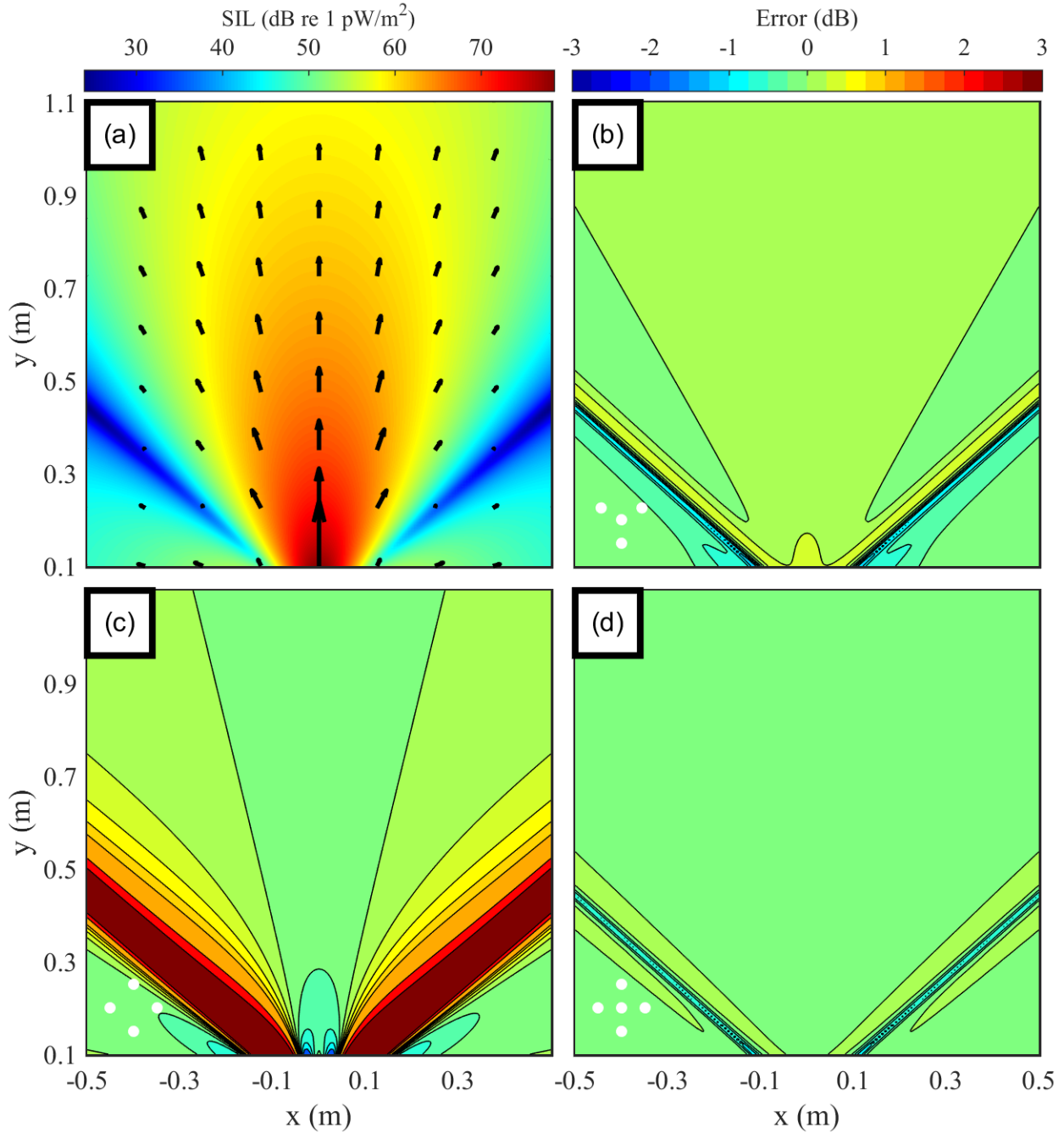


Figure 4.2. Magnitude error for active intensity between the analytical solution of the baffled circular piston and various estimates at 8 kHz from different probes using the PAGE method. Subplot (a) shows the active sound intensity level and some active intensity vectors. The remaining subplots show the error, on a decibel scale, in magnitude of the active intensity estimates obtained for (b) the equilateral triangle probe with a microphone at the center, (c) the orthogonal probe with no microphone at the center, and (d) the orthogonal probe with a microphone at the center. The size of the probe and microphone positions are shown in the bottom left corner of each error subplot.

Reactive intensity is difficult to accurately estimate. Every relative error subplot in Figure 4.3, has more error than is seen with the other energy quantities. The orthogonal pair probes (subplot (c) and (d)) perform better than the equilateral triangle probe (subplot(b)). In fact, subplot (b) indicates that the equilateral probe error varies from around -2 dB to 1 dB depending on the orientation of the probe. The orthogonal probes have small error away from the nulls and the source, but these are the regions where reactive intensity is strongest. Interestingly, subplot (c) seems to perform better in certain directions (slightly off axis the middle of the plot) than subplot (d), but there are large positive errors near the null. The estimate of the center pressure magnitude is too high. This combined with the underestimation of the gradient of pressure in this region explains why subplot (c) has smaller error near the middle, but retains large errors near the null. The presence of a center microphone, as in the one-dimensional case, tends to minimize the error, with the exception just discussed, where overestimation of center pressure combined with underestimation of pressure gradient has less error than the case with an exact center pressure measurement.

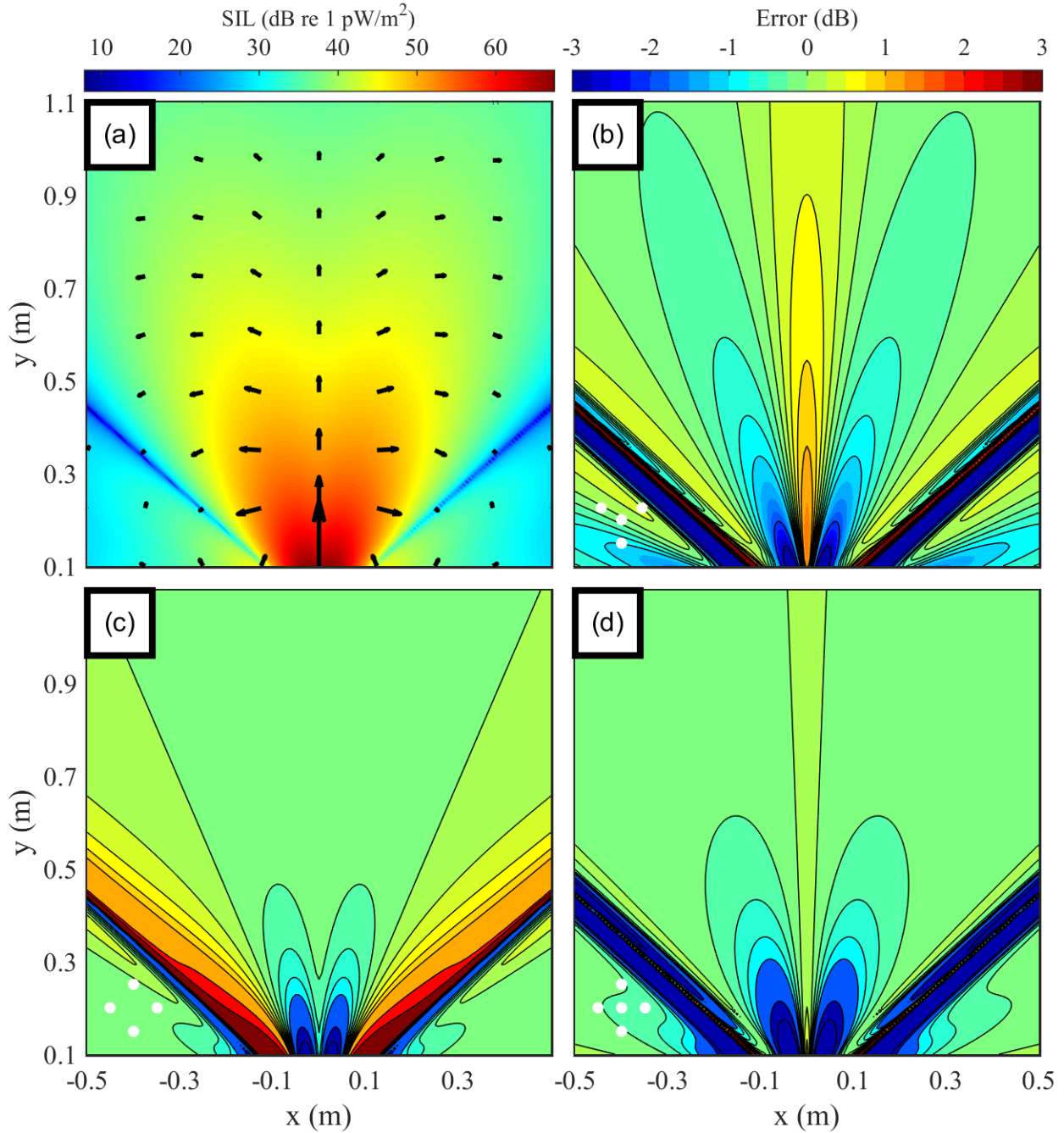


Figure 4.3. Magnitude error for reactive intensity between the analytical solution and various estimates at 8 kHz from different probes using the PAGE method. Subplot (a) shows the reactive sound intensity level and some reactive intensity vectors from the baffled circular piston model. The remaining subplots show the error, on a decibel scale, in magnitude of the reactive intensity estimates obtained for (b) the equilateral triangle probe with a microphone at the center, (c) the orthogonal probe with no microphone at the center, and (d) the orthogonal probe with a microphone at the center. The size of the probe and microphone positions are shown in the bottom left corner of each error subplot.

Likewise, the potential and kinetic energy density comparison show the advantage of an orthogonal probe with a center microphone. Since potential energy is based on the pressure magnitude squared, any probe configuration with a microphone at the center obtains a perfect result. Configurations lacking the center microphone have errors based on their ability to estimate the center pressure, as shown in Figure 4.4. This agrees with the one dimensional case where a center probe eliminated the error in estimating the potential energy. Finally, Figure 4.5 shows the probe bias errors in the kinetic energy density. Since kinetic energy depends on both the gradient of phase and the gradient of pressure magnitude as well as the estimate of the center pressure, the ability to estimate these quantities determines the quality of the bias error. Thus, the probes with a center microphone (both subplots (b) and (d)) perform better than the orthogonal probe without one (subplot (c)). Furthermore, since the orthogonal probe configuration (subplot (d)) is better at estimating the pressure gradient than the equilateral triangle probe (subplot (b)), it has significantly less error. Also, it should be pointed out that unlike the one dimensional probes, the two dimensional probes have different angle of incident upon the probe. This means in certain directions each probe will perform better or worse. The equilateral triangle probe performs worse in the y direction, because it has to estimate the gradients using a combination of microphone pairs while the orthogonal probe only has to use the outer microphones aligned in the y direction.

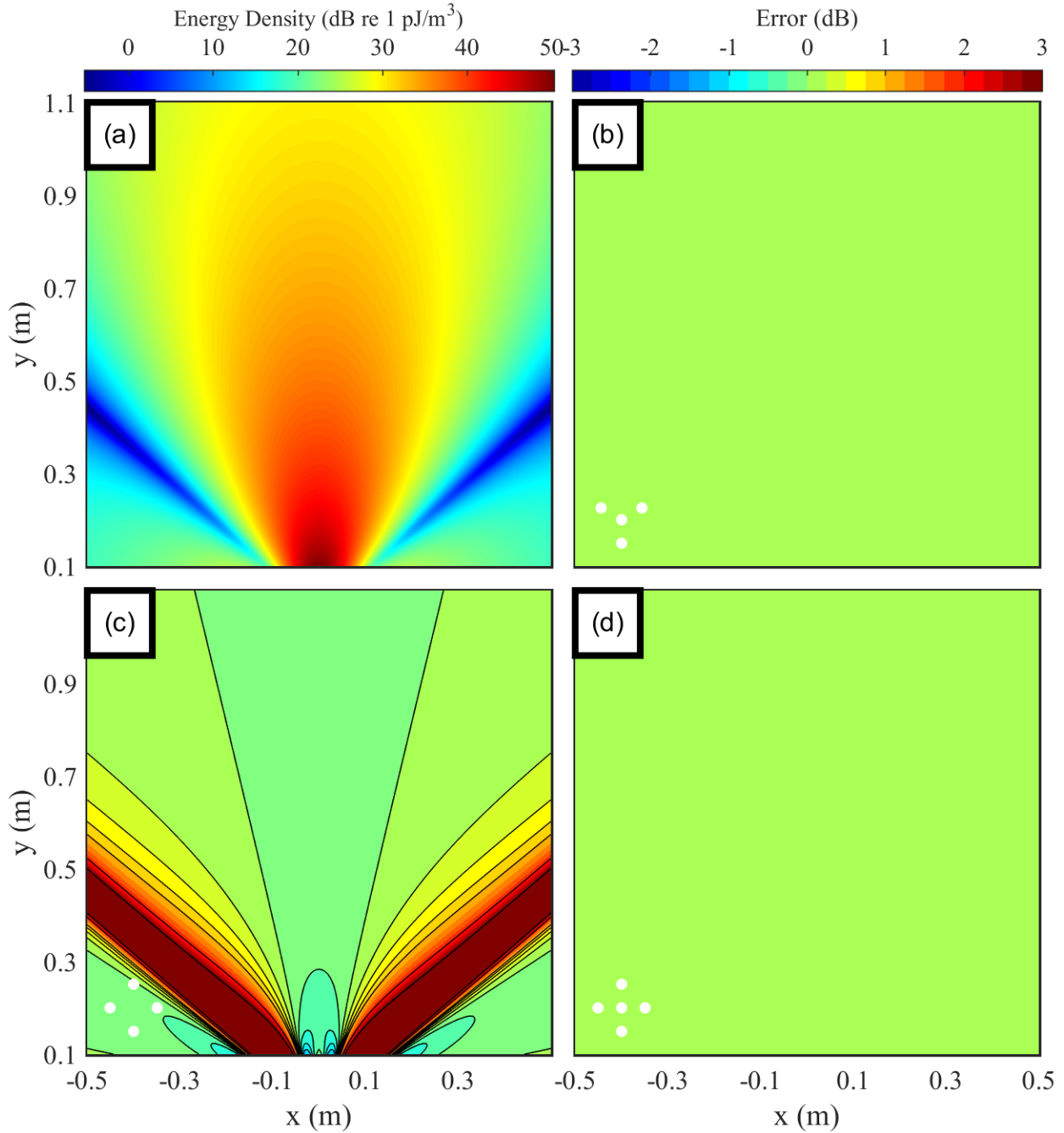


Figure 4.4. Magnitude error for potential energy density between the analytical solution and various estimates at 8 kHz from different probes using the PAGE method. Subplot (a) shows the potential energy density level from a baffled circular piston. The remaining subplots show the error, on a decibel scale, in magnitude of the potential energy estimates obtained for (b) the equilateral triangle probe with a microphone at the center, (c) the orthogonal probe with no microphone at the center, and (d) the orthogonal probe with a microphone at the center. The size of the probe and microphone positions are shown in the bottom left corner of each error subplot.

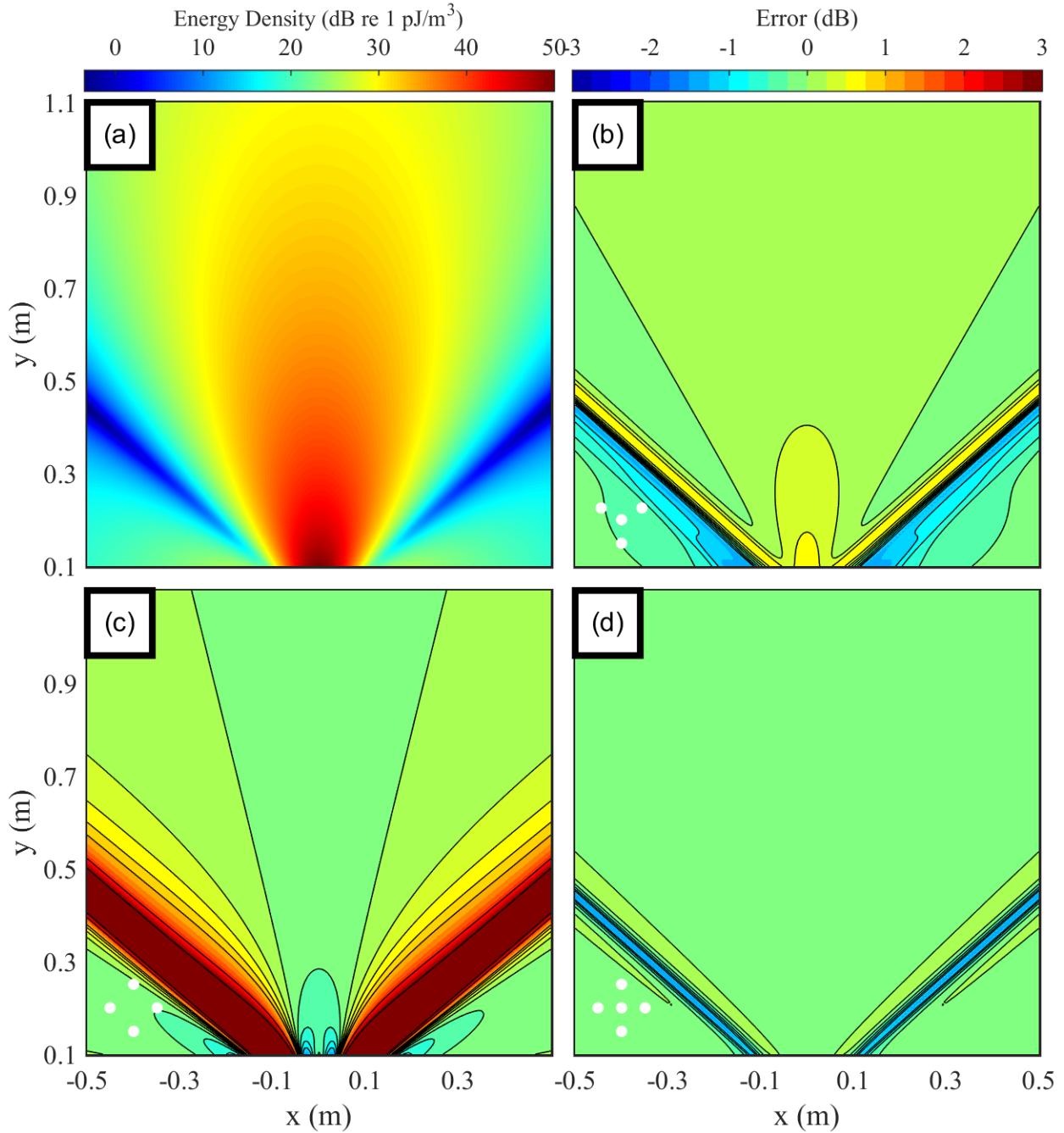


Figure 4.5. Magnitude error for kinetic energy density between the analytical solution and various estimates at 8 kHz from different probes using the PAGE method. Subplot (a) shows the kinetic energy density level for the baffled circular piston. The remaining subplots show the error, on a decibel scale, in magnitude of the kinetic energy estimates obtained for (b) the equilateral triangle probe with a microphone at the center, (c) the orthogonal probe with no microphone at the center, and (d) the orthogonal probe with a microphone at the center. The size of the probe and microphone positions are shown in the bottom left corner of each error subplot.

Lastly, these probes do surprisingly well at measuring the specific acoustic impedance.

Normally, when computed using the traditional method, the specific acoustic impedance can

only be found in a narrow frequency range. But using the PAGE method, as shown in Figure 4.6, the specific acoustic impedance is shown to have very little relative error at 8 kHz. At 8 kHz, the acoustic wavelengths are small compared to the distance from the source, making this analysis largely in the far field. In the far-field, the estimated impedance magnitude approaches the specific acoustic impedance of a plane wave, as expected. In Section 3.2.2.5, the one-dimensional analysis of a plane wave showed that the PAGE method did very well at estimating the specific acoustic impedance. Here, the two-dimensional analysis similarly shows that the specific acoustic impedance is well estimated in the plane-wave-like far field.

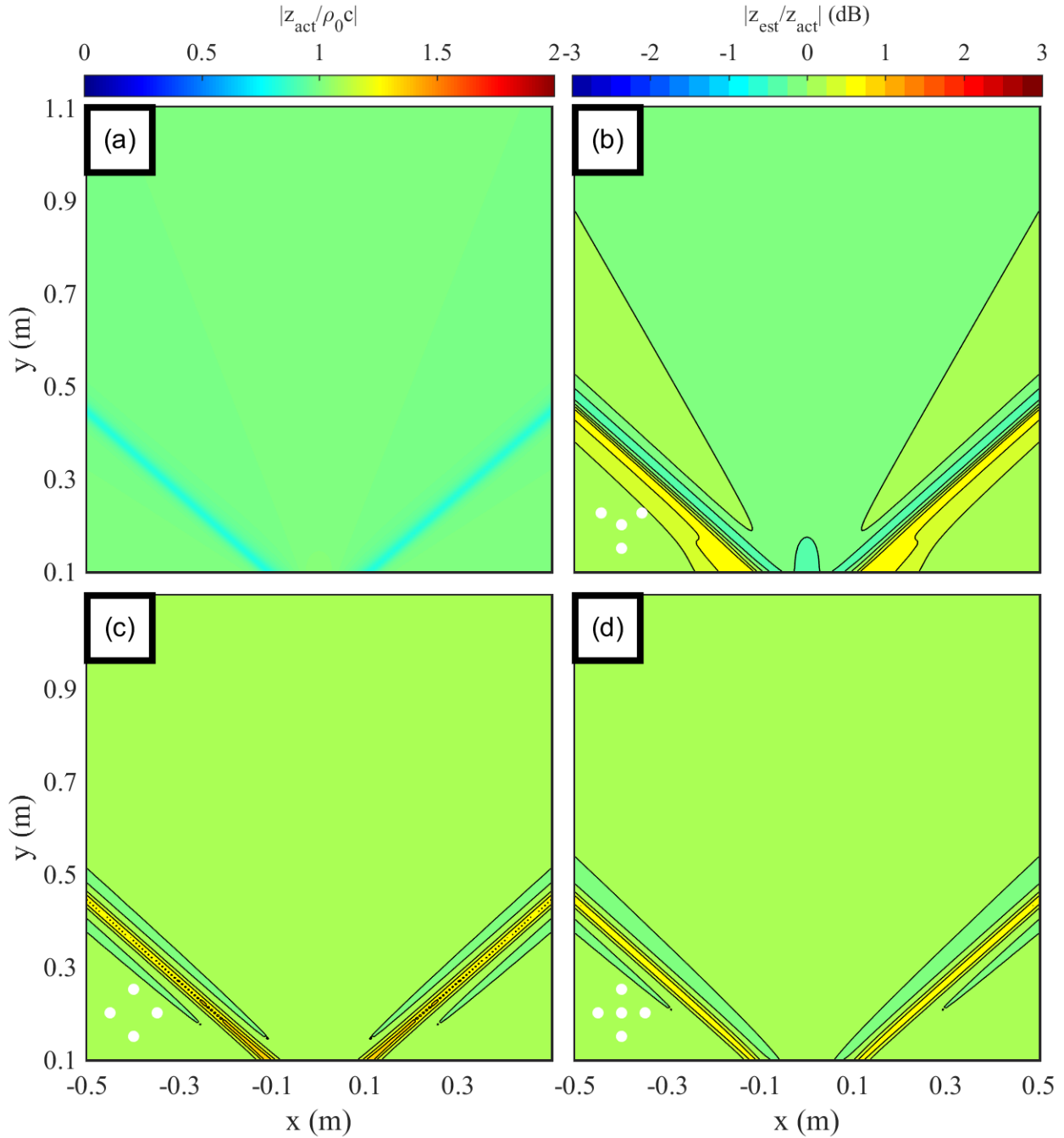


Figure 4.6. Error plot showing the magnitude error for specific acoustic impedance between the analytical solution and various estimates in the direction of the active intensity at 8 kHz from different probes using the PAGE method. Subplot (a) shows the specific acoustic impedance for a baffled circular piston divided by the specific acoustic impedance of a plane wave, for the baffled circular piston. The remaining subplots show the error, on a decibel scale, in magnitude of the specific acoustic impedance estimates obtained for (b) the equilateral triangle probe with a microphone at the center, (c) the orthogonal probe with no microphone at the center, and (d) the orthogonal probe with a microphone at the center. The size of the probe and microphone positions are shown in the bottom left corner of each error subplot

4.5 Conclusions

The numerical study presented in this chapter is a significant contribution because it demonstrates how to analyze the bias error of the estimates of various energy quantities based on probe configuration over a broader range of frequencies than previously possible. The probe size makes a significant impact on how well the quantities are estimated. A large probe radius has its advantages and disadvantages. On the one hand, it allows for analysis of lower frequencies because the measurement is not as susceptible to differences in microphone response times to a signal. It has the disadvantage that the larger probe yields a worse estimate of the gradient. The method of analysis also impacts the results. Although not shown in this chapter, the traditional method cannot obtain reasonable estimates of active intensity at 8 kHz from a probe with $d = 5$ cm. The only reason the PAGE method could obtain good estimates at this high frequency is because of its ability to unwrap the phase and thus properly estimates the gradients of the pressure and particle velocity beyond the spatial Nyquist limit. Using this technique of analyzing bias error, various probe configurations can be analyzed and compared to find the optimal configuration based on bias error. In practice, the complex pressure at the probe microphone locations can be modeled using the Rayleigh integral based on a measured source velocity distribution. Then, the bias errors from the processing method for each acoustic energy quantity of interest and for the particular probe of interest can be estimated.

This work demonstrates that the optimal probe configuration for estimating all acoustic quantities of interest for propagating wave fields is two orthogonal pairs of microphones with a microphone at the center. This probe configuration has the least bias error for all energy quantities. At the very least, there is a significant advantage in having a microphone at the center of the probe when estimating quantities like active intensity level and potential energy that

depend on the center pressure directly. Because the orthogonal probe with microphone at the center requires 5 microphones, it might be advantageous in some cases to use the equilateral triangle probe because the error from this probe design was still minimal and mainly struggled around interference nulls. Furthermore, the five microphone orthogonal probe is physically larger than a probe with fewer microphones because the size and spacing of the microphones limits how small the probe can be made. Additionally, a probe with more microphones would have significantly more scattering off the probe which could deteriorate the results. Thus, the advantages and disadvantages of each probe configuration must be weighed in light of the bias error presented in this chapter to select the optimal probe configuration for the type of field and quantities of interest.

Chapter 5

Wavepacket representation of high-performance military jet noise from PAGE intensity estimates

5.1 Introduction

The impact of high-performance military aircraft noise on nearby personnel and surrounding communities is of vital concern because of the potential for hearing loss and human annoyance. In order to better predict the noise impact, modeling tools are needed that accurately predict the spatial variation of the frequency-dependent noise levels, particularly in the dominant noise radiation region to the rear of the aircraft. The dominant turbulent mixing noise from high-speed jets originates from the interaction of turbulent structures traveling along the shear layer with the ambient air.⁶¹ Direct measurement of the turbulence-ambient fluid interactions for an advanced tactical engine have not yet been possible, so the noise radiation must be modeled.

Models take two forms. First, noise fields are calculated from computational aeroacoustics models. Although significant advances in numerical modeling of heated supersonic jets⁶²⁻⁶⁸ have occurred, the computational cost is still prohibitive in many circumstances. Second, rather than modeling the jet-fluid interaction, an acoustic equivalent source model based on e.g., simple sources,^{69, 70} wavepackets,⁷¹ or wave functions⁷²⁻⁷⁴ can represent the noise region and be used to predict the radiated sound field. This article describes the development of an equivalent wavepacket source model for the F-22A Raptor ground run-up noise that uses vector acoustic

intensity measurements^{14, 75} in its optimization. This approach, which requires relatively few measurement locations, is an efficient alternative to other pressure-based equivalent source models obtained from beamforming⁷⁶ and acoustical holography.⁷²

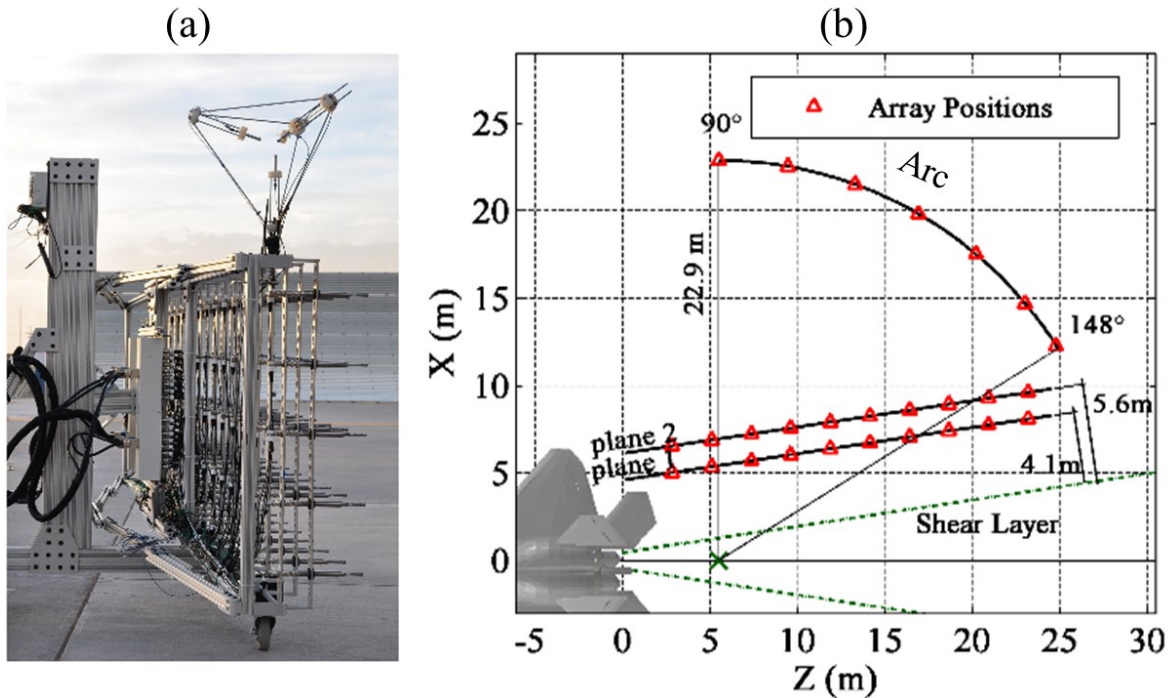


Figure 5.1. Experimental Setup. (a) Photograph of the intensity probe on top of the 90 microphone array. (b) Schematic of noise measurements of a tethered high-performance military aircraft. The red triangles indicate the positions of the 90 microphone array.

An extensive set of noise measurements in the vicinity of a tethered F-22A were made jointly by the Air Force Research Laboratory, Blue Ridge Research and Consulting, LLC, and Brigham Young University. A detailed description of the experiment is found in Wall *et al*⁷⁷. A custom, three-dimensional intensity probe shown in Fig. 5.1 (a), developed originally for rocket noise source measurements^{78, 79} was placed on top of an array of microphones that was moved to the locations indicated by the red triangles in Figure 5.1 (b) and at a height of $y = 2.54$ m. One F-22A engine was sequentially operated at four engine conditions: idle, intermediate (80% ETR), military (100% ETR), and afterburner, while the other engine was held at idle.

The F-22 data set has been analyzed in multiple ways to explore possible equivalent source representations of the noise. The first equivalent source model of the F-22 noise⁶⁹ was simulated with distributions of correlated and uncorrelated line arrays of monopoles and their image sources over a ground reflecting plane.⁸⁰ This field represented the two-source model of jet turbulent mixing noise. The simulated model was matched to the F-22 sound pressure level measurements. Subsequent equivalent source modeling efforts^{76, 81} have been based on an analytical wavepacket representation of the jet noise.⁸² Wavepackets share characteristics with instability wave theory that has been used to model the hydrodynamic and near-field acoustic pressure fluctuations.^{71, 83-89} Equivalent source wavepackets have been deduced from the decomposition of level-based, ground array measurements into contributions associated with fine and large-scale turbulent structures.⁹⁰ The resulting wavepackets show a remarkable degree of self-similarity across frequency. In addition, the source distributions obtained from a beamforming method has been decomposed into a multiple-wavepacket representation that can be used to predict not only the levels of the sound field but also the coherence properties.⁷⁶ This paper describes an equivalent source wavepacket-based model for the aeroacoustic noise obtained from the acoustic intensity measurements.

Although the use of intensity measurements to determine aeroacoustic source characteristics is rare, some prior examples exist. Although details are limited to a conference abstract, Roth⁹¹ used a two-microphone intensity probe to characterize the near and far fields of hot and cold jets in an anechoic chamber. Results were verified by comparing to jet noise prediction models and by substituting a loudspeaker for the jet. Jaeger and Allen⁹² ray-traced two-dimensional intensity measurements to obtain a compact centerline source region for a Mach 0.2 to 0.6 laboratory-scale cold jet. More recently, efforts to characterize the noise sources in

small⁷⁹ and large solid^{15, 78} rocket motors using near-field vector intensity resulted in the opportunity to take similar measurements on the F-22A as part of the overall measurement campaign.^{14, 77} Wideband intensity calculations were obtained at 27 locations to the sideline and the rear of the F-22 engine nozzle exit plane with the PAGE method for calculating intensity vectors.⁵² Then, the frequency-dependent vectors whose magnitudes were within 3 dB of the maximum were ray-traced back to the jet centerline to characterize the dominant source region. A complementary numerical study¹⁴ showed that this approach resulted in identification of the source region that radiated the top 1-2 dB of energy.

This article builds on the recent intensity-based source characterization and uses the measured intensity vectors to obtain an equivalent wavepacket-based source representation of the jet noise. The analytical wavepacket model proposed by Papamoschou⁷¹ is used to define the amplitude and phase of the equivalent source. A simulated annealing optimization is employed to obtain the frequency-dependent wavepacket parameters that minimize the difference between the measured and modeled acoustic intensity vectors for military (MIL) and afterburner (AB) engine conditions. The results show that a single-wavepacket model from a limited number of intensity measurements reasonably reproduces the levels of the measured field levels and has features consistent with those deduced directly from ray tracing the maximum acoustic intensity vectors. Limitations of using a single wavepacket to model the entire sound intensity field are discussed.

5.2 Methods

5.2.1 Model

A wavepacket has been described as a spatially extended disturbance characterized by an axial amplitude distribution that grows, saturates and decays, with a spatial phase relationship, which produces directional radiation⁸⁸ and correlation lengths longer than the integral length scales of

the turbulence⁹³. For laboratory-scale jet noise, wavepacket characteristics have been found in the turbulent source region, the hydrodynamic near field⁹⁴ and the acoustic far field^{71, 82}. A wavepacket-like representation of jet noise has been investigated for laboratory-scale jet noise experiments. For example, Papamoschou⁷¹ showed that the far-field acoustic levels from a cold, lab-scale Mach 0.9 jet can be modeled as the field from a single pressure wavepacket if a monopole was included to account for the sound radiation to the side of the engine nozzle. Given their relative prominence in laboratory-scale studies, this wavepacket ansatz provides a convenient starting point for finding an intensity-based equivalent source model for the noise radiation from high-power jet engines. This work similarly attempts to show that a single wavepacket, which defines the source strengths and phase relationship of a line array of monopoles can be used to model the acoustic intensity from a tethered aircraft at military and afterburner conditions.

Although wavepackets are most commonly described in terms of acoustic pressure along some surface,^{71, 81, 82} radiated acoustic vector intensity is most easily calculated from a volume-velocity wavepacket representation. A volume-velocity wavepacket defines an axial source strength distribution along the jet centerline, which in practice, is accomplished by assigning the magnitudes and phases of the wavepacket to a closely-spaced line array of acoustic point sources. While several analytical wavepacket models have been proposed. The analytical wavepacket model of Papamoschou⁷¹ is chosen for this work, but represents complex source strength, \tilde{Q} , rather than the nozzle lip-line pressure. The wavepacket defines the relative amplitude and phase of the n th point source as a function of downstream distance along the centerline, z_n , and angular frequency, ω , as

$$\tilde{Q}_n = \tilde{Q}(z_n, \omega) = \tanh \left[\left(\frac{z_n}{b_1} \right)^{g_1} \right] \left(1 - \tanh \left[\left(\frac{z_n}{b_2} \right)^{g_2} \right] \right) \exp \left(- \frac{j\omega}{U_c} z_n \right). \quad \text{Eq. 5.1}$$

The convective velocity, U_c is frequency dependent and determines the relative phase between point sources. Physically, the ratio of the ambient sound speed, c_0 to U_c has been shown to determine the peak angle of the Mach wave radiation lobe in supersonic jets:

$$\cos \theta_{\text{peak}} = \frac{c_0}{U_c}, \quad \text{Eq. 5.2}$$

where θ_{peak} is measured relative to the jet centerline with an origin at the microphone array reference point (MARP). The parameters of the first hyperbolic tangent term, b_1 and g_1 of Eq. 5.1, control the length scale and the rate of the growth of the wavepacket amplitude. Similarly, the parameters in the second hyperbolic tangent term, b_2 and g_2 dictate the length scale and rate of the amplitude decay.

As examples of how the growth, decay, and phase relationship modeling parameters affect the amplitude distribution, a series of normalized wavepacket shapes is shown in Figure 5.2, with one parameter varied at a time relative to the baseline case. Decreasing the value of U_c in Figure 5.2 (b) affects the relative phase across the wavepacket distribution, thereby lessening the radiation angle, but does not change the amplitude envelope relative to the baseline case shown in Figure 5.2 (a). On the other hand, adjustments in b_1, b_2, g_1, g_2 control both the extent and rate of the wavepacket rise and decay, as illustrated in Figure 5.2 (c) - (f), respectively. These five parameters are varied in a simulated annealing optimization algorithm to find frequency-dependent wavepacket representation of the equivalent source strengths that model the measured intensity.

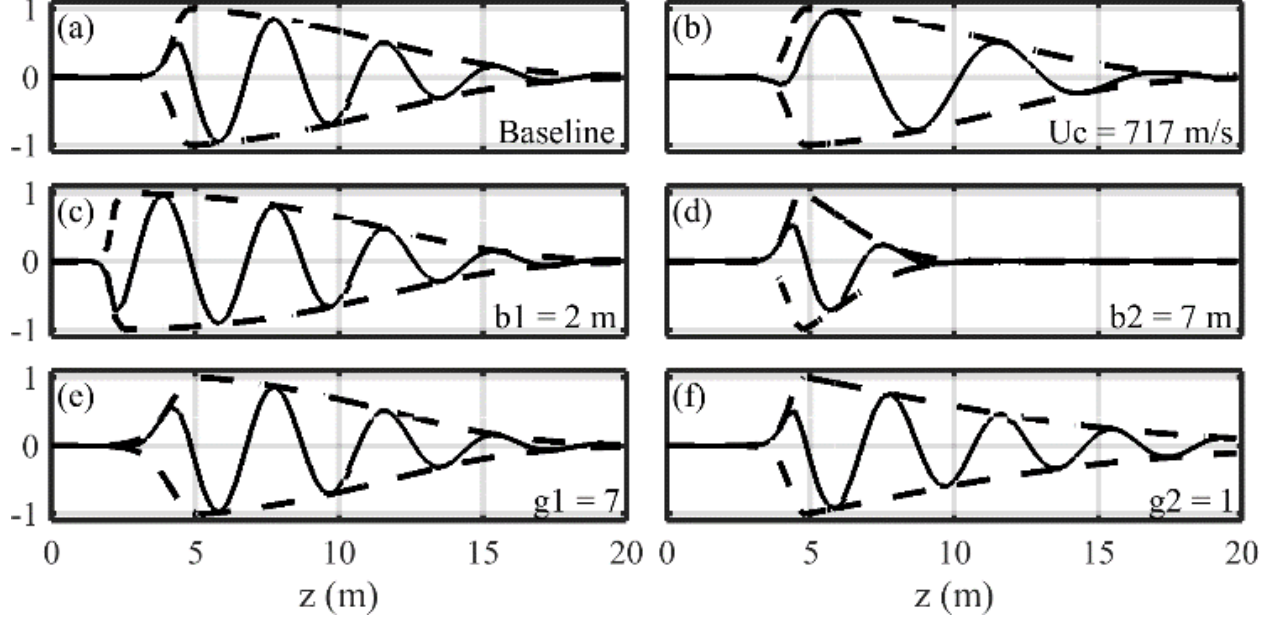


Figure 5.2. Various normalized wavepacket shapes. The baseline parameters are $U_c = 478$ m/s, $b_1 = 4$ m, $b_2 = 14$ m, $g_1 = 14$ m, and $g_2 = 2$ m. For the various plots (b)-(f), one parameter is changed from the baseline as indicated in the plot.

To calculate the acoustic intensity at a field location from the wavepacket source model, the pressure and particle velocity fields are needed. The contribution to the complex pressure at field location, \vec{r} , from the n th source, $\tilde{p}_n(\vec{r})$, may be written as

$$\tilde{p}_n(\vec{r}, \omega) = \frac{j\rho_0 c k \tilde{Q}_n \exp(-jk r_n)}{4\pi r_n}, \quad \text{Eq. 5.3}$$

where r_n is the distance from the n th point source location \vec{z}_n to the pressure location \vec{r} , k is the wavenumber, and \tilde{Q}_n is calculated according to Eq. 5.1. The linearized Euler's equation for a time-harmonic field is used to obtain the particle velocity at the desired location, $\tilde{u}_m(r)$:

$$\begin{aligned} \tilde{u}_n(\vec{r}, \omega) &= \left(\frac{j}{\rho_0 \omega} \right) \nabla \tilde{p}_n \\ &= \frac{\tilde{Q}_n \exp(-jk r_n) (1 + jk r_n)}{4\pi r_n^2} \hat{r}_n, \end{aligned} \quad \text{Eq. 5.4}$$

and \hat{r}_n is the unit direction from the source to the desired location.

The total contribution of all of the point sources to the acoustic intensity is found by the coherent summation of the pressure and the particle velocity. The time-averaged acoustic intensity at location r is modeled by

$$\vec{I}(\vec{r}, \omega) = \frac{1}{2} \text{Re} \left\{ \left(\sum_{n=1}^N \tilde{p}_n(\vec{r}, \omega) \right) \left(\sum_{n=1}^N \tilde{u}_n^*(\vec{r}, \omega) \right) \right\}, \quad \text{Eq. 5.5}$$

where * indicates the complex conjugate and the summation is over the N point sources.

This wavepacket-based model for the acoustic intensity could be modified to include an image source to account for the ground-reflected sound waves from the concrete run-up pad. However, in this study, unlike Harker et al.⁷⁶ and Wall et al.⁷², the image source is not incorporated because the sparseness of the intensity measurements does not yield sufficient information about the ground reflections for its meaningful inclusion in the model.

5.2.2 Simulated annealing algorithm

A simulated annealing algorithm⁹⁵ is used to find the volume velocity wavepacket parameters that provide the best match to the measured acoustic vector intensity. The algorithm makes random steps in the multidimensional parameter space. The step size in each of the five wavepacket model parameters is a random number multiplied by the difference between the upper and lower allowable bounds for that parameter. A scale factor is included that allows the algorithm to make smaller steps as the annealing progresses in order to improve convergence.⁹⁶ The simulated annealing algorithm is designed to always accept jumps that reduce the selected cost function (a downhill jump), and with a certain probability, accept uphill jumps via the Metropolis criteria⁹⁷ in search for the global minimum. The probability of accepting an uphill jump decreases as the algorithm progresses.

The bounds on these parameters are chosen to represent a wide range of wavepacket shapes. First, the boundaries for the convective speed, U_c , are selected to provide a physically realistic direction of the maximum radiation angle. An interpolation of the seven intensity measurements along the 22.9 m arc in Fig. 1 is used to find an appropriate range of radiation angles and from Eq. 5.2, corresponding bounds for U_c . Note that angles are defined relative to the measurement origin in Fig. 5.1 (a), rather than $z = 0$, because the dominant jet noise source is known to be downstream of the nozzle exit plane. This choice of origin allows the peak radiation angles obtained from the 22.9 m arc to better align with observed far-field directivity angles.⁹⁸ Because of the limited angular resolution in measuring peak radiation angle and to allow the algorithm flexibility in optimizing parameter choices, an uncertainty of $\pm 10^\circ$ about the peak angle is converted to a range of convective velocities using Eq. 5.2. This process allows for physically realistic bounds to be set on the values of U_c sampled in the simulated annealing algorithm

For the remaining four parameters, although there is not a direct tie to measurements as in the case of U_c , general physical features are used to set constraints. Since b_1 and b_2 correspond to the length scale of the rise and fall of the source region, the upper bound on each is the length of the modeled source and the lower limit is set to 0.1λ . An additional bound was $b_1 \geq b_2$, because numerical experiments showed almost no change in wavepacket shape for $b_1 < b_2$. Finally, from many prior jet noise source characterizations obtained from a variety of methods, it is expected that the source distribution should rise faster than it decays.⁹⁹⁻¹⁰² This translates into the constraint that $g_1 > g_2$ for the sampled parameters.

The simulated annealing optimization seeks to maximize the agreement between the modeled and measured intensity vectors by minimizing the cost function E . Because of the

multi-dimensional nature of the vectors, the cost function, E , is the Euclidian distance between modeled and measured vectors,

$$E = \frac{1}{27} \sum_{a=1}^{27} (I_{wp_{x_a}} - I_{meas_{x_a}})^2 + (I_{wp_{y_a}} - I_{meas_{y_a}})^2, \quad \text{Eq. 5.4}$$

where $I_{wp_{x_a}}$ is the x component of the wavepacket-based modeled intensity at location a and $I_{meas_{x_a}}$ is the x component of the intensity from the measurement of the F-22. Similarly, $I_{wp_{y_a}}$ is the y component from the model and $I_{meas_{y_a}}$ is the y component of the intensity from the measurement of the F-22. This cost function guides the simulated annealing algorithm to obtain wavepacket modeling parameters that achieve the best overall agreement between the magnitude and angle of the modeled and measured intensity vectors.

An example of the convergence of the simulated algorithm for 10 trials with random initial parameter choices is shown in Figure 5.3. For all cases, a minimum error was reached in fewer than 10,000 iterations. Furthermore, the trial runs converged to nearly the same cost, indicating convergence to an equivalent minimum.

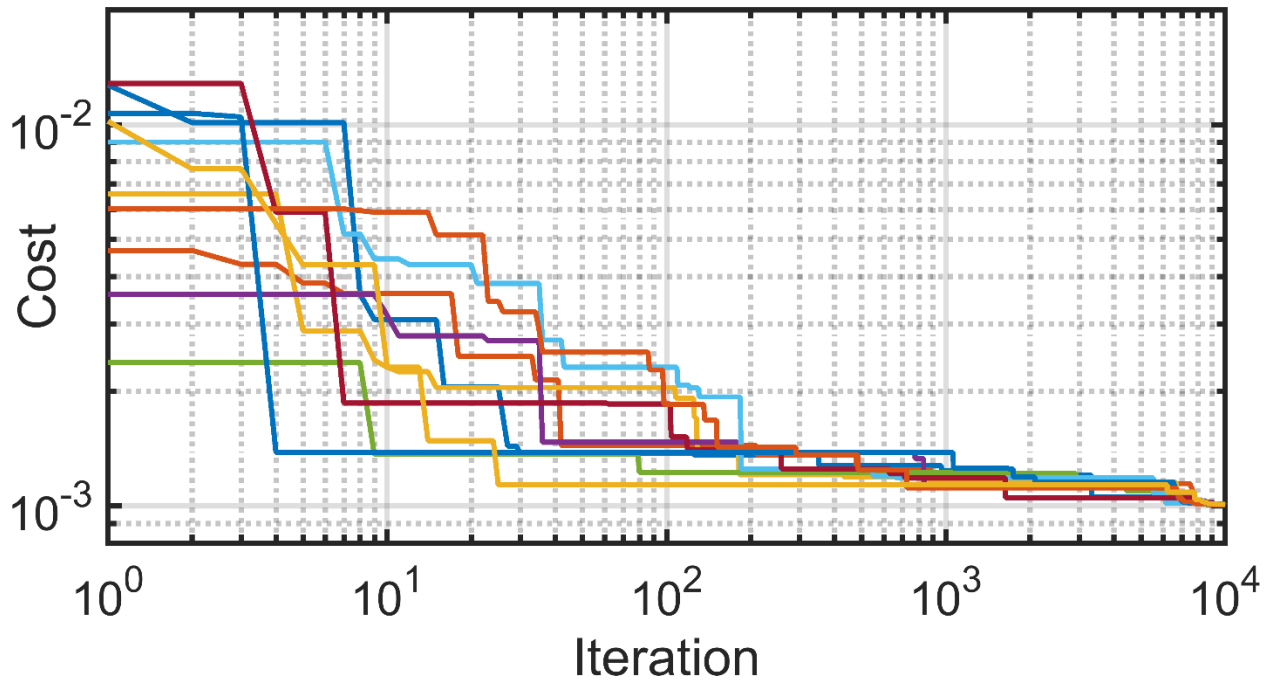


Figure 5.3. The various cost functions for military engine condition at 125 Hz for 10 different optimization runs.

5.2.3 Verification of Optimization

Before applying the optimization method for the F-22A field, the simulated annealing procedure was first applied in a numerical case comparable to the volume-velocity wavepacket obtained from the F-22 measured intensity at 125 Hz and military engine condition. This wavepacket, with known parameters, is used to calculate the pressure, particle velocity, and radiated intensity at the F-22A measurement locations (see Fig. 5.1). The resulting simulated intensity vectors at the measured locations are input for the simulated annealing algorithm, which returns an optimized set of wavepacket parameters. Ideally, the optimized intensity-based wavepacket should exactly match the source wavepacket, resulting in a cost function of zero. However, the simulated annealing algorithm is a heuristic approach and does not guarantee an exact match.

The optimization validation consisted of 100 trials, each with a different initial random starting point within allowable bounds. Table 5.1 lists the mean and the standard deviation of the

optimized wavepacket parameters and the actual source parameters used to simulate the intensity vectors. The mean optimized values are very close to the correct value with the optimized values falling within one standard deviation from the mean. A greater number of trials or removing all the results that yield a cost function much greater than the lowest cost function would further improve results.

Table 5.1. Actual and optimized wavepacket parameters for a numerical case comparable to the wavepacket obtained for the F-22 measured intensity at 125 Hz and military engine condition. The top row lists the chosen parameters for the simulated wavepacket. The second and third row indicate the mean and standard deviation, respectively, after the 100 optimizations.

	U_c (m/s)	b_1 (m)	b_2 (m)	g_1	g_2
Source Parameters	478	4.4	14.2	13	2.7
Optimized Results	478 ± 4	4.3 ± 0.2	14.1 ± 1.2	17.5 ± 6.1	2.7 ± 0.3

In addition to demonstrating the feasibility of obtaining intensity-based wavepackets for the F-22A, the verification test shows that the cost function is more sensitive to changes in some wavepacket parameters than others. The b_1 parameter has a very small standard deviation (5%) indicating that good results are only achievable with an accurate estimate of this parameter. On the other hand, the g_1 parameter has a very large standard deviation (35%) indicating that the model is not as selective for this parameter and many different values of g_1 can provide similar results. This understanding of parameter sensitivity is useful in obtaining and interpreting the jet noise field results.

5.3 Results

For the tethered F-22A with one engine operating at both military and afterburner conditions, the intensity-optimized wavepackets are obtained at one-third octave band center frequencies. In Sec. 5.3.1, an example of the optimization results is shown when the F-22

intensity vectors at 125 Hz and military engine condition is the input. In Sec. 5.3.2, the wavepacket source and peak radiation directivity are compared with the measured intensity vectors. In Sec. 5.3.3, the same comparison is carried out for afterburner condition.

5.3.1 Example of optimization results

Before proceeding to a broadband, wavepacket-based source characterization, examples of the agreement between the wavepacket-predicted and measured intensity at military condition are displayed in Figure 5.4-5 for 125 Hz and Figs. 5.6-7 for 1000 Hz. Figure 5.4 (a) shows the optimized wavepacket envelope and corresponding real part at 125 Hz. The source is comprised of 3-4 wavelengths and the dominant source region (<1 dB) is between 4.25 and 8.5 m. Using Eq. 5.5, this optimized volume velocity wavepacket results in the predicted intensity levels and direction at the plane 1, plane 2, and arc measurement locations shown in Figure 5.1. A comparison of these results with the measured intensity vectors, in Figs. 5.4 (b) – (g), shows that the wavepacket-predicted intensity vectors are within 3 dB at most locations of the measured sound intensity level (SIL) and within 3° of measured direction. A two-dimensional view of the measured intensity vectors (at a height of 2 m) is displayed in Figure 5.5 (a) and the wavepacket-predicted intensity field in Figure 5.5 (b). The modeled magnitude of the predicted intensity is shown over the entire aperture with vectors shown at the measurement points. Although the field predictions are displayed within the jet shear layer, which is denoted by the dashed line, these intensity levels are not related to the turbulent jet exhaust. Thus, at 125 Hz, good agreement exists between a wavepacket-based ESM prediction and the intensity measurement at 125 Hz for locations in the aperture spanned by plane 1 and the arc.

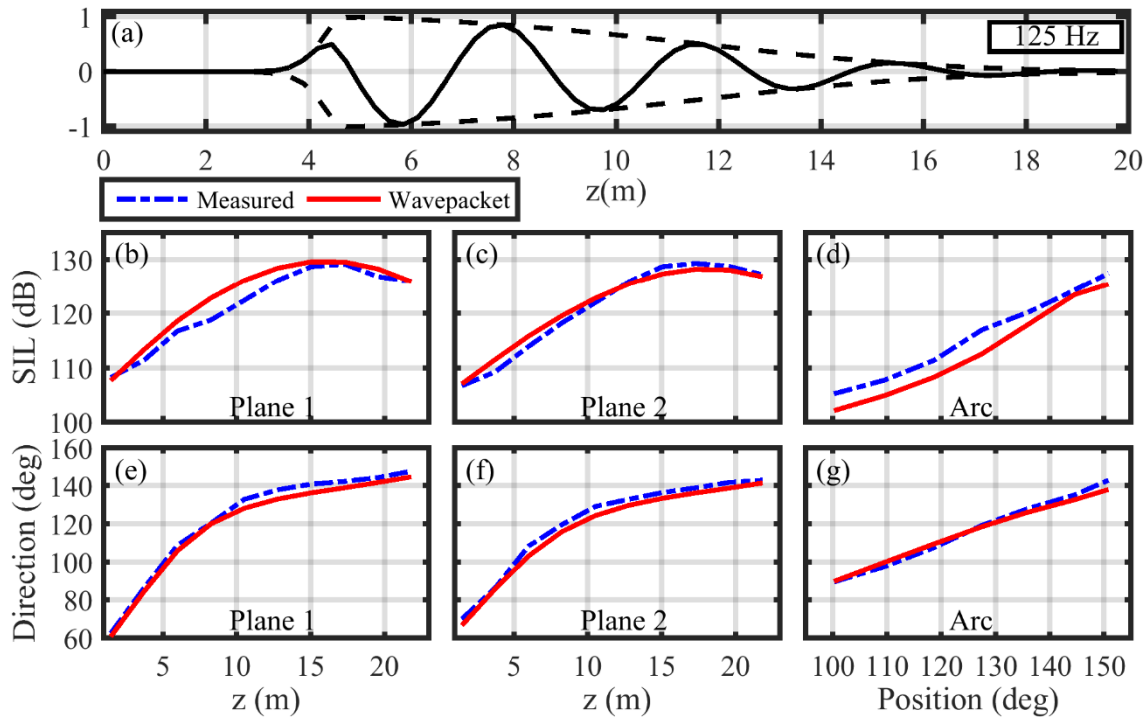


Figure 5.4. The optimized wavepacket (a) for military engine condition at 125 Hz. The center line shows the measured (blue dashed) and modelled (red) intensity magnitude for the three intensity probe measurement plane 1 (b), plane 2 (c), and the 22.9 m arc (d), shown in Figure 5.1(b). The bottom line shows the agreement of measured and modelled intensity directions for the same locations.

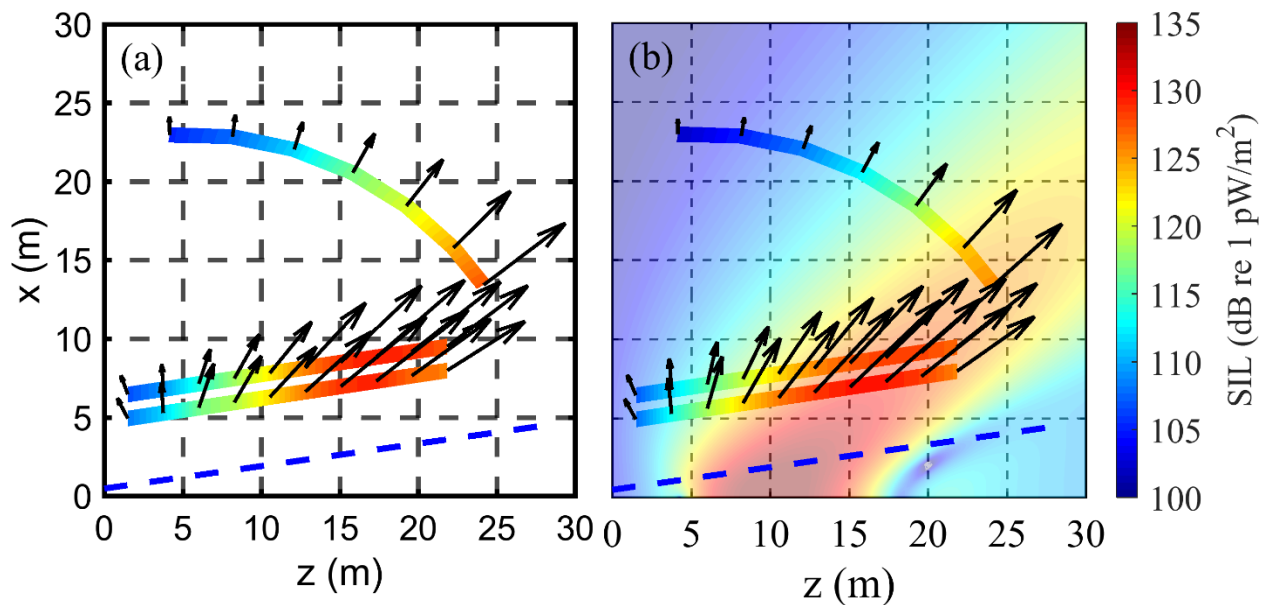


Figure 5.5. For 125 Hz and military engine condition, subplot (a) shows the measured afterburner acoustic intensity vectors, and subplot (b) shows the wavepacket-predicted intensity vectors. Subplot (b) has the wavepacket-predicted intensity level throughout the region. The dashed line indicates the approximate jet shear layer. The predicted levels inside the shear layer are not related to the turbulent flow and have no meaning.

The wavepacket-based ESM is frequency dependent. The optimized wavepacket for the 1000 Hz, shown in Figures 5.6 (a) is significantly smaller than at 125 Hz, with the large amplitude portion extending from 3.1 m to 3.3 m, which is less than half a wavelength span. In general, at high frequencies (1000 Hz or more) the high-amplitude region of the optimized wavepackets is very compact and behaves almost like a point source. Despite this compact shape, the agreement between the wavepacket-predicted and measured intensity vectors is good. The 1000 Hz optimized wavepacket produces predicted intensity levels that are within 5 dB of the measured levels and predicted directions that are within 5° of the measured intensity vector directions on the measurement planes and the arc, as shown in Figure 5.6 (b) – (g). The two dimensional comparison of the intensity vectors at the measurement location and the overall predicted intensity field levels are displayed in Figure 5.7 (a) and (b), respectively.

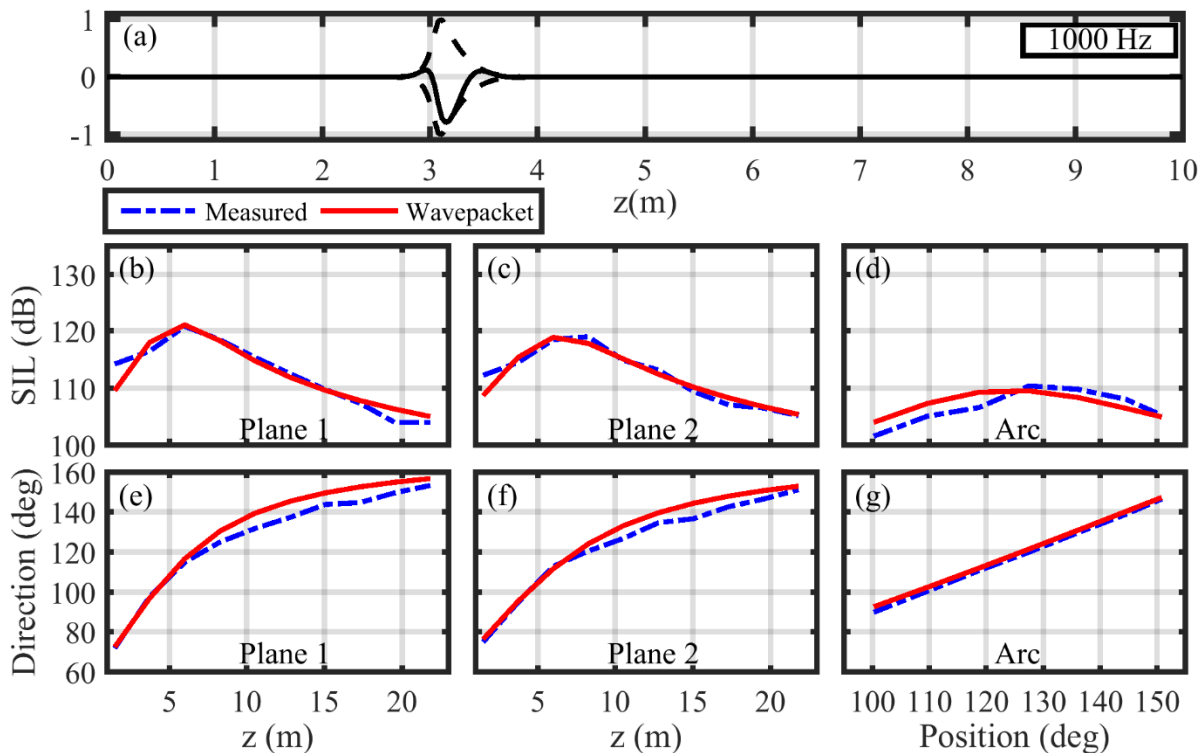


Figure 5.6. Same as Figure 5.4, but at 1000 Hz.

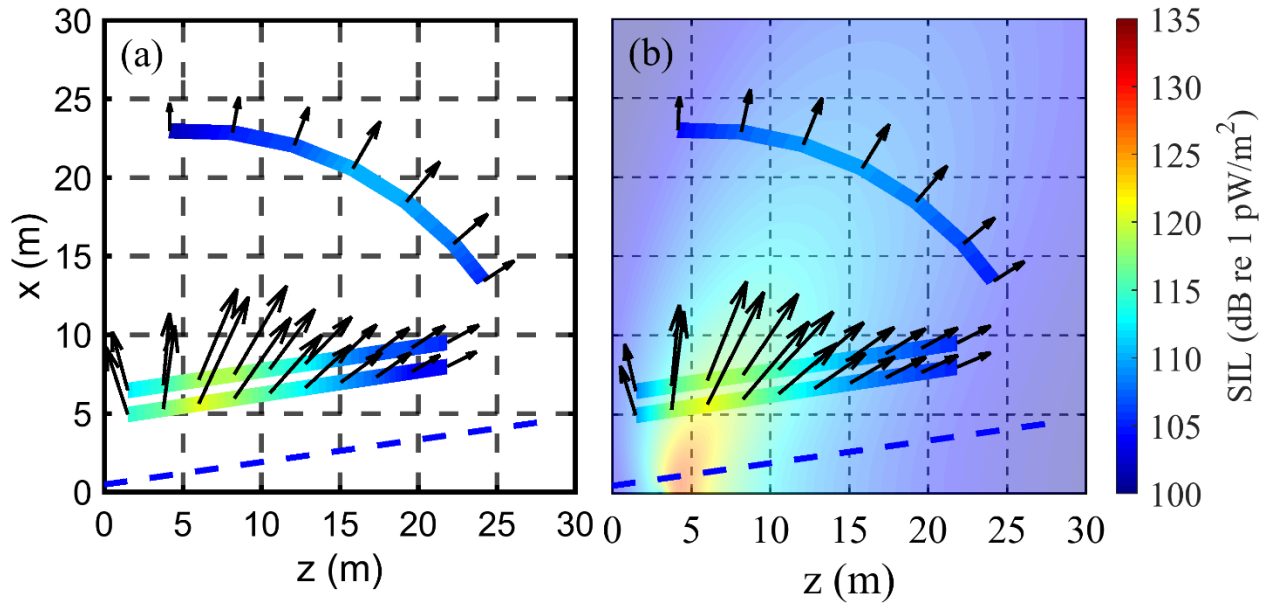


Figure 5.7. Same as Figure 5.5, but at 1000 Hz.

Some additional general comments regarding the optimizations are worthwhile. In prior work, most wavepacket envelopes that have been used to model the sound radiation from large-scale turbulent structures have smoothly varying contours with gentle rise and fall characteristics.^{71, 81} However, with this study, the optimization algorithm consistently converged to a wavepacket shape with a very steep rise portion. Further modeling investigations showed that this rise was critical to increasing the modeled sideline radiation to the measured levels; a more gradual rise typical of other results in the jet noise literature matches the downstream radiation but was found to consistently under predict the sideline levels. This may explain why Papamoschou⁷¹ found he had to add a monopole to the wavepacket model in order to better match the lower-level sound radiation at the sideline. Others^{83, 103} have also shown similar under-predictions at sideline angles.

Other observations involve intermediate frequencies between 125 and 1000 Hz. First, at 250 Hz, the agreement between the single wavepacket model and the measured field is less because of a dual radiation lobe in the measured data. The dual radiation lobe has been

described by many researchers.^{80, 104, 105} An ESM based on a single wavepacket cannot fit this dual lobe field perfectly and so the optimization yields a wavepacket with a broader source region than expected in order to capture the second radiation lobe. Addition of a second wavepacket has been shown to adequately model both radiation lobes.⁷⁵ Second, because these measurements were taken over a hard surface, a ground reflection produced a broad interference null in the spectrum around 500 Hz at the 22.9 m arc. Although there are similar spatial trends between the measured and modeled intensity fields around 500 Hz, the model over predicts the measurement by 5-8 dB. The addition of an image-source wavepacket did not help reduce the error between the measurement and the optimized model. Beyond the measurement array sparseness, the most likely cause is the addition of the direct and image wavepackets is assumed to be perfectly coherent, resulting in much deeper interference nulls and a significant under-prediction by the modeled field.

5.3.2 Military engine condition

In this section, the source characteristics deduced by Stout et al.¹⁴ using ray-tracing are compared with the optimized wavepackets for military engine condition. The comparison is carried out between 100 and 1000 Hz, which contains much of the dominant noise radiation by the F-22A. In a numerical study, Stout et al.⁷⁵ showed that ray tracing the intensity vectors with magnitudes within 3 dB of the peak correctly predicted the top 1-2 dB of the source region. Figure 5.8 shows the ray-traced source region from Stout *et al.*⁷⁵ (red) compared to the top 2 dB of the optimized wavepackets (green). The ray-traced and wavepacket maximum source regions exhibit the same trends: the source region is centered at greater than 5 m downstream of the nozzle at 100 Hz and then moves upstream with frequency, eventually reaching asymptotic behavior. However, the wavepacket model predicts that the maximum source region is both

farther upstream and, above 500 Hz, more compact than the ray-traced maximum. In fact, it appears the wavepacket model source region is roughly centered on the upstream edge of the maximum source region obtained from ray tracing. This could be due to the shape of the wavepackets. The wavepackets rise quickly and fall slowly so the peak is near the upstream edge; although the full extent of the wavepacket is larger, the peak and most of the energy is on the upstream edge. Nevertheless, the optimized wavepacket peak locations match the ray-traced source location to within 1 m (about 1.5 equivalent engine nozzle diameters), helping to establish the robustness and reasonableness of the optimization process.

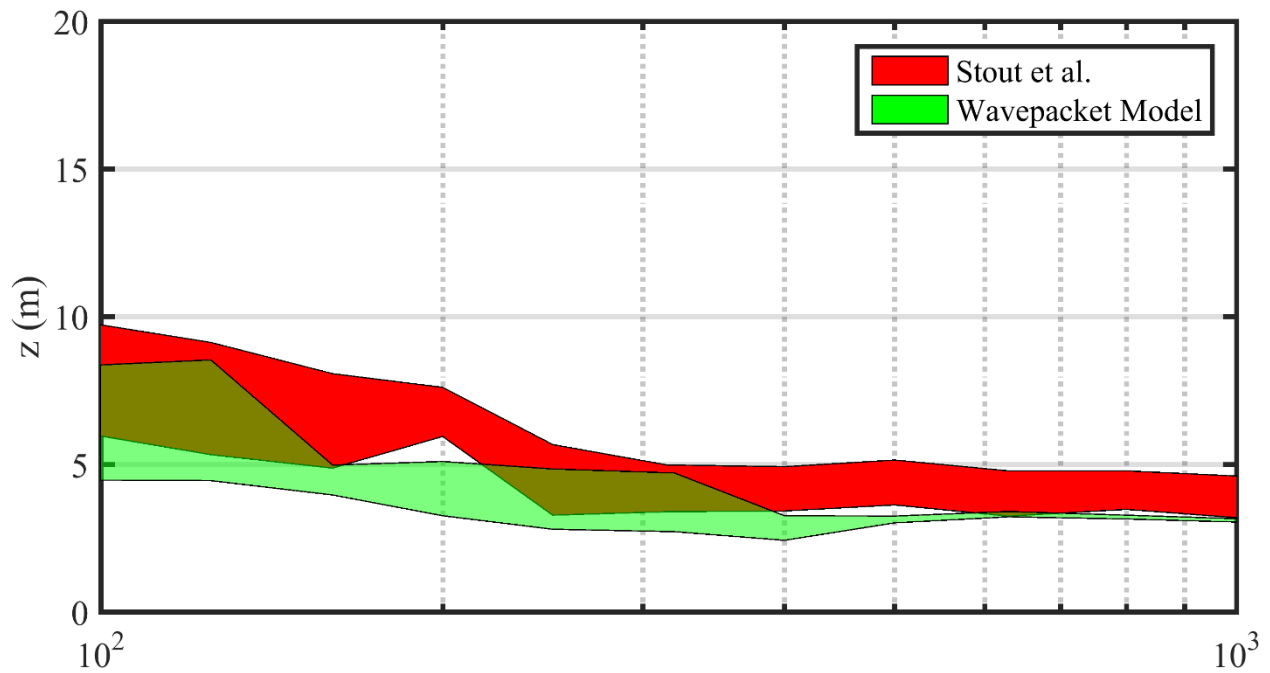


Figure 5.8. Comparison of the estimated maximum equivalent source regions from the ray-tracing method employed by Stout *et al.* and the optimized wavepacket ESM for the F-22 when a single engine was operated at military engine conditions

Another result shown by Stout *et al.* is the range of angles of measured intensity vectors that have a magnitude within 3 dB of the maximum at plane 2. A comparison can be made with the optimized wavepacket model by calculating the wavepacket-based intensity vectors at the measurement locations and finding the intensity angle range that corresponds to a similar 3-dB

down region. These results are shown in Fig. 5.9 between 100 and 1000 Hz for military power. In addition, the radiation angle obtained with Eq. 5.2 using the optimized values of U_c is plotted as a green dashed line. The measured and wavepacket-predicted directions for the intensity vectors along plane 2 follow the same trend, in that the peak radiation moves towards the sideline as frequency increases, agreeing with typical jet noise.^{61, 80, 99}, with a few exceptions. First, note that the optimized wavepackets yield a wider range of intensity angles (5-10°) at nearly all frequencies. This is likely due to the use of single wavepacket in the ESM, which, as mentioned rises particularly sharply in order to model the upstream radiation and is particularly compact at higher frequencies. Second, the wavepacket model gradually transitions to a lesser angle between 100 and 300 Hz, whereas the measurement shows an abrupt transition between 200 and 250 Hz. As noted by Stout et al.¹⁴, this abrupt transition is related to the relative dominance of the two radiation lobes. Below 200 Hz, the downstream lobe (~135°) dominates, while above 250 Hz, the upstream lobe (~120°) dominates. Because the single wavepacket model does not incorporate the dual lobe radiation, the predicted direction changes more gradually.

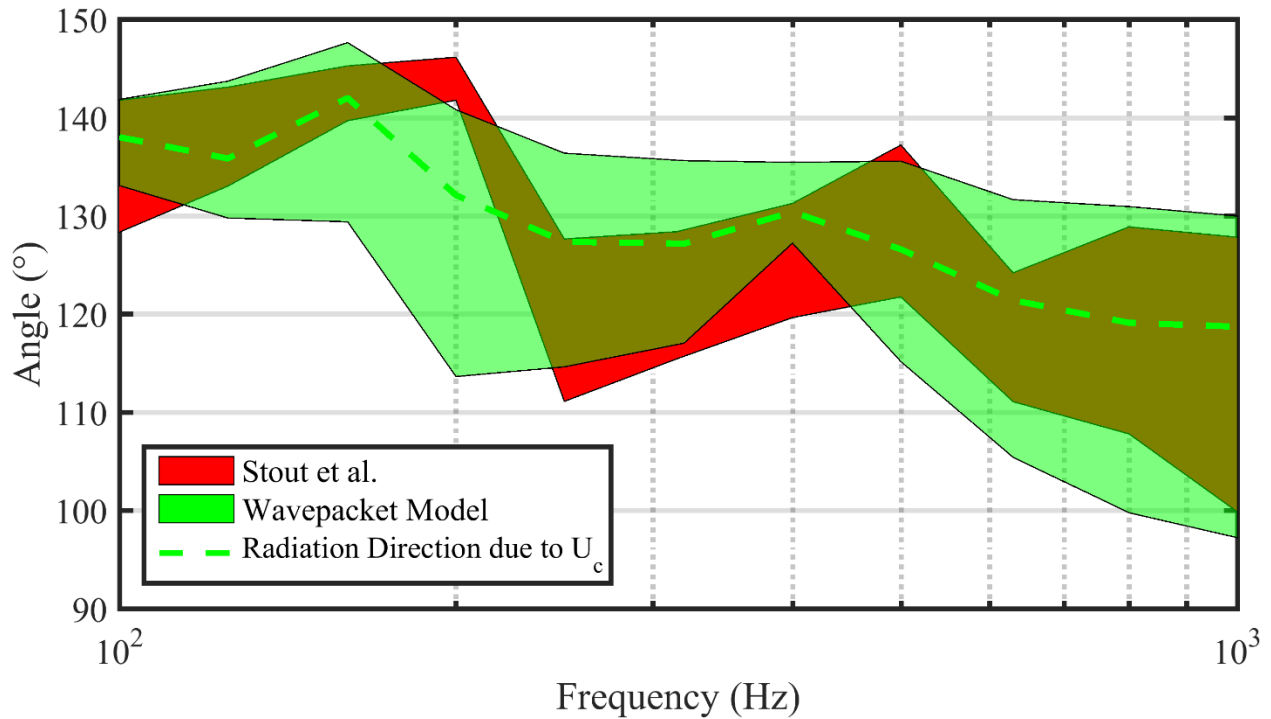


Figure 5.9. Comparison of the direction of the largest measured and wavepacket-predicted intensity vectors on plane 2 at military engine conditions. The dotted green line represents the peak radiation direction computed from the optimized convective velocity using Eq. 5.2.

5.3.3 Afterburner engine condition

The afterburner condition has some peculiarities. The measured intensity levels were not as smooth as the military engine conditions and so the wavepacket model does not fit the data as well. Thus, like the military condition, the optimized wavepacket model agrees best at low frequencies around 125 Hz and at higher frequencies (1000 Hz). In between these frequencies the wavepacket shape is almost rectangular. Despite this, there is still relatively good general agreement in the source region and directivity between the ray-tracing and wavepacket-predicted equivalent source models.

For the afterburner location, the maximum equivalent source region shrinks and moves upstream as frequency increases (Figure 5.10). At 100 Hz, the source region extends from about 6 m to 12 m. While similar to the estimated maximum source region shown by Stout et al.,¹⁴

which extends from about 7 m to 11 m, this work shows the equivalent source region as being broader and closer to the engine nozzle. As seen at military engine condition, the wavepacket-based equivalent source region tends to be narrower because of the need for the abrupt rise described before, except around 250 Hz where the dual lobe in the field is prominent.

Similarly, the directionality at afterburner is comparable between the two methods. There is good agreement at low and high frequencies. In the troublesome region (250 to 500 Hz) where the optimized wavepacket model has trouble getting good agreement with the measured data, the two methods disagree by roughly 10 degrees.

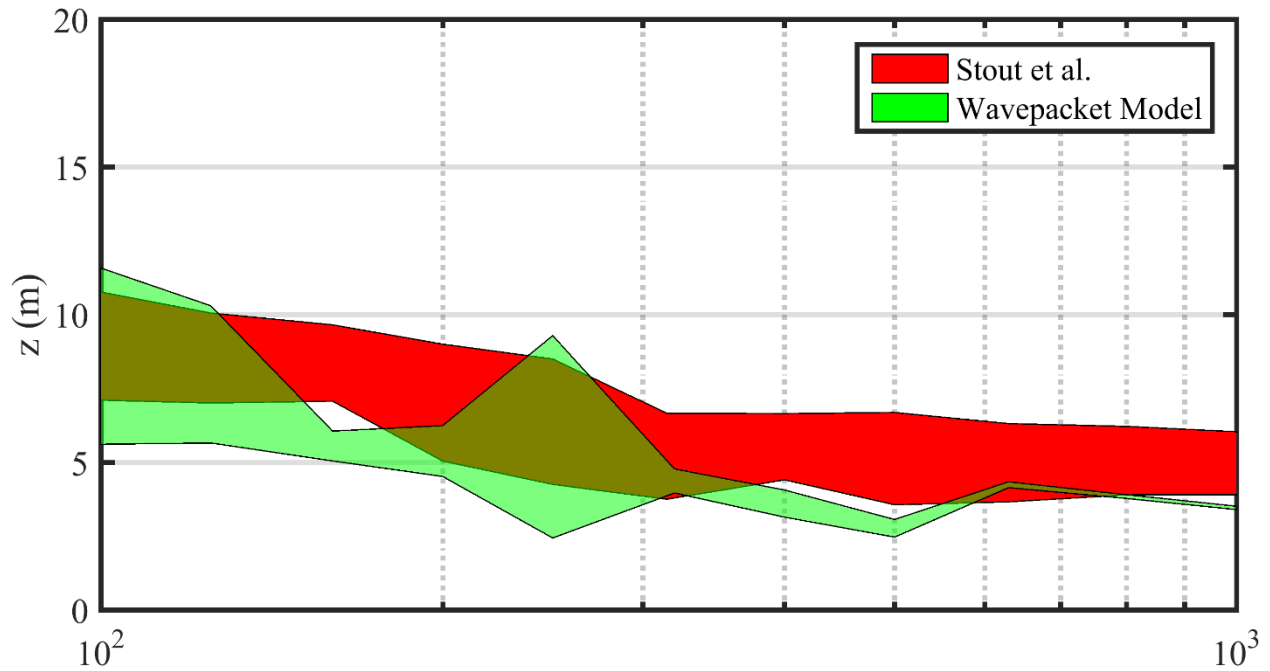


Figure 5.10. Comparison of the estimated maximum equivalent source region from the ray-tracing method employed by Stout et al. and the optimized wavepacket ESM for the F-22 when a single engine was operated at afterburner power.

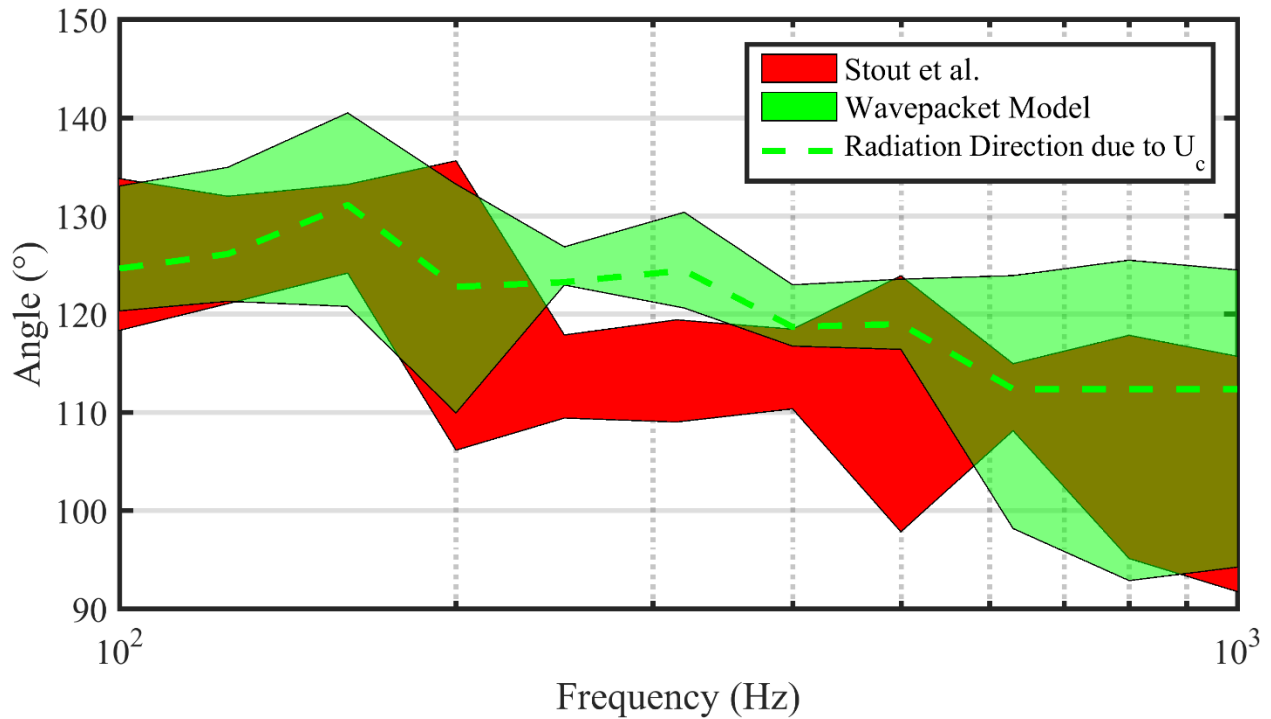


Figure 5.11. Comparison of the direction of the largest measured and wavepacket-predicted intensity vectors on plane 2 at afterburner engine conditions. The dotted green line represents the peak radiation direction computed from the optimized convective velocity using Eq. 5.2.

As is expected, the maximum equivalent source location estimated by both methods is further downstream for the afterburner engine condition's location than the military condition. Likewise, the main radiation from the afterburner engine condition radiates further upstream than the military engine condition. Furthermore, both engine conditions have small source regions with broad directivity at higher frequencies.

5.4 Conclusion

This work has presented the method and results of modeling the intensity field of a military jet aircraft at military and afterburner engine conditions with a single volume velocity wavepacket model for each frequency. The results compare favorably with previous work using intensity vectors to trace back to the centerline of the jet. The results do not agree perfectly, but the general method of optimizing a source model in order to get agreement between the

measured intensity data and the modeled intensity from the source can be used in a variety of situations. This optimized equivalent source model could then be used to predict acoustic quantities away from the source without a lot of computational expense.

Chapter 6

Conclusion

6.1 Conclusions

The PAGE method has previously been shown to work better than the traditional method to calculate active intensity.^{52, 53} But this thesis has shown that the PAGE method does a better job of estimating the center pressure and particle velocity than the traditional method. This does not mean that the PAGE method is better at handling all possible errors, but it does have better bias errors that are not dependent on frequency. Furthermore, by calculating the error for the complex pressure and particle velocity, analytical expressions for the bias error can be derived. Nevertheless, this method becomes tedious for every unique situation and field. A more general approach was demonstrated in which a wide range of acoustic fields could be simulated along with any conceivable probe configuration. This simulation has not been designed for other sources of error like phase calibration, scattering, or random noise; the simulation only shows the best possible result for the different methods and probes.

The choice of probe design and calculation method has the sole purpose of characterizing a real source. An equivalent source model was made for an F-22 Raptor using intensity measurements at two engine conditions. This application demonstrates the power of using intensity measurements to characterize a source. This work thus shows the benefit of using vector intensity to characterize sources and provides a method to account for the errors in analyzing vector intensity measurements.

6.2 Future Work

This thesis has only addressed one type of error in energy quantity estimation with ideal acoustic energy probes. Further work could address how well the PAGE method handles noise compared to the traditional method, and what the optimal way to reduce noise in the PAGE method is. Since the active intensity is dependent on pressure squared, it seems as though the noise might be magnified with the PAGE method. Furthermore, the effects of Gaussian noise on the phase estimate are of interest. Furthermore, a study of the scattering from these multi-microphone probes is important because a probe with more microphones seems to produce better intensity measurement results, but it is unclear how scattering affects the results. Plus, if higher order methods in energy quantity estimation, are to be used, then even more microphones are required.

There are some interesting applications of the PAGE method that still need to be studied. First, for rocket noise measurements, ideally a very large intensity probe to measure the very low frequencies is desired. The performance of large probes could be studied further. Second, a preliminary study of an ideal standing wave was studied, but it would be of great interest to know if and how the PAGE method can be applied to a reverberant room. An analytical model of a standing wave was examined, but the current implementation of the PAGE method failed to improve upon the traditional method. Work still needs to be done to improve and verify the PAGE results in a reverberant field. The analysis of this type of field is important because power measurements are often made in situ, where the field in a room could affect the measurement. Third, it would be interesting to apply the PAGE method to tonal, not broadband, noise. Currently, to unwrap the phase, a broadband source is needed. Theoretically, the PAGE method should work for tonal sources. For example, for active intensity, all that is needed is the center

pressure magnitude and the gradient of phase. The center pressure magnitude can be measured with a center microphone, and the gradient of phase is related to the wavenumber and the direction of propagation of the wave. Therefore, to find the gradient of phase, since the wavenumber is known, one simply needs to know the direction of propagation of the wave. Lastly, beamforming and holography both use pressures or particle velocities in the frequency domain to analyze a source. It is of interest to know if the same principles used in the PAGE method can be applied to these applications.

Appendix A

A.1 Derivations of two- and three-microphone expressions

A consistent methodology is used to derive all expressions described in Chapter 2. The methodology is to first estimate the pressure and particle velocity at the center of the microphone configuration using a truncated Taylor series. Then, using the estimations of the pressure and the particle velocity, the intensity, energy density, and impedance are found for each probe configuration and analysis method.

A.2 Traditional method two-microphone expression:

The pressure at the center of the probe is estimated to be

$$\tilde{p}_c(\omega) = \frac{\tilde{p}_2(\omega) + \tilde{p}_1(\omega)}{2}, \quad \text{Eq. A.1}$$

where \tilde{p}_2 is the complex pressure from the second microphone and \tilde{p}_1 is the pressure from the first microphone at angular frequency, ω . Each microphone is a distance d from the center of the microphones but in opposite directions.

The particle velocity will be

$$\tilde{u}(\omega) = \frac{j}{\omega\rho_0} \frac{\tilde{p}_2 - \tilde{p}_1}{2d}, \quad \text{Eq. A.2}$$

where ρ_0 is the density of air and $2d$ is the separation between the microphones.

The time-averaged active intensity is then

$$I_a(\omega) = \frac{1}{2} \text{Re}\{\tilde{p}_c \tilde{u}^*\} \quad \text{Eq. A.3}$$

$$\begin{aligned}
&= \frac{1}{2} \operatorname{Re} \left\{ \left(\frac{\tilde{p}_2 + \tilde{p}_1}{2} \right) \left(\frac{j}{\omega \rho_0} \frac{\tilde{p}_2 - \tilde{p}_1}{2d} \right)^* \right\} \\
&= \frac{1}{8\omega \rho_0 d} \operatorname{Re} \{ -j(\tilde{p}_2 \tilde{p}_2^* - \tilde{p}_2 \tilde{p}_1^* + \tilde{p}_1 \tilde{p}_2^* - \tilde{p}_1 \tilde{p}_1^*) \} \\
&= \frac{1}{2\omega \rho_0 d} \operatorname{Im} \{ G_{12} \}.
\end{aligned}$$

The reactive intensity is

$$\begin{aligned}
I_r(\omega) &= \frac{1}{2} \operatorname{Im} \{ \tilde{p}_c \tilde{u}^* \} = \frac{1}{2} \\
&= \frac{1}{2} \operatorname{Im} \left\{ \left(\frac{\tilde{p}_2 + \tilde{p}_1}{2} \right) \left(\frac{j}{\omega \rho_0} \frac{\tilde{p}_2 - \tilde{p}_1}{2d} \right)^* \right\} \\
&= \frac{1}{8\omega \rho_0 d} \operatorname{Im} \{ -j(\tilde{p}_2 \tilde{p}_2^* - \tilde{p}_2 \tilde{p}_1^* + \tilde{p}_1 \tilde{p}_2^* - \tilde{p}_1 \tilde{p}_1^*) \} \\
&= \frac{1}{4\omega \rho_0 d} (G_{11} - G_{22}).
\end{aligned}$$

Eq. A.4

The potential energy is

$$E_p(\omega) = \frac{(\tilde{p}_2 + \tilde{p}_1)(\tilde{p}_2 + \tilde{p}_1)^*}{16\rho_0 c^2} = \frac{G_{22} + 2\operatorname{Re}\{G_{12}\} + G_{11}}{8\rho_0 c^2}.$$

Eq. A.5

The kinetic energy is

$$\begin{aligned}
E_k(\omega) &= \frac{\rho_0}{4} \left(\frac{j}{\rho_0 \omega} \frac{\tilde{p}_2 - \tilde{p}_1}{2d} \right) \left(\frac{j}{\rho_0 \omega} \frac{\tilde{p}_2 - \tilde{p}_1}{2d} \right)^* \\
&= \frac{1}{16\rho_0 \omega^2 d^2} (G_{22} + G_{11} - 2\operatorname{Re}\{G_{21}\}).
\end{aligned}$$

Eq. A.6

Specific acoustic impedance is

$$z(\omega) = \frac{\frac{\tilde{p}_2 + \tilde{p}_1}{2}}{\frac{j}{\rho_0 \omega} \frac{\tilde{p}_2 - \tilde{p}_1}{2d}} = -j\rho_0 \omega d \left(\frac{G_{21} + G_{11}}{G_{21} - G_{11}} \right).$$

Eq. A.7

A.3 Traditional method three-microphone expression:

The pressure at the center of the probe is estimated to be

$$\tilde{p}_c(\omega) = \tilde{p}_2(\omega). \quad \text{Eq. A.8}$$

where $\tilde{p}_2(\omega)$ is the pressure at the center microphone.

The particle velocity will be

$$\tilde{u}(\omega) = \frac{j}{\omega\rho_0} \frac{\tilde{p}_3 - \tilde{p}_1}{2d}. \quad \text{Eq. A.9}$$

where \tilde{p}_1 and \tilde{p}_3 are the measurements from the pair of microphones on the opposite sides of the center microphone and d from the center microphone.

The active intensity is then

$$\begin{aligned} I_a(\omega) &= \frac{1}{2} \text{Re}\{\tilde{p}_c \tilde{u}^*\} = \frac{1}{2} \text{Re}\left\{\tilde{p}_2 \left(\frac{j}{\omega\rho_0} \frac{\tilde{p}_3 - \tilde{p}_1}{2d}\right)^*\right\} \\ &= \frac{1}{4\omega\rho_0 d} \text{Re}\{-j(\tilde{p}_2 \tilde{p}_3^* - \tilde{p}_2 \tilde{p}_1^*)\} \\ &= \frac{\text{Im}\{G_{23}\} - \text{Im}\{G_{21}\}}{2\omega\rho_0 d}. \end{aligned} \quad \text{Eq. A.10}$$

The reactive intensity is

$$\begin{aligned} I_r(\omega) &= \frac{1}{2} \text{Im}\{\tilde{p}_c \tilde{u}^*\} = \frac{1}{2} \text{Im}\left\{\tilde{p}_2 \left(\frac{j}{\omega\rho_0} \frac{\tilde{p}_3 - \tilde{p}_1}{2d}\right)^*\right\} \\ &= \frac{1}{4\omega\rho_0 d} \text{Im}\{-j(\tilde{p}_2 \tilde{p}_3^* - \tilde{p}_2 \tilde{p}_1^*)\} \\ &= \frac{-\text{Re}\{G_{23}\} + \text{Re}\{G_{21}\}}{2\omega\rho_0 d}. \end{aligned} \quad \text{Eq. A.11}$$

The potential energy is

$$E_p(\omega) = \frac{G_{22}}{4\rho_0 c^2}. \quad \text{Eq. A.12}$$

The kinetic energy is

$$\begin{aligned}
 E_k(\omega) &= \frac{\rho_0}{4} \left(\frac{j}{\rho_0 \omega} \frac{\tilde{p}_3 - \tilde{p}_1}{2d} \right) \left(\frac{j}{\rho_0 \omega} \frac{\tilde{p}_3 - \tilde{p}_1}{2d} \right)^* \\
 &= \frac{1}{16\rho_0\omega^2 d^2} (G_{33} + G_{11} - 2\text{Re}\{G_{31}\}).
 \end{aligned}
 \tag{Eq. A.13}$$

Specific acoustic impedance is

$$z(\omega) = \frac{\tilde{p}_2}{\frac{j}{\rho_0 \omega} \frac{\tilde{p}_3 - \tilde{p}_1}{2d}} = -\frac{j2\rho_0\omega d G_{22}}{G_{32} - G_{12}}.
 \tag{Eq. A.14}$$

A.4 PAGE method two-microphone expression:

The pressure at the center of the probe is estimated to be

$$\tilde{p}_c(\omega) = \frac{|\tilde{p}_2| + |\tilde{p}_1|}{2} \exp \left[\frac{j}{2} (\angle \tilde{p}_2 + \angle \tilde{p}_1) \right],
 \tag{Eq. A.15}$$

where \tilde{p}_2 is the complex pressure from the second microphone and \tilde{p}_1 is the pressure from the first microphone at angular frequency, ω . Each microphone is d from the center of the microphones but in opposite directions.

The particle velocity will be

$$\tilde{u}(\omega) = \frac{\exp \left[\frac{j}{2} (\angle \tilde{p}_2 + \angle \tilde{p}_1) \right] \left[j(|\tilde{p}_2| - |\tilde{p}_1|) - \frac{(|\tilde{p}_2| + |\tilde{p}_1|)}{2} (\angle \tilde{p}_2 - \angle \tilde{p}_1) \right]}{2\omega\rho_0 d},
 \tag{Eq. A.16}$$

where a is the separation between the microphones.

The active intensity is then

$$\begin{aligned}
 I_a(\omega) &= \frac{1}{2} \text{Re}\{\tilde{p}_c \tilde{u}^*\} \\
 &= \frac{1}{2} \text{Re} \left\{ \left(\frac{|\tilde{p}_2| + |\tilde{p}_1|}{2} \right) \left[\frac{-j(|\tilde{p}_2| - |\tilde{p}_1|) - \frac{(|\tilde{p}_2| + |\tilde{p}_1|)}{2} (\angle \tilde{p}_2 - \angle \tilde{p}_1)}{2\omega\rho_0 d} \right] \right\} \\
 &= \frac{-(|\tilde{p}_2| + |\tilde{p}_1|)^2 (\angle \tilde{p}_2 - \angle \tilde{p}_1)}{16\omega\rho_0 d} = \frac{G_{11} + 2|G_{12}| + G_{22}}{8\omega\rho_0 d} \arg\{H_{12}\},
 \end{aligned}
 \tag{Eq. A.17}$$

where ρ_0 is the density of air and a is the separation between the microphones.

The reactive intensity is

$$\begin{aligned} I_r(\omega) &= \frac{1}{2} \text{Im}\{\tilde{p}_c \tilde{u}^*\} = \frac{1}{2} \text{Im} \left\{ \left(\frac{|\tilde{p}_2| + |\tilde{p}_1|}{2} \right) \left[\frac{-j(|\tilde{p}_2| - |\tilde{p}_1|) - \frac{(|\tilde{p}_2| + |\tilde{p}_1|)}{2} (\angle\tilde{p}_2 - \angle\tilde{p}_1)}{2\omega\rho_0 d} \right] \right\} \\ &= \frac{-1}{8\omega\rho_0 d} (|\tilde{p}_2| + |\tilde{p}_1|)(|\tilde{p}_2| - |\tilde{p}_1|) = \frac{G_{11} - G_{22}}{4\omega\rho_0 d}. \end{aligned} \quad \text{Eq. A.18}$$

The potential energy is

$$\begin{aligned} E_p(\omega) &= \frac{\left\{ \left(\frac{|\tilde{p}_2| + |\tilde{p}_1|}{2} \right) \exp \left[\frac{j}{2} (\angle\tilde{p}_2 + \angle\tilde{p}_1) \right] \right\} \left\{ \left(\frac{|\tilde{p}_2| + |\tilde{p}_1|}{2} \right) \exp \left[\frac{j}{2} (\angle\tilde{p}_2 + \angle\tilde{p}_1) \right] \right\}^*}{4\rho_0 c^2} \\ &= \frac{(|\tilde{p}_2| + |\tilde{p}_1|)^2}{16\rho_0 c^2} = \frac{G_{22} + G_{11} + 2|G_{12}|}{8\rho_0 c^2}. \end{aligned} \quad \text{Eq. A.19}$$

The kinetic energy is

$$\begin{aligned} E_k(\omega) &= \frac{\rho_0}{4} \left| \left(\frac{\exp \left[\frac{j}{2} (\angle\tilde{p}_2 + \angle\tilde{p}_1) \right] \left[j(|\tilde{p}_2| - |\tilde{p}_1|) - \frac{(|\tilde{p}_2| + |\tilde{p}_1|)}{2} (\angle\tilde{p}_2 - \angle\tilde{p}_1) \right]}{2\omega\rho_0 d} \right) \right|^2 \\ &= \frac{1}{4\omega^2 \rho_0 a^2} \left\{ (|\tilde{p}_2| - |\tilde{p}_1|)^2 + \left[\frac{(|\tilde{p}_2| + |\tilde{p}_1|)}{2} (\angle\tilde{p}_2 - \angle\tilde{p}_1) \right]^2 \right\} \\ &= \frac{1}{8\omega^2 \rho_0 d^2} \left[G_{11} + G_{22} - 2|G_{12}| + \frac{G_{11} + G_{22} + 2|G_{12}|}{4} (\arg\{H_{12}\})^2 \right]. \end{aligned} \quad \text{Eq. A.20}$$

Specific acoustic impedance is

$$\begin{aligned} z(\omega) &= \frac{\left(\frac{|\tilde{p}_2| + |\tilde{p}_1|}{2} \right) \exp \left[\frac{j}{2} (\angle\tilde{p}_2 + \angle\tilde{p}_1) \right]}{\exp \left[\frac{j}{2} (\angle\tilde{p}_2 + \angle\tilde{p}_1) \right] \left[j(|\tilde{p}_2| - |\tilde{p}_1|) - \frac{(|\tilde{p}_2| + |\tilde{p}_1|)}{2} (\angle\tilde{p}_2 - \angle\tilde{p}_1) \right]} \\ &= \frac{2\omega\rho_0 d (|\tilde{p}_2| + |\tilde{p}_1|)}{[2j(|\tilde{p}_2| - |\tilde{p}_1|) - (|\tilde{p}_2| + |\tilde{p}_1|)(\angle\tilde{p}_2 - \angle\tilde{p}_1)]} \\ &= \frac{2\omega\rho_0 d (G_{11} + G_{22} + 2|G_{12}|)}{[2j(G_{22} - G_{11}) + (G_{11} + G_{22} + 2|G_{12}|) \arg\{G_{12}\}]} \end{aligned} \quad \text{Eq. A.21}$$

A.5 PAGE method three-microphone expression:

The pressure at the center of the probe is estimated to be

$$\tilde{p}_c(\omega) = \tilde{p}_2(\omega), \quad \text{Eq. A.22}$$

where $\tilde{p}_2(\omega)$ is the pressure at the center microphone.

The particle velocity will be

$$\tilde{u}(\omega) = \frac{\exp(j\angle\tilde{p}_2) [j(|\tilde{p}_3| - |\tilde{p}_1|) - |\tilde{p}_2|(\angle\tilde{p}_3 - \angle\tilde{p}_1)]}{2\omega\rho_0 d}, \quad \text{Eq. A.23}$$

where $\tilde{p}_3(\omega)$ is the pressure at location d from the center microphone and $\tilde{p}_1(\omega)$ is the complex pressure at location d from the center microphone in the opposite direction.

The active intensity is then

$$\begin{aligned} I_a(\omega) &= \frac{1}{2} \text{Re}\{\tilde{p}_c \tilde{u}^*\} \\ &= \frac{1}{2} \text{Re} \left\{ \tilde{p}_2 \left[\frac{\exp(j\angle\tilde{p}_2) (j[|\tilde{p}_3| - |\tilde{p}_1|] - |\tilde{p}_2|[\angle\tilde{p}_3 - \angle\tilde{p}_1])}{2\omega\rho_0 d} \right]^* \right\} \\ &= \frac{G_{22} \arg\{H_{13}\}}{2\omega\rho_0 d}, \end{aligned} \quad \text{Eq. A.24}$$

where $2d$ is the separation between the microphones.

The reactive intensity is

$$\begin{aligned} I_r(\omega) &= \frac{1}{2} \text{Im}\{\tilde{p}_c \tilde{u}^*\} \\ &= \frac{1}{2} \text{Im} \left\{ \tilde{p}_2 \left[\frac{\exp(j\angle\tilde{p}_2) (j[|\tilde{p}_3| - |\tilde{p}_1|] - |\tilde{p}_2|[\angle\tilde{p}_3 - \angle\tilde{p}_1])}{2\omega\rho_0 d} \right]^* \right\} \\ &= \frac{|G_{23}| - |G_{21}|}{2\omega\rho_0 d}. \end{aligned} \quad \text{Eq. A.25}$$

The potential energy is

$$E_p(\omega) = \frac{|\tilde{p}_2|^2}{4\rho_0 c^2} = \frac{G_{22}}{2\rho_0 c^2}. \quad \text{Eq. A.26}$$

The kinetic energy is

$$\begin{aligned}
E_k(\omega) &= \frac{\rho_0}{4} \left| \frac{\exp(j\angle\tilde{p}_2) (j(|\tilde{p}_3| - |\tilde{p}_1|) - |\tilde{p}_2|(\angle\tilde{p}_3 - \angle\tilde{p}_1))}{2\omega\rho_0d} \right|^2 \\
&= \frac{1}{16\omega^2\rho_0d^2} \left((|\tilde{p}_3| - |\tilde{p}_1|)^2 \right. \\
&\quad \left. + (|\tilde{p}_2|(\angle\tilde{p}_3 - \angle\tilde{p}_1))^2 \right) \\
&= \frac{1}{8\omega^2\rho_0d^2} [G_{11} + G_{33} - 2|G_{13}| \\
&\quad + G_{22}(\arg\{H_{13}\})^2].
\end{aligned}$$

Eq. A.27

Specific acoustic impedance is

$$\begin{aligned}
z(\omega) &= \frac{\tilde{p}_2}{\frac{\exp(j\angle\tilde{p}_2) [j(|\tilde{p}_3| - |\tilde{p}_1|) - |\tilde{p}_2|(\angle\tilde{p}_3 - \angle\tilde{p}_1)]}{2\omega\rho_0d}} \\
&= \frac{2\omega\rho_0d|\tilde{p}_2|}{j(|\tilde{p}_3| - |\tilde{p}_1|) - |\tilde{p}_2|(\angle\tilde{p}_3 - \angle\tilde{p}_1)} \\
&= \frac{2\omega\rho_0dG_{22}}{j(|G_{23}| - |G_{21}|) + G_{22} \arg\{H_{13}\}}.
\end{aligned}$$

Eq. A.28

Bibliography

1. Hickling, R., Lee, P., and Wei, W. "Investigation of integration accuracy of sound-power measurement using an automated sound-intensity system," *Appl. Acoust.* **50**, 125-140 (1997).
2. Fahy, F. J. *Sound Intensity* (Thomson Press, Bury St Edmunds, Suffolk, Great Britain, 1995).
3. Jacobsen, F. "An overview of the sources of error in sound power determination using the intensity technique," *Appl. Acoust.* **50**, 155-166 (1997).
4. Gade, S., Ginn, K., Roth, O., and Brock, M. "Sound power determination in highly reactive environments using sound intensity measurements," *Proceedings of Inter-Noise* **83** (1983).
5. Jacobsen, F. "Spatial sampling errors in sound power estimation based upon intensity," *J. Sound Vibr.* **145**, 129-149 (1991).
6. Marquez, D. R. "Estimating the Acoustic Power of Sources in Nonideal Enclosures Using Generalized Acoustic Energy Density," in *Physics and Astronomy* (Brigham Young University, Provo, Utah) (2014).
7. Astrup, T. "Measurement of sound power using the acoustic intensity method--a consultant's viewpoint," *Appl. Acoust.* **50**, 111-123 (1997).
8. ISO 11205:2003. Acoustics - Noise Emitted by Machinery and Equipment - Engineering Method for the Determination of Emission Sound Pressure Levels in situ at the Work Station and at Other Specified Positions Using Sound Intensity," (International Organization for Standardization, Geneva, Switzerland, 2003).
9. ISO 9614-2:1996. Acoustics - Determination of sound power levels of noise sources using sound intensity - Part 2: Measurement by Scanning (International Organization for Standardization, Geneva, Switzerland, 1996).
10. ISO 15186-1:2003. Acoustics - Measurement of Sound Insulation in Buildings and of Building Elements Using Sound Intensity - Part 1: Field Measurements (International Organization for Standardization, Geneva, Switzerland, 2003).
11. ISO 9614-1:1993. Acoustics - Determination of sound power levels of noise sources using sound intensity - Part 1: Measurement at Discrete Points (International Organization for Standardization, Geneva, Switzerland, 1993).

12. ISO 9614-3:2002. Acoustics - Determination of sound power levels of noise sources using sound intensity -Part 3: Precision Method for Measurement by Scanning (International Organization for Standardization, Geneva, Switzerland, 2002).
13. ANSI/ASA S1.9:1996. Instruments for the Measurement of Sound Intensity (America, A. S. o., Melville, NY, 1996).
14. Stout, T. A., Gee, K. L., Neilsen, T. B., Wall, A. T., and James, M. M. "Source characterization of full-scale jet noise using acoustic intensity," *Noise Control Engr. J.* **63**, 522-536 (2015).
15. Gee, K. L., Whiting, E. B., Neilsen, T. B., James, M. M., and Salton, A. R. "Development of a near-field intensity measurement capability for static rocket firings," in *30th International Space Technology Symposium* (Kobe, Japan) (2015).
16. Jacobsen, F., and Jaud, V. "Statistically optimized near field acoustic holography using an array of pressure-velocity probes," *J. Acoust. Soc. Am.* **121**, 1550-1558 (2007).
17. Jacobsen, F., and Liu, Y. "Near field acoustic holography with particle velocity transducers," *J. Acoust. Soc. Am.* **118**, 3139-3144 (2005).
18. Maynard, J. D., Williams, E. G., and Lee, Y. "Nearfield acoustic holography: I. Theory of generalized holography and the development of NAH," *J. Acoust. Soc. Am.* **78**, 1395-1413 (1985).
19. Williams, E. G. *Fourier acoustics: sound radiation and nearfield acoustical holography* (Academic press, 1999).
20. Williams, E. G., and Takashima, K. "Vector intensity reconstructions in a volume surrounding a rigid spherical microphone array," *J. Acoust. Soc. Am.* **127**, 773-783 (2010).
21. Loyau, T., Pascal, J. C., and Gaillard, P. "Broadband acoustic holography reconstruction from acoustic intensity measurements. I: Principle of the method," *J. Acoust. Soc. Am.* **84**, 1744-1750 (1988).
22. Mann, J. A., and Tichy, J. "Near-field Identification of Vibration Sources, Resonant Cavities, and Diffraction Using Acoustic Intensity Measurements," *J. Acoust. Soc. Am.* **90**, 720-729 (1991).
23. Parkins, J. W., Sommerfeldt, S. D., and Tichy, J. "Narrowband and broadband active control in an enclosure using the acoustic energy density," *J. Acoust. Soc. Am.* **108**, 192-203 (2000).
24. Xu, B., Sommerfeldt, S. D., and Leishman, T. W. "Generalized acoustic energy density," *J. Acoust. Soc. Am.* **130**, 1370-1380 (2011).

25. Parkins, J. W. "Error analysis of a practical energy density sensor," *J. Acoust. Soc. Am.* **108**, 211-222 (2000).
26. Qiu, X., Hansen, C., and Li, X. "A comparison of near-field acoustic error sensing strategies for the active control of harmonic free field sound radiation," *J. Sound Vibr.* **215**, 81-103 (1998).
27. Bendat, J. S., and Piersol, A. G. *Random data: analysis and measurement procedures* (John Wiley & Sons, 2011).
28. Wolff, I., and Massa, F. "Use of pressure gradient microphones for acoustical measurements," *J. Acoust. Soc. Am.* **4**, 217-234 (1933).
29. Rose, M. T., Torrie, D. K., Rasband, R. D., Gee, K. L., and Sommerfeldt, S. D. "Comparison of pressure-based intensity measurements for different probe designs and estimation methods," *J. Acoust. Soc. Am.* **139**, 2065-2065 (2016).
30. Nutter, D. B. "Sound absorption and sound power measurements in reverberation chambers using energy density methods," in *Physics and Astronomy* (Brigham Young University, Provo, UT) (2006).
31. Ghan, J., Cazzolato, B. S., and Snyder, S. D. "Expression for the estimation of time-averaged acoustic energy density using the two-microphone method," *J. Acoust. Soc. Am.* **113**, 2404-2407 (2003).
32. De Bree, H.-E. "An overview of microflow technologies," *Acta acustica united with Acustica* **89**, 163-172 (2003).
33. De Bree, H.-E. "The Microflow: An acoustic particle velocity sensor," *Acoustics Australia* **31**, 91-94 (2003).
34. Fahy, F. J. "Measurement of acoustic intensity using the cross-spectral density of two microphone signals," *J. Acoust. Soc. Am.* **62**, 1057-1059 (1977).
35. Pavić, G. "Measurement of sound intensity," *J. Sound Vibr.* **51**, 533-545 (1977).
36. Chung, J. "Cross-spectral method of measuring acoustic intensity without error caused by instrument phase mismatch," *J. Acoust. Soc. Am.* **64**, 1613-1616 (1978).
37. Chung, J., and Pope, J. "Practical measurement of acoustic intensity-The two-microphone cross-spectral method," *Inter-Noise 78: Designing for Noise Control* **1** (1978).
38. Jacobsen, F. "Intensity Techniques," in *Handbook of Signal Processing in Acoustics* (Springer, New York, NY), pp. 1109-1127 (2008).

39. Jacobsen, F. "Sound Intensity," in *Springer Handbook of Acoustics* (Springer, New York, NY), pp. 1053-1075 (2007).
40. Jacobsen, F. "Random errors in sound intensity estimation," *J. Sound Vibr.* **128**, 247-257 (1989).
41. Elko, G. W. "Frequency domain estimation of the complex acoustic intensity and acoustic energy density," in *Acoustics* (Pennsylvania State University, State College, PA), p. 376 (1984).
42. Wolff, I., and Massa, F. "Direct measurement of sound energy density and sound energy flux in a complex sound field," *J. Acoust. Soc. Am.* **3**, 317-318 (1932).
43. Loyau, T., and Pascal, J.-C. "Statistical errors in the estimation of the magnitude and direction of the complex acoustic intensity vector," *J. Acoust. Soc. Am.* **97**, 2942-2962 (1995).
44. Seybert, A. F. "Statistical Errors in acoustic intensity measurements," *J. Sound Vibr.* **75**, 519-526 (1981).
45. Wiederhold, C. P., Gee, K. L., Blotter, J. D., and Sommerfeldt, S. D. "Comparison of methods for processing acoustic intensity from orthogonal multimicrophone probes," 2841-2852 (2012).
46. Wiederhold, C. P., Gee, K. L., Blotter, J. D., Sommerfeldt, S. D., and Giraud, J. H. "Comparison of multimicrophone probe design and processing methods in measuring acoustic intensity," *J. Acoust. Soc. Am.* **135**, 2797-2807 (2014).
47. Cazzolato, B. S., and Hansen, C. H. "Errors arising from three-dimensional energy density sensing in one-dimensional sound fields," *J. Sound Vibr.* **236**, 375-400 (2000).
48. Cazzolato, B. S., and Hansen, C. H. "Errors in the measurement of acoustic energy density in one-dimensional sound fields," *J. Sound Vibr.* **236**, 801-831 (2000).
49. Iino, T., Tatekawa, H., Mizukawa, H., and Suzuki, H. "Numerical evaluation of three-dimensional sound intensity measurement accuracies and a proposal for an error correction method," *Acoustical Science and Technology* **34**, 34-41 (2013).
50. Pascal, J.-C., and Li, J.-F. "A systematic method to obtain 3D finite-difference formulations for acoustic intensity and other energy quantities," *J. Sound Vibr.* **310**, 1093-1111 (2008).
51. Yanagisawa, T., and Koike, N. "Cancellation of both phase mismatch and position errors with rotating microphones in sound intensity measurements," *Journal of sound and vibration* **113**, 117-126 (1987).

52. Thomas, D. C., Christensen, B. Y., and Gee, K. L. "Phase and amplitude gradient method for estimation of acoustic vector quantities," *J. Acoust. Soc. Am.* **137**, 3366-3376 (2015).
53. Christensen, B. Y. "Investigation of a New Method of Estimating Acoustic Intensity and its Application to Rocket Noise," in *Department of Physics and Astronomy* (Brigham Young University, Provo Utah), p. 64 (2014).
54. Mann, J. A., Tichy, J., and Romano, A. J. "Instantaneous and Time-averaged Energy Transfer in Acoustic Fields," *J. Acoust. Soc. Am.* **82**, 17-30 (1987).
55. Mann III, J. A., and Tichy, J. "Acoustic intensity analysis: Distinguishing energy propagation and wave-front propagation," *J. Acoust. Soc. Am.* **90**, 20-25 (1991).
56. Gee, K. L., Neilsen, T. B., Whiting, E. B., Torrie, D. K., Akamine, M., Okamoto, K., Teramoto, S., and Tsutsumi, S. "Application of a Phase and Amplitude Gradient Estimator to Intensity-Based Laboratory-Scale Jet Noise Source Characterization," Berlin Beamforming Conference 2016 (2016).
57. Gee, K. L., Whiting, E. B., Neilsen, T. B., James, M. M., and Salton, A. R. "Development of a Near-field Intensity Measurement Capability for Static Rocket Firings," *Transactions of the Japan Society for Aeronautical and Space Sciences, Aerospace Technology Japan* **14**, Po_2_9-Po_2_15 (2016).
58. Locey, L. L. "Analysis and comparison of three acoustic energy density probes," in *Physics and Astronomy* (Brigham Young University, Provo, UT) (2004).
59. Wiederhold, C. P. "Analytical Comparison of Multimicrophone Probes in Measuring Acoustic Intensity," in *Mechanical Engineering* (Brigham Young University, Provo Utah), p. 206 (2011).
60. Blackstock, D. T. "Fundamentals of Physical Acoustics," pp. 440-465 (2000).
61. Tam, C. K., Pastouchenko, N. N., and Schlinker, R. H. "On the two sources of supersonic jet noise," *AIAA Paper* **37**, 145-153 (1999).
62. Liu, J. "Developing large-scale wavelike eddies and the near jet noise field," *J. Fluid Mech.* **62**, 437-464 (1974).
63. Liu, J. "Contributions to the understanding of large-scale coherent structures in developing free turbulent shear flows," *Adv. Appl. Mech.* **26**, 183-309 (1988).
64. Liu, J., Kailasanath, K., Ramamurti, R., Munday, D., Gutmark, E., and Lohner, R. "Large-eddy simulations of a supersonic jet and its near-field acoustic properties," *AIAA Paper* **47**, 1849-1865 (2009).

65. Nichols, J., Ham, F., Lele, S., and Bridges, J. "Aeroacoustics of a supersonic rectangular jet: Experiments and LES predictions," AIAA Paper **678**, 2012 (2012).
66. Du, Y., and Morris, P. J. "Noise simulations of supersonic hot jets for chevron nozzles," AIAA Paper **2787**, 2011 (2011).
67. Morris, P. J., and Boluriaan, S. "The prediction of jet noise from CFD data," AIAA Paper **2977**, 2004 (2004).
68. Morris, P. J., Du, Y., and Kara, K. "Jet noise simulations for realistic jet nozzle geometries," *Procedia Engineering* **6**, 28-37 (2010).
69. Morgan, J., Neilsen, T. B., Gee, K. L., Wall, A. T., and James, M. M. "Simple-source model of high power scale military jet noise beamforming analyses," *Noise Control Engr. J.* **60**, 435-449 (2012).
70. Shah, P., Vold, H., and Yang, M. "Reconstruction of far-field noise using multireference acoustical holography measurements of high-speed jets," AIAA Paper **2772**, 5-8 (2011).
71. Papamoschou, D. "Wavepacket modeling of the jet noise source," AIAA Paper **2835**, 2011 (2011).
72. Wall, A. T., Gee, K. L., and Neilsen, T. B. "Multisource statistically optimized near-field acoustical holography," *J. Acoust. Soc. Am.* **137**, 963-975 (2015).
73. Lee, M., and Bolton, J. S. "Scan-based near-field acoustical holography and partial field decomposition in the presence of noise and source level variation," *J. Acoust. Soc. Am.* **119**, 382-393 (2006).
74. Vold, H., Shah, P., Davis, J., Bremner, P., McLaughlin, D., Morris, P., Veltin, J., and McKinley, R. "High-resolution continuous scan acoustical holography applied to high-speed jet noise," AIAA Paper **3754**, 2010 (2010).
75. Stout, T. A., Gee, K. L., Neilsen, T. B., Wall, A. T., and James, M. M. "Intensity analysis of the dominant frequencies of military jet aircraft noise," 166th Meeting of the Acoustical Society of America **20**, 040010 (2013).
76. Harker, B. M., Gee, K. L., Neilsen, T. B., Wall, A. T., and James, M. M. "Wavepacket modeling and full-scale military jet noise beamforming analyses," AIAA Paper (2016).
77. Wall, A. T., Gee, K. L., James, M. M., Bradley, K. A., McInerny, S. A., and Neilsen, T. B. "Near-field noise measurements of a high-performance military jet aircraft," *Noise Control Engineering Journal* **60**, 421-434 (2012).
78. Gee, K. L., Giraud, J. H., Blotter, J. D., and Sommerfeldt, S. D. *Energy-Based Acoustical Measurements of Rocket Noise*, in *15th AIAA/CEAS Aeroacoustics Conference (30th*

AIAA Aeroacoustics Conference) (American Institute of Aeronautics and Astronautics, 2009).

79. Gee, K. L., Giraud, J. H., Blotter, J. D., and Sommerfeldt, S. D. "Near-field vector intensity measurements of a small solid rocket motor," *J. Acoust. Soc. Am.* **128**, EL69-EL74 (2010).
80. Neilsen, T. B., Gee, K. L., Wall, A. T., and James, M. M. "Similarity spectra analysis of high-performance jet aircraft noise," *J. Acoust. Soc. Am.* **133**, 2116-2125 (2013).
81. Neilsen, T. B., Gee, K. L., Harker, B. M., and James, M. M. "Level-educed Wavepackets Representation of NOise Radiation form a High-performance MIlitary Aircraft," *AIAA Paper* (2016).
82. Jordan, P., and Colonius, T. "Wave Packets and Turbulent Jet Noise," *Annual Review of Fluid Mechanics* **45**, 173-195 (2013).
83. Suzuki, T. "Coherent noise sources of a subsonic round jet investiaged using hydrodynamic and acoustic phased-microphone arrays," *J. Fluid Mech.* **730** (2013).
84. Suzuki, T., and Colonius, T. "Instability waves in a subsonic round jet detected using a near-field phase microphones array," *J. Fluid Mech.* **565**, 197-226 (2006).
85. Kerherve, F., Guitton, A., Jordan, P., Delville, J., Fortune, V., Gervais, Y., and Tinney, C. "Identifying the dynamics undelying the large-scale and fine-scale jet noise similarity spectra," *AIAA Paper* (2008).
86. Koenig, M., Cavlieri, A. V. G., Jordan, P., Delville, J., Gervais, Y., and Papamoschou, D. "Farfield filtering and source imaging of subsonic jet noise," *J. Sound Vibr.* **332**, 4067-4088 (2013).
87. Reba, R., Simonich, J., and Schlinker, R. "Measurement of Source Wave-Packets in High-Speed Jets and Connection to Far-Field Sound," *AIAA Paper* (2008).
88. Reba, R., Narayanan, S., and Colonius, T. "Wave-packet models for large-scale mixing noise," *Int. J. Aeroacoust.* **9** (2010).
89. Morris, P. J. "A note on noise generation by large scale turbulent structures in subsonic and supersonic jets," *Int. J. Aeroacoust.* **8**, 301-315 (2009).
90. Tam, C. K. "Jet noise: since 1952," *Theoretical and Computational Fluid Dynamics* **10**, 393-405 (1998).
91. Roth, D. J. "Sound intensity techniques of ridentifying location so scale model jet noise sources," *J. Acoust. Soc. Am.* **75** (1984).

92. Jaeger, S. M., and Allen, C. S. "Two-dimensional sound intensity analysis of jet noise," AIAA Paper **93** (1993).
93. Reba, R., Simonich, J., and Schlinker, R. "Sound radiated by large-scale wave-packet in subsonic and supersonic jets," AIAA Paper (2009).
94. Breakey, D. E., Jordan, P., Cavalieri, A. V., Léon, O., Zhang, M., Lehnasch, G., Colonius, T., and RODRíguez, D. "Near-field wavepackets and the far-field sound of a subsonic jet," 19th AIAA/CEAS Aeroacoustics Conference, Berlin, Germany, AIAA Paper **2083** (2013).
95. Kirkpatrick, S., D., G. J. C., and Vecchi, M. P. "Optimization by Simulated Annealing," Science **220**, 671-680 (1983).
96. Corte, H. "Simulated Annealing Optimization," (MATLAB File Exchange) (2011).
97. Metropolis, N., Rosenbluth, A. W., Rosenbluth, M. N., Teller, A. H., and Teller, E. "Equation of State Calculations by Fast computing Machines," J. Chem. Phys. **21** (1953).
98. McLaughlin, D. K., Kuo, C.-W., and Papamoschou, D. "Experiments on the effect of ground reflections on supersonic jet noise," AIAA Paper **22**, 2008 (2008).
99. Tam, C. K., Pastouchenko, N. N., and Schlinker, R. H. "Noise source distribution in supersonic jets," J. Sound Vibr. **291**, 192-201 (2006).
100. Varnier, J. "Experimental study and simulation of rocket engine freejet noise," AIAA Paper **39**, 1851-1859 (2001).
101. Haynes, J., and Kenny, R. J. "Modifications to the NASA SP-8072 Distributed Source Method II for Ares I lift-off environment predictions," 15th AIAA/CEAS Aeroacoustics Conference (2009).
102. Schlinker, R., Liljenberg, S., Polak, D., Post, K., Chipman, C., and Stern, A. "Supersonic jet noise source characteristics & propagation: Engine and model scale," AIAA Paper **3623**, 2007 (2007).
103. Cavalieri, A. V., Rodríguez, D., Jordan, P., Colonius, T., and Gervais, Y. "Wavepackets in the velocity field of turbulent jets," J. Fluid Mech. **730**, 559-592 (2013).
104. W. Tam, C. K. "Mach wave radiation from high-speed jets," AIAA Paper **47**, 2440-2448 (2009).
105. Neilsen, T. B., Gee, K. L., and James, M. M. "Spectral characterization in the near and mid-field of military jet aircraft noise," AIAA Paper **2191** (2013).